Reduced-Order Models of Bladed Disks and Vane with Mistuning and Frictionally Constrained Ring Damper

by

Seunghun Baek

A dissertation submitted in partial fulfillment
of the requirements for the degree of
Doctor of Philosophy
(Mechanical Engineering)
in the University of Michigan
2016

Doctoral Committee:

Professor Bogdan Epureanu, Chair
Professor Gregory M. Hulbert
Professor Nickolas Vlahopoulos
Professor Kon-Well Wang

Acknowledgments

I would like to express my deepest gratitude to my advisor, Professor Bogdan I. Epureanu, for his support and guidance during the past year. Your guidance, teaching, concern and enthusiasm, have always kept me motivated throughout these years.

I would like to extend my appreciation to my committee members: Professor Gregory M. Hulbert, Professor Nickolas Vlahopoulos and Professor Kon-Well Wang for their advice during my research.

This work was supported by GE Aviation through the University Strategic Alliance (USA) program. In this paper there is no data representative of an actual GE blisk.

Contents

List of Figures

List of Tables

Abstract

High performance bladed disks used in turbomachines have to meet strict standards in terms of aeroelastic stability and high-cycle fatigue. One structural characteristic of bladed disks which can significantly impact compliance with these standards is mistuning, namely small structural variability from blade to blade. To predict the effects of mistuning, computationally efficient methods are needed to enable free and forced-response analyses of full-assembly finite element models for both research and realistic industrial-size studies. Due to the size and complexity of typical industrial bladed disk models, one must resort to robust and systematic reduction techniques to create computationally fast reduced-order models of sufficient accuracy.

The main goal of this research is to develop a framework for efficient yet accurate linear and nonlinear vibration analysis of bladed disk systems with friction interfaces and structural or geometrical variations. The main component of the solution technique for predicting the nonlinear vibration response is based on novel reduced-order models (ROMs).

CHAPTER 1

1. Introduction

1.1. Overview

Gas turbines are widely used in aircraft, marine and space propulsion engines. Due to the vast extent of their applications, many efforts have been devoted to improvement of durability, efficiency and production costs. In the turbine, the compressor comprises of two consecutive components, the bladed disks and the vane, which are known to be rich dynamical systems that suffer from severe vibration problems. One of the most common problems is mistuning. Such mistuning of turbomachinery rotors or vanes is defined as random blade-to-blade geometric and structural variations that may occur during the manufacturing process and as a consequence of wear. It has been shown that while mistuning can cause a beneficial effect on flutter, it confers mostly undesirable effects on the forced responses. The system with mistuned blades can have drastically larger forced-response levels than the tuned system.

Preventing abnormal forced response level in bladed disk systems can be achieved by increasing damping to the system, and friction is one of the common ways to add damping. The numerical studies of the effects of mistuning on the free vibrations and forced response or the modeling and analysis of the friction forces at the contact interfaces have often been performed with finite element (FE) models. However, modern industrial FE models can be in the order of millions of degrees of freedom. This situation has led researchers to propose reduction techniques that retain the essential physics and dynamics captured by a high-fidelity model, but at a much lower computational cost. These efforts have created a large and growing area of research termed reduced order models (ROMs).

The effects of mistuning have been studied by experimental, analytical and numerical approaches over the past few decades. Several studies explored the dynamic behavior of mistuned bladed disks by using ROMs. In previous work, the entire bladed disk was substructured into a disk and several blade components to implement the mistuning projection by using a few modes of a single tuned cantilevered blade. Also, the tuned system modes were modeled in component mode mistuning methods by using modal participation factors of cantilevered blade modes. Thus, mistuning was projected onto cantilevered blade modes without requiring a component-based representation of the full system. In addition, by using modal participation factors, it was possible to project the mistuning by using just a few dominant cantilevered blade modes. However, such techniques assume that mistuning can be well modeled as variations in blade alone frequencies,

while blade-alone mode shapes are assumed invariant. That assumption does not hold for higher order modes of geometrically mistuned bladed disks. Geometric deformations contain stiffness and mass variations, and mistuning can no longer be captured by tuned cantilevered blade modes because the shapes of these modes are affected by mistuning. Previous studies compromised computational speed in favor of the ability to capture geometric mistuning. In this study, a new technique for generating ROMs of bladed disks with small geometric mistuning is discussed.

At the first chapter, a technique for generating ROMs of bladed disks with small geometric mistuning is proposed. Discrepancies in structural properties (mistuning) from blade to blade can cause a significant increase in the maximum vibratory stresses. The effects of mistuning have been studied over the past few decades. Many researchers have studied the dynamic behavior of mistuned bladed disks by using ROMs. Many of these techniques rely on the fact that the modes of a mistuned system can be approximated by a linear combination of modes of the corresponding tuned system. Also, the tuned system modes have been modeled in component mode mistuning by using modal participation factors of cantilevered blade modes. Such techniques assume that mistuning can be well modeled as variations in blade alone frequencies. However, since geometric deformations contain stiffness and mass variations, mistuning can no longer be captured by cantilevered blade modes alone. To address this, a new technique is presented for generating ROMs of bladed disks with small geometric mistuning which may be a more general case of mistuning in practice.

Preventing high cycle fatigue can be realized not only by judicious modeling and prediction of mistuning effects, but also by increasing damping to reduce vibration amplitudes. Friction is one of the common ways to add damping. Designing frictional interfaces for bladed disks systems is an important means adopted to dissipate vibration energy. Placement of dry friction dampers between blades or under the blades is a widely used technique. One of the recently emerging technologies uses ring dampers. These are ring-like substructures constrained to move inside a groove at the root of the blades. Such rings are in contact with the bladed disk due to centrifugal forces, and they create nonlinear dissipation by relative motion between the ring and the disk. The analysis of the resulting system involves computing the forced response of very large dimensional nonlinear structures. This is commonly done by numerical integration of the equations of motion. This is computationally inefficient especially for steady-state responses. To address this issue, new ROMs are developed in this work to capture the nonlinear behavior due to contact friction. The proposed approach is based on expressing the nonlinear force as response-dependent and iteratively solving linear systems with response-dependent characteristics. A key advantage of the proposed approach is that it requires only sector-level calculations to compute the response of the full-wheel system. A model of a bladed disk and the damper system is used to demonstrate the method. Macro- and micro-slip models are used to account for realistic behavior of dry friction damping.

At the second chapter, an efficient methodology to predict the nonlinear response of bladed disks with a dry friction ring damper is proposed. Designing frictional interfaces for bladed disk systems is an important

approach to dissipate vibration energy. One emerging technology uses ring dampers, which are ring-like substructures constrained to move inside a groove at the root of the blades. Such rings are in contact with the bladed disk due to centrifugal forces, and they create nonlinear dissipation by relative motion between the ring and the disk. The analysis of the dynamic response of nonlinear structures is commonly done by numerical integration of the equations of motion, which is computationally inefficient, especially for steady-state responses. To address this issue, ROMs are developed to capture the nonlinear behavior due to contact friction. The approach is based on expressing the nonlinear forces as equivalent nonlinear damping and stiffness parameters. The method requires only sector level calculations, and allows pre-calculation of the response-dependent equivalent terms. These factors contribute to the increase of the computational speed of the iterative solution methods. A model of a bladed disk and damper is used to demonstrate the method. Macro- and micro-slip are used in the friction model to account for realistic behavior of dry friction damping. For validation, responses due to steady-state traveling wave excitations are examined. Results computed by ROMs are compared with results from transient dynamic analysis in ANSYS with the full order model.

Modeling of contact interfaces is very important in many engineering applications. In turbomachinery, the friction force between the contact interfaces is one of the most common strategies applied to dampen the system. The friction force dissipates vibratory energy in the form of heat and reduces the resonance amplitude. To establish reliable models of bladed disks with friction dampers, it is necessary to obtain the accurate values of contact parameters. Accurate modeling require knowledge of contact parameters such as contact stiffness and contact damping, which are not readily available. Thus, there have been many attempts to extract the contact parameters correctly through both analytical and experimental methods. Most of these methods, however, assumed lightly loaded conditions or fixture tests, which are limited to specific geometries. Although the contact parameters are identified through the static and dynamic tests as a fixture, the contact stiffness may vary depending on its geometry and loading conditions.

At the third chapter, a methodology to identify the contact stiffness by measuring the forced responses of the system is suggested. A ROM is developed to predict the forced response of a bladed disk with a ring damper. Based on the ROM, an iterative solution to find the optimal contact parameters which can match the predicted response with the measured response is introduced. Nonlinear force associated with friction between the mechanical contact interfaces often affects structural response, causing localized nonlinear stiffness and damping changes. As many bladed disks assemblies use the friction forces as a source of damping, incorporating the effects of friction is necessary to produce predictive finite element models. The contact modeling by using the finite element method serves as a powerful and versatile tool. However, the reliable modeling of bladed disks with a friction damper is extremely complicated due to its nonlinear behaviors. Contact surfaces can experience slipping and, tension release depending on the magnitude of the normal and tangential forces at the contact interface. Often, contact parameters including stiffness and damping are unknown or inaccurate when applied to analytic models. An efficient methodology to identify the contact stiffness is suggested. An optimization problem is stated and solved by finding the minimum

residual between the measurement data from the dynamic responses of bladed disks with a friction ring damper and the predictions from the developed ROM.

Turbine engine compressors consist of many stages. Each stage consists of rotating blades and stationary stators or vanes. Interactions between the rotating blades and stationary vanes create traveling but harmonic excitations. A structure is said to be periodic when its construction has the form of spatially repeated units. Bladed disks are spatially repetitive structures, and their geometry is fully described by that of a fundamental region, or sector. In addition, the dynamic characteristics of a sector determine the dynamics behavior of the entire structure. Modern structural analysis of bladed disks takes advantage of this fact and is greatly simplified by the assumption of cyclic symmetry. In general, however, vanes consist of a number of packets; each packet having multiple sector interconnected with a platform and a casting. The vane system is partially periodic but not cyclic symmetric since the packets are not connected with each other. Due to this fact, the methodologies to understand the dynamic responses of cyclically symmetric structures are not applicable to a vane system. Therefore, a new approach to investigate the responses under traveling wave excitation and the effect of mistuning between the blades is presented.

At the forth chapter, mode based methodology is used to identify the most responding mode under a traveling wave excitation. Also, a ROM for calculating the effect of a damping mistuning combined with a stiffness mistuning on a vane packet is presented. A novel methodology for statistical analyses to investigate the effect of damping mistuning in a vane is presented also. The developed ROMs are validated by comparing ROM-predicted steady state harmonic responses to full-order analyses in ANSYS. It is observed that the maximum error of the ROM-predicted amplitude is under 1%. Based on the developed ROMs, a simple algebraic equation is derived for predicting amplification factors by introducing the concept of unit damping mistuning. Amplification factors for all engine order excitations are examined to verify the performance of the proposed methodology. The effects of damping mistuning are studied statistically through Monte Carlo simulations.

1.2. State of the art

There is more than 40 years of history of researches for mistuning effects on turbomachinery. Mistuning in blades was first identified from a number of experimental investigations done in the early 70's [1, 2, 3]. Also, it is found that mistuning can cause a significant increase in the maximum vibratory stress [4, 5, 6]. This increase is caused by the high modal density of bladed disks. Since mistuned mode shapes consist of several nodal diameter components, those mistuned modes can be excited by several engine orders. This yields multiple peaks in the frequency response curves. In general, numerous response peaks can observed in the mistuned bladed disk system (blisks), in contrast to the tuned case, where only the modes with number of nodal diameters corresponding to the applied engine order respond. It is observed that the resulting vibration energy from the dynamic response of a mistuned blisks can be concentrated on a few blades. This may lead to stress levels considerably higher than those predictions of the associated tuned bladed disk

assemblies. It is common to observe that the amplitude magnification level of 2 with small blade to blade material property variations (1-2%) [7]. The effect of the mistuning on forced response have been shown to feature a local maximum at a moderately low coupling level [8]. This phenomena can be explained by an energy augmentation mechanism [9]. The blade which experiences the maximum amplitude can draw on the energy being fed to the other blades in the assembly.

The intentional mistuning, which is called detuning, has been introduced to bladed disk design to reduce the effects of random mistuning. Ewins [10] suggested the advantages of grouping the blades into packets of shrouded blades. Griffin and Hoosac [11] considered an alternate mistuning pattern, placing blades with high and low frequencies alternatingly around the disk. Most recent studies focus on harmonic mistuning. Certain blade properties follow a sinusoidal pattern around the bladed disk.

In order to reduce the large computational cost associated with large size of finite element (FE) model of mistuned bladed disks, techniques to reduce the size of the FE models is required. To address this, reduced-order models (ROMs) have been proposed. Two main classes of ROMs have developed, based on Component Mode Synthesis (CMS) and classical modal analyses. The principles of the two methods are similar, as both methods employ tuned modes to reduce the finite element matrices. CMS methods employ modes of the individual substructures, however, rather than modes of the entire structure. Of particular importance for ROMs is to capture the effects of mistuning. Castanier et al. used that observation and captured the effects of small mistuning by using component-based ROMs. These ROMs account for mistuning as variations in blade stiffness (in a system-level synthesized stiffness matrix). Bladh et al. [12] developed this idea further by projecting the small mistuning onto the tuned cantilevered blade normal modes (fixed at the blade and disk interface). Since the modal stiffness variations are small, their implementation of mistuning is quite accurate. Yang and Griffin [13] have shown that the modes of a mistuned system can be approximated by a linear combination of modes of the corresponding tuned system. The approximation holds because the modal density of bladed disks is very high. Moreover, different mistuning patterns in each blade can be modeled by using several cantilevered blade modes simultaneously. This mistuning projection method has shown great potential for constructing ROMs [14] and is referred to as the component mode mistuning (CMM) method. In previous work [12, 14, 15, 16], the entire bladed disk was substructured into a disk and several blade components to implement the mistuning projection by using a few modes of a single tuned cantilevered blade. Also, the tuned system modes in CMM are modeled by using modal participation factors of cantilevered blade modes. Thus, mistuning can be projected onto cantilevered blade modes without requiring a component-based representation of the full system. In addition, by using modal participation factors, it is possible to project the mistuning by using just a few dominant cantilevered blade modes.

Blade disks are assembled from a large population of blades and disks, which results in random mistuning, and introduces random variations in maximum amplitude. To account for the effect of random mistuning in the design of bladed disk systems, statistical analyses of the forced response must be performed by considering deviations of the structural properties of individual blades random variables. Many study have used statistical

approaches that consider rotor structural parameters to be the actual statistical variables [17, 18, 19, 20]. The most straightforward method to obtain such statistics is by means of Monte Carlo simulations. Monte Carlo simulations are widely applied for statistical investigation of the forced responses of the mistuned blisks due to the accuracy of its results and the simplicity of its algorithm [18, 21, 22]. However, this is a computationally expensive approach. In the case of numerical models of large numbers of degrees of freedoms (DOFs), only limited results can be generated owing to the high computational costs. Therefore, alternative approaches have been considered to obtain the statistical characteristics of the forced responses. Reduced-order models have been developed to predict the mistuned forced responses in a computationally efficient manner [13, 23, 14]. These ROMs are sufficiently compact so that Monte Carlo simulations can be performed to collect the statistics of the forced responses from a large number of mistuned rotors. In these studies [24, 25], however, mistuning patterns are assigned only to the stiffness or blade-alone natural frequency. Since it is difficult to model damping with all damping mechanisms involved, there have been many attempts to develop ROMs approaches accounting for the different damping mechanisms separately. Lumped parameter models were used for constructing ROMs with structural damping [26, 2, 27]. Also, the original size of a finite element (FE) model was reduced by characterizing the modal damping mistuning at a sector level or desired nodal locations [23, 28]. Recently, Joshi [29] introduced a novel ROM to capture blade-to-blade damping variations among the blades of integrally bladed rotors.

To prevent high cycle fatigue failures due to large response levels at resonance, introducing dry friction dampers to bladed disk system is common strategies [30]. Due to the nonlinear nature of the friction force, modeling the effect of friction contacts in the structure is essential. The friction damping is widely used in turbine bladed disks with different types of geometric configurations. The fundamental type of friction damper is to use the blade-disk interfaces [31, 32, 33], and the shrouds located at the blade tip to connect adjacent blades by interference. The most common type is underplatform damper [34, 35, 36, 37], which is loaded by centrifugal force against the underside of the platform of two adjacent blades [34, 38]. Unlike other types of rotors, integrally bladed disks are made as one single piece of structure. Therefore, there is no inherent contact surfaces for energy dissipation via friction. To solve this issue, ring-shaped substructures have been proposed as a damper solution for blisks [39, 40, 41, 42, 43].

Bladed disks with frictional contacts between components can be modeled using FE analysis. Due to the complexity of the nonlinear behavior of friction dampers, however, several computational methods have been suggested. The most commonly used method for obtaining the response of nonlinear structures is direct numerical integration of the equations of motion [44, 45, 46]. Numerical integration is widely used to determine time-varying displacements, strains, stresses, and forces in a structure. This method calculates the dynamic responses and loads for all degrees of freedom at all FE nodal points in the most accurate manner. However, very heavy computation and tremendous computational time is needed to obtain the steady-state responses. Thus, the harmonic balance method (HBM) is often applied to reduce the computational cost. Frequency-domain methods such as HBM allow for a significant reduction in computational costs compared

to time-domain analysis [39, 34, 47, 48, 49, 50, 51]. Although the HBM method is efficient for large FE models, the computational cost is still expensive due to the large number of governing equations caused by the many DOFs involved in the nonlinearity.

Parameters at contact interfaces are of great importance to contact dynamics and interface modeling. It is shown that contact stiffness has a great effect on the accuracy of the results when it is studied by finite element methods. It is known that up to 90% of the damping and 60% of the deformation in a fabricated structure can arise from various connections [52]. The contact stiffness for the mechanical structure must be identified along with their expected ranges of variation in order to use FE models confidently. Contact surfaces can experience slipping and tension release depending on the magnitude of the normal and tangential forces at the contact interface. Due to its nonlinear behavior, the analysis of identifications of contact stiffness is generally complicate. There have been many efforts to investigate the contact parameters at the mechanical joint analytically [53, 54] and experimentally [55, 56, 57, 58]. Wang and Sas [59] suggested a method for finding the optimal linear joint stiffness and damping parameters from measured modal parameters (resonant frequency and damping ratio), and Ren and Beards [60] represent a method to extract the optimal linear joint parameters by using experimental frequency response data. Although those techniques are available for the identification of nonlinear joints, they are only applicable to those joints with specific configurations, or when dynamic tests are performed on a fixture.

CHAPTER 2

2. Reduced Order Models of Bladed Disks with Small Geometric Mistuning

2.1. Introduction

Bladed disks have been used in various applications, such as fans, impeller pumps, propellers and turbine generators. In general, a bladed disk is a cyclic symmetric structure, where all its sectors are identical and arranged around a central axis. In practice, however, deviations from cyclic symmetry are common due to manufacturing tolerances, material deviations, and uneven operating wear. These small irregularities, which are called mistuning, destroy the cyclic symmetry of bladed disks. Mistuning can cause a significant increase in the maximum vibratory stress [4, 5, 6]. This increase is caused by the high modal density of bladed disks. The effects of mistuning have been studied using experimental, analytical and numerical approaches over the past few decades. Tobias and Arnold [61] reported that inevitable imperfections in rotating disks cause mode pairs with identical natural frequencies to separate into two distinct modes. Since their research, there have been various studies aimed at understanding and predicting the vibration of mistuned turbomachinery bladed disks. Many researchers have studied the dynamic behavior of mistuned bladed disks by using lumped parameter models [4, 5, 62]. Although such models are simple, they can provide only a basic, qualitative understanding of the effects of mistuning. They cannot be used to predict accurately, quantitatively the vibratory response of industrial bladed disks. Industrial calculations require high fidelity models. Unfortunately, such high fidelity models are excessively large (often reaching hundreds of millions of degrees of freedom) and computationally expensive.

In addition, since mistuning patterns are random, statistical characterizations are required. Such characterizations are typically done by sample-based methods (such as Monte Carlo simulations) because the vibratory response is nonlinearly dependent on mistuning. Hence, tens of thousands of simulations are typically necessary to predict the dynamic response of a single bladed disk statistically; the computational cost is tremendous. To address this, reduced-order models (ROMs) have been proposed. Of particular importance for these models is to capture the effects of mistuning. Yang and Griffin [13] have shown that the modes of a mistuned system can be approximated as a linear combination of modes of the corresponding tuned system. This approximation holds because the modal density of bladed disks is high. Castanier et al. used that

observation and captured the effects of small mistuning by using component-based ROMs. These ROMs account for mistuning as variations in blade stiffness (in a system-level synthesized stiffness matrix). Bladh et al. [12] developed this idea further by projecting the small mistuning onto the tuned cantilevered blade modes (fixed at the interface between the blade and the disk). Since the modal stiffness variations are small, their implementation of mistuning is quite accurate. Moreover, different mistuning patterns in each blade can be modeled by using several cantilevered blade modes simultaneously [63]. This mistuning projection method has shown great potential for constructing ROMs [14], and is referred to as the component mode mistuning (CMM) method. In previous work [12, 14, 15, 16], the entire bladed disk was substructured into a disk and several blade components to implement the mistuning projection by using a few modes of a single tuned cantilevered blade. Also, the tuned system modes in CMM are modeled by using modal participation factors of cantilevered blade modes. Thus, mistuning can be projected onto cantilevered blade modes without requiring a component-based representation of the full system. In addition, by using modal participation factors, it is possible to project the mistuning by using just a few dominant cantilevered blade modes. However, the techniques for constructing ROMs discussed above assume that mistuning is simply variations in the modal stiffness of the blades. That assumption does not hold for higher order modes of geometrically mistuned bladed disks. Geometric deformations contain stiffness and mass variations, and mistuning can no longer be captured by cantilevered blade modes because the shapes of these modes are affected by mistuning [63]. To address this, several studies have focused on large geometric mistuning [14, 64, 63, 65]. Those studies compromised computational speed in favor of the ability to capture large geometric mistuning. However, in practice, bladed disks often suffer only from small geometric variability. In this paper, a new technique is presented for generating ROMs of bladed disks with small geometric mistuning. A modeling framework is developed by partitioning the system into a (whole) tuned bladed disk and (several) mistuning components. The tuned system modes are introduced in the ROM transformation matrix together with several additional basis vectors which can compensate for modeshape discrepancies due to small geometric variability. The additional basis vectors are obtained by algebraically manipulating the difference between tuned and geometrically mistuned modes. A key advantage of the new approach is that it uses only single-sector calculations. This provides gains in computational speed while accurately predicting system-level frequencies and modes.

2.2. Modeling

In this section, a methodology to model the dynamics of bladed disks having small geometric mistuning is presented. First, a new reduced basis for projecting the equations of motion of systems with small geometric mistuning is presented. Next, a sector based reduced order modeling method is proposed.

2.2.1. Projection basis

Let us consider a bladed disk with NB blades, where g of them are geometrically mistuned. Geometric mistuning in blades changes their mass and the stiffness matrices. Thus, it is well known that the full

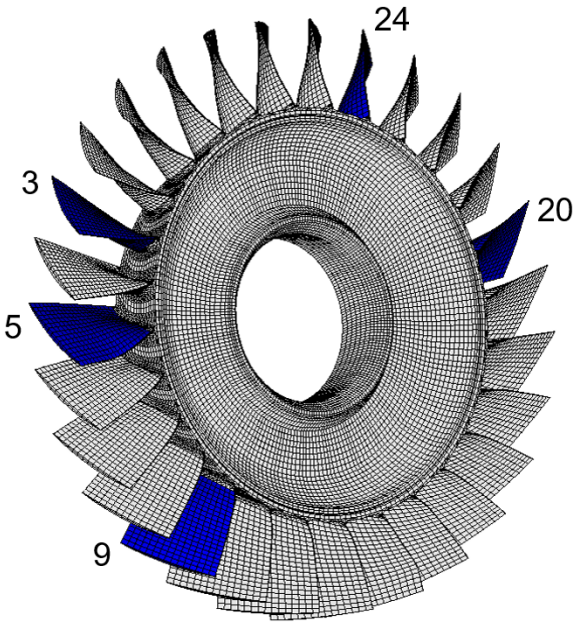

Figure 1: A finite element model of a blisks with geometric mistuning in blades number 3, 5, 9, 20 and 24 (mistuned blades are shown in blue)

geometrically mistuned modes cannot be represented by a basis of tuned system modes [14]. Therefore, additional basis vectors are required to capture the effects of geometric mistuning.

In the case of a tuned bladed disk, all blades are identical. Hence, tuned modes can be expressed in each sector j as a linear combination of two vectors $\mathbf{u}^t_{(n)}$ and $\bar{\mathbf{u}}^t_{(n)}$ as [66]

$$\begin{aligned}
\mathbf{\Phi}^t_{j(n)} &= \mathbf{u}^t_{(n)} cos\left(\frac{2\pi n}{NB}(j-1)\right) - \bar{\mathbf{u}}^t_{(n)} sin\left(\frac{2\pi n}{NB}(j-1)\right), \\
\bar{\mathbf{\Phi}}^t_{j(n)} &= \mathbf{u}^t_{(n)} sin\left(\frac{2\pi n}{NB}(j-1)\right) + \bar{\mathbf{u}}^t_{(n)} cos\left(\frac{2\pi n}{NB}(j-1)\right), \\
&\qquad\qquad (j = 1 \cdots NB)
\end{aligned} \tag{1}$$

where $\bar{\mathbf{\Phi}}^t_{j(n)}$ is the pair of $\mathbf{\Phi}^t_{j(n)}$, and n denotes the nodal diameter. Similarly, one can create a cyclic system in which all blades have the same (mistuned) geometric configuration as the j^{th} sector of the mistuned system. Herein, such systems are refered to as cyclic mistuned systems to differentiate it from the tuned system (which is also cyclic). Their modes are cyclic, and can be written as

$$\begin{aligned}
\mathbf{\Phi}^m_{j(n)} &= \mathbf{u}^m_{(n)} cos\left(\frac{2\pi n}{NB}(j-1)\right) - \bar{\mathbf{u}}^m_{(n)} sin\left(\frac{2\pi n}{NB}(j-1)\right), \\
\bar{\mathbf{\Phi}}^m_{j(n)} &= \mathbf{u}^m_{(n)} sin\left(\frac{2\pi n}{NB}(j-1)\right) + \bar{\mathbf{u}}^m_{(n)} cos\left(\frac{2\pi n}{NB}(j-1)\right), \\
&\qquad\qquad (j = 1 \cdots NB)
\end{aligned} \tag{2}$$

where vectors $\mathbf{u}^m_{(n)}$ and $\bar{\mathbf{u}}^m_{(n)}$ are vectors which characterize the cyclic mistuned system, and $\mathbf{\Phi}^m_{j(n)}$ and $\bar{\mathbf{\Phi}}^m_{j(n)}$ are a mode pair for that system. The cyclic modes obtained in Eq. (2) can be used as an addition to the

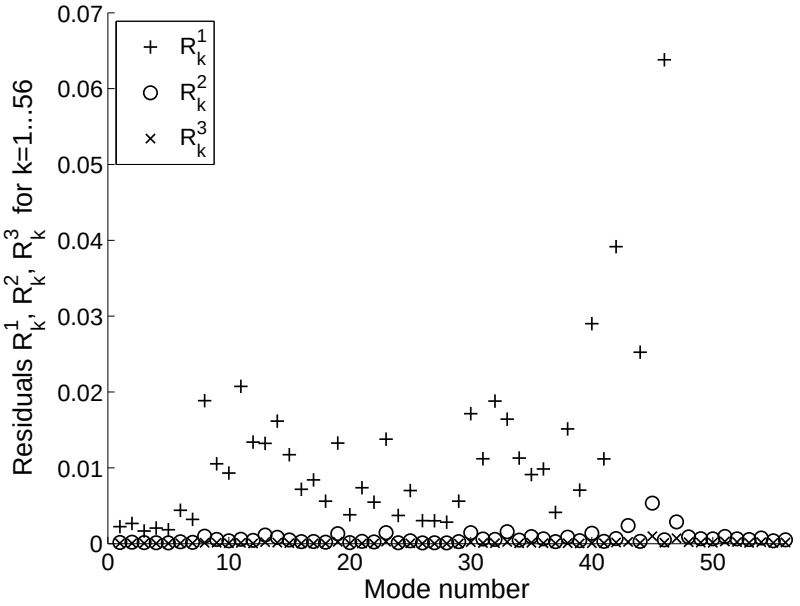

Figure 2: Residuals at each transformation matrix

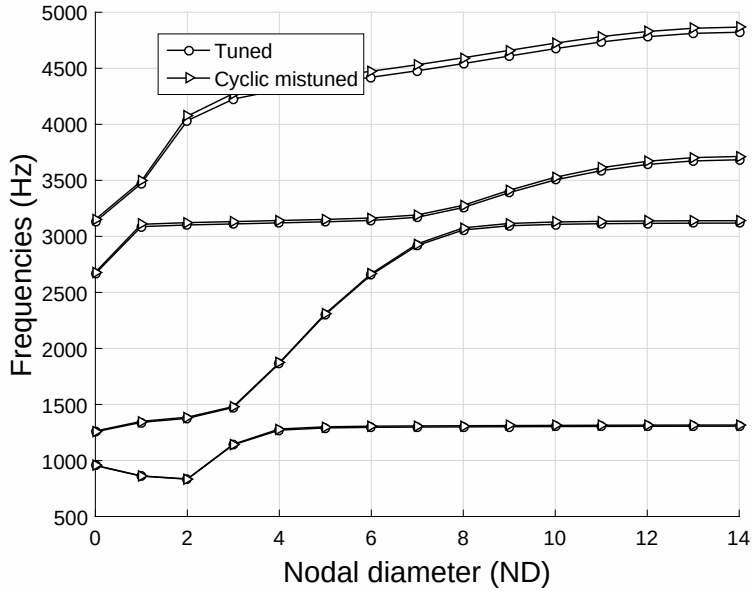

Figure 3: System frequencies of tuned and geometric modified blisks

basis together with the tuned modes in Eq. (1) in an attempt to capture the mistuned modes $\tilde{\mathbf{\Phi}}$ at sector j as,

$$\tilde{\mathbf{\Phi}}_j = \begin{bmatrix} \mathbf{\Phi}_j^t & \mathbf{\Phi}_j^m \end{bmatrix} \mathbf{q}_j, \tag{3}$$

where $\mathbf{q}_j$ are modal participations. Note that $\tilde{\mathbf{\Phi}}_j$, $\mathbf{\Phi}_j^t$ and $\mathbf{\Phi}_j^m$ are $r \times N$ matrices containing N modes for sector j, where r is the total number of DOFs in the finite element model of a sector.

The matrix $\begin{bmatrix} \mathbf{\Phi}_j^t & \mathbf{\Phi}_j^m \end{bmatrix}$ is in general full rank when the mistuning is large. However, for small mistuning,

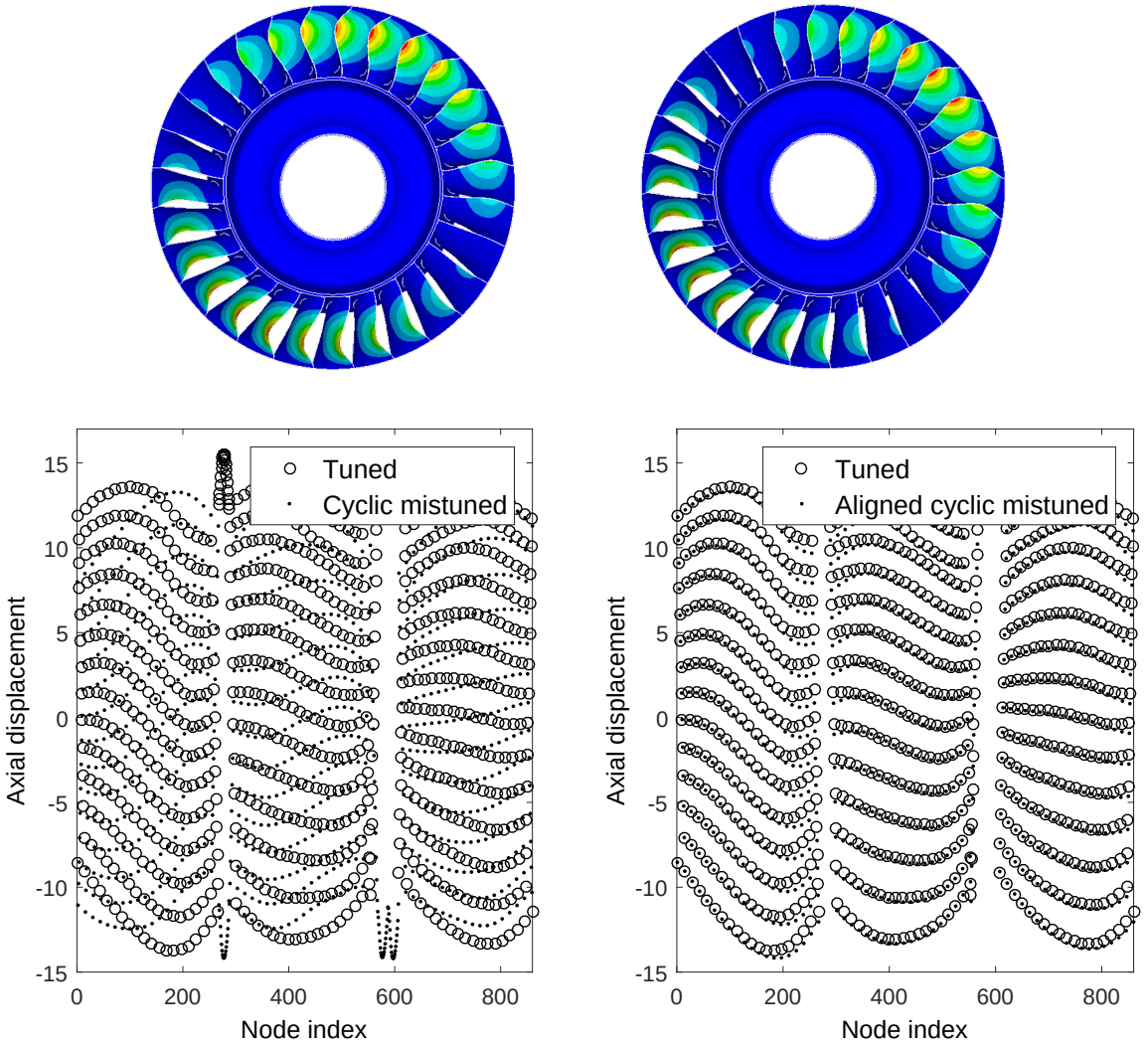

Figure 4: Top plots show full wheel models (tuned left and cyclic mistuned right); bottom plots show axial direction, blade portion modes from two different sector models without phase alignment (left) and with phase alignment (right)(n=1)

this matrix may not be full rank because the modes of the tuned and the cyclic mistuned systems can be nearly identical for many of the DOFs (such as the DOFs on the disk for example). To minimize the possible rank deficiency, matrix $\mathbf{\Phi}_j^m$ can be replaced with an equivalent representation, namely

$$\Delta\mathbf{\Phi}_j = \mathbf{\Phi}_j^m \mathbf{b}_j - \mathbf{\Phi}_j^t, \tag{4}$$

where $\mathbf{b}_j$ are scaling factors needed because modes are mass normalized. Consider that the disk and blade DOFs are ordered in such a manner as to give the following partitioning of the sector modes

$$\tilde{\mathbf{\Phi}}_j = \begin{bmatrix} \tilde{\mathbf{\Phi}}_{j,B} \\ \tilde{\mathbf{\Phi}}_{j,D} \end{bmatrix}, \quad \mathbf{\Phi}_j^t = \begin{bmatrix} \mathbf{\Phi}_{j,B}^t \\ \mathbf{\Phi}_{j,D}^t \end{bmatrix}, \quad \mathbf{\Phi}_j^m = \begin{bmatrix} \mathbf{\Phi}_{j,B}^m \\ \mathbf{\Phi}_{j,D}^m \end{bmatrix}, \tag{5}$$

where subscripts B and D refer to blade and disk DOFs in sector j. Since geometric mistuning is present only in the blades, the mode difference is dominant in the blade DOFs. Also, a scaling factor $\mathbf{b}_j$ can be defined

as $\mathbf{b}_j = diag\left(||\mathbf{\Phi}^t_{j,D,k}||/||\mathbf{\Phi}^m_{j,D,k}||\right)$, where $\mathbf{\Phi}^t_{j,D,k}$ and $\mathbf{\Phi}^m_{j,D,k}$ are the k^{th} mode of the tuned and cyclically mistuned systems, namely the k^{th} column of $\mathbf{\Phi}^t_{j,D}$ and $\mathbf{\Phi}^m_{j,D}$, respectively. Assuming that the effects of the geometric mistuning affect mostly the blade portion of the modes, one can approximate $\mathbf{\Phi}^m_{j,D}\mathbf{b}_j \approx \mathbf{\Phi}^t_{j,D}$. Therefore, Eq. (58) can be expressed as

$$\Delta\mathbf{\Phi}_j = \begin{bmatrix}\mathbf{\Phi}^m_{j,B}\\ \mathbf{\Phi}^m_{j,D}\end{bmatrix}\mathbf{b}_j - \begin{bmatrix}\mathbf{\Phi}^t_{j,B}\\ \mathbf{\Phi}^t_{j,D}\end{bmatrix} \approx \begin{bmatrix}\mathbf{\Phi}^m_{j,B}\mathbf{b}_j - \mathbf{\Phi}^t_{j,B}\\ \mathbf{0}\end{bmatrix} = \begin{bmatrix}\Delta\mathbf{\Phi}_{j,B}\\ \mathbf{0}\end{bmatrix}. \tag{6}$$

To explore which set of vectors $\mathbf{\Phi}^t_j$, $\mathbf{\Phi}^m_j$ and/or $\Delta\mathbf{\Phi}_j$ can be used to represent the mistuned modes of the blisk, we compute their corresponding residuals. These residuals are obtained when expressing mistuned modes as a linear combination of the columns of matrices $\mathbf{T}_1$, $\mathbf{T}_2$ and $\mathbf{T}_3$ given by

$$\mathbf{T}_1 = \mathbf{\Phi}^t,\ \ \mathbf{T}_2 = \left[\mathbf{\Phi}^t,\ \ \mathbf{\Phi}^m\right],\ \ \mathbf{T}_3 = \left[\mathbf{\Phi}^t,\ \ \Delta\mathbf{\Phi}\right], \tag{7}$$

where $\mathbf{\Phi}^t$ contains the full wheel tuned modes obtained using $\mathbf{\Phi}_j$, $\mathbf{\Phi}^m = \left[\mathbf{\Phi}^m_1\ \ \mathbf{\Phi}^m_2\ \cdots\ \mathbf{\Phi}^m_g\right]$, where $\mathbf{\Phi}^m_s$ contains the modes of a cyclic mistuned system which has all sectors having the same geometric mistuning, namely that of the s^{th} mistuned blade, and $\Delta\mathbf{\Phi} = \left[\Delta\mathbf{\Phi}^1\ \Delta\mathbf{\Phi}^2\ \cdots\ \Delta\mathbf{\Phi}^g\right]$, where g is the number of sectors with distinct geometric mistuning, and each $\Delta\mathbf{\Phi}^s$ is a set of full wheel vector obtained by cyclically expanding the sector-level vectors in matrices $\Delta\mathbf{\Phi}^s_j$ for each $s = 1, \cdots, g$ (recall that j is the reference sector). The residuals are defined as

$$\mathbf{R}^h_k = \frac{||\tilde{\mathbf{\Phi}}_k - \mathbf{T}_h\mathbf{q}_h||}{||\tilde{\mathbf{\Phi}}_k||}, \quad h = 1, 2, 3, \tag{8}$$

where $\tilde{\mathbf{\Phi}}_k$ is the k^{th} mistuned mode of the full wheel, and $\mathbf{q}_h = \mathbf{T}^\dagger_h\tilde{\mathbf{\Phi}}_k$, with $\dagger$ being the pseudoinverse.

A finite element model of a bladed disk with 28 blades is shown in Fig. 39. In this example, 5 blades are shown with geometric mistuning. The geometric mistuning was introduced as follows. All elements were selected at each blade tip. Their nodes were displaced in the radial direction so that the resulting blade length was up to 98% from its original length. To consider random mistuning, the deformations were different not only from blade to blade, but also different from node to node in the same blade. These geometric modifications lead to changes in system frequencies. The frequencies of the tuned system are shown in Fig. 3 together with the frequencies of a cyclic mistuned system where all blades have the same geometric mistuning (that of one of the mistuned blades shown in Fig. 39). The residuals obtained using Eq. (8) are plotted in Fig. 2. In this example, 56 of mistuned modes are examined, namely $k = 1, \cdots, 56$. The size of matrices $\mathbf{T}_1$, $\mathbf{T}_1$ and $\mathbf{T}_3$ are

$$\begin{aligned}
\mathbf{T}_1 &= \mathbf{\Phi}^t_{(r\cdot NB\times 56)},\\
\mathbf{T}_2 &= \left[\mathbf{\Phi}^t_{(r\cdot NB\times 56)}\ \mathbf{\Phi}^m_{1,(r\cdot NB\times 56)}\ \cdots\ \mathbf{\Phi}^m_{5,(r\cdot NB\times 56)}\right],\\
\mathbf{T}_3 &= \left[\mathbf{\Phi}^t_{(r\cdot NB\times 56)}\ \Delta\mathbf{\Phi}_{1,(r\cdot NB\times 56)}\ \cdots\ \Delta\mathbf{\Phi}_{5,(r\cdot NB\times 56)}\right],
\end{aligned} \tag{9}$$

As shown in Fig. 2, the mistuned modes are captured the best when $\mathbf{T}_3$ is adopted.

2.2.2. Phase alignment of cyclic modes

The differences between the modes in Eq. (58) cannot be used unless cyclic modes are aligned in phase (clocking). Each set of cyclic modes is computed independently. Thus, a phase shift between the cyclic modes may appear. This phase shift between two different tuned modes (also commonly referred to as clocking) is characterized by a rotation of the nodal diameters of the cyclic modes. A proper alignment of the modes is needed before Eq. (58) can be used. Let us consider the cyclic modes of a geometrically modified sector from Eq. (2). Substituting the inter blade phase angle $2\pi n(j-1)/NB$ with σ_j, and applying a rotation phase angle of φ^m, Eq. (2) can be rewritten as

$$\begin{aligned} \hat{\mathbf{\Phi}}^m_{j(n)} &= \hat{\mathbf{u}}^m_{(n)} cos\left(\sigma_j\right) - \hat{\bar{\mathbf{u}}}^m_{(n)} sin\left(\sigma_j\right), \\ \hat{\bar{\mathbf{\Phi}}}^m_{j(n)} &= \hat{\mathbf{u}}^m_{(n)} sin\left(\sigma_j\right) + \hat{\bar{\mathbf{u}}}^m_{(n)} cos\left(\sigma_j\right), \end{aligned} \tag{10}$$

where

$$\begin{aligned} \hat{\mathbf{u}}^m_{(n)} &= \mathbf{u}^m_{(n)} cos\varphi^m - \bar{\mathbf{u}}^m_{(n)} sin\varphi^m, \\ \hat{\bar{\mathbf{u}}}^m_{(n)} &= \mathbf{u}^m_{(n)} sin\varphi^m + \bar{\mathbf{u}}^m_{(n)} cos\varphi^m. \end{aligned} \tag{11}$$

In Fig. 4, cyclic modes each from one of two different sector models, are compared. The contour plots in Fig. 4 show the two full wheel cyclic modes. The bottom two graphs focus only on the reference sector. Circles represent values of the axial displacement in the blade portion of the tuned mode in the reference sector. Dots represent values of the axial displacement in the blade portion of the cyclic mistuned mode in the reference sector before and after alignment. The mistuned mode has blade length reduced to 98.5% of the tuned blade. The modes obtained from cyclic expansion have significant differences because of the phase difference (left). After alignment (right), the two modes have only small differences.

The phase angle φ^m which represents the phase difference between the different modes can be calculated by aligning $\mathbf{u}^m$ along $\mathbf{u}^t$ which can be done by finding the maxima of

$$\begin{aligned} f(\varphi^m) &= {\mathbf{u}^t}^T_{(n)} \hat{\mathbf{u}}^m \\ &= {\mathbf{u}^t}^T_{(n)} (\mathbf{u}^m_{(n)} cos\varphi^m - \bar{\mathbf{u}}^m_{(n)} sin\varphi^m). \end{aligned} \tag{12}$$

Note that aligning $\mathbf{u}^t$ and $\mathbf{u}^m$ automatically alignes also $\bar{\mathbf{u}}^t$ and $\bar{\mathbf{u}}^m$. The phase alignment is achieved when φ^m satisfies

$$df(\varphi^m)/d\varphi^m = -{\mathbf{u}^t}^T_{(n)} (\mathbf{u}^m_{(n)} sin\varphi^m + \bar{\mathbf{u}}^m_{(n)} cos\varphi^m) = 0. \tag{13}$$

Thus, the alignment phase angle is given by

$$tan\left(\varphi^m\right) = \frac{{\mathbf{u}^t_{(n)}}^T \bar{\mathbf{u}}^m_{(n)}}{{\mathbf{u}^t}^T_{(n)} \mathbf{u}^m_{(n)}}. \tag{14}$$

2.2.3. Reduced order modeling

The equation of motion of a bladed disk system with geometric mistuning can be written as

$$\mathbf{M}\ddot{\mathbf{X}}(t) + \frac{\gamma}{\omega}\mathbf{K}\dot{\mathbf{X}}(t) + \mathbf{K}\mathbf{X}(t) = \mathbf{F}(t), \tag{15}$$

where $\mathbf{M}$ is the mass matrix, $\mathbf{K}$ is the stiffness matrix, γ is the structural damping coefficient, and $\mathbf{F}$ is the external force. The mass matrix $\mathbf{M}$ is composed of block matrices $\mathbf{M}_1, \cdots, \mathbf{M}_{NB}$ for NB sectors. Each matrix $\mathbf{M}_k$ is the free-interface mass matrix for a sector k. Assembling matrices $\mathbf{M}_k$ into $\mathbf{M}$ requires overlap at the DOFs on the interface between sectors. Instead of working with full assembled matrices, we operate with sector-level matrices by using free-interface matrices and duplicating the DOFs at the interfaces between sectors. Note that typical sizes of bladed disk models used in industry often exceed 10 million DOFs. Thus, sector-level calculations can be very helpful by eliminating the need to form full wheel finite element matrices.

The transformation matrix used to obtain ROMs consists of tuned modes cyclically expended from a sector, and diagonally stacked additional block matrices $\Delta\mathbf{\Phi}_{s,B}$ with $s = 1, \cdots, g$. For all g different geometric mistuned blades, the transformation matrix $\mathbf{T}_3$ of the full wheel system can be written using Eq. (6) as

$$\mathbf{T}_3 = \begin{bmatrix} \mathbf{\Phi}^t & \Delta\mathbf{\Phi} \end{bmatrix} = \begin{bmatrix} \mathbf{\Phi}^t_{1,B} & \Delta\mathbf{\Phi}_{1,B} & \cdots & \mathbf{0} \\ \vdots & \vdots & \ddots & \vdots \\ \mathbf{\Phi}^t_{g,B} & \mathbf{0} & \cdots & \Delta\mathbf{\Phi}_{g,B} \\ \vdots & \vdots & \ddots & \vdots \\ \mathbf{\Phi}^t_{NB,B} & \mathbf{0} & \cdots & \mathbf{0} \\ \mathbf{\Phi}^t_{1,D} & \mathbf{0} & \cdots & \mathbf{0} \\ \vdots & \vdots & \ddots & \vdots \\ \mathbf{\Phi}^t_{NB,D} & \mathbf{0} & \cdots & \mathbf{0} \end{bmatrix}. \tag{16}$$

Note that each column $\mathbf{\Phi}^t$ has the system level modes expanded from all DOFs in a sector including interfaces. Hence, there is duplicated interface nodal information between adjacent sectors.

By introducing the transformation matrix from Eq. (16) into Eq. (15), the following ROM is obtained

$$\left[-\omega^2\mathbf{m} + i\gamma\mathbf{k} + \mathbf{k}\right]\mathbf{q} = \mathbf{f}, \tag{17}$$

$$\mathbf{m} = \begin{bmatrix} \mathbf{\Phi}^t & \Delta\mathbf{\Phi} \end{bmatrix}^T \begin{bmatrix} \mathbf{M}_1 & \mathbf{0} & \cdots & \mathbf{0} \\ \mathbf{0} & \mathbf{M}_2 & \cdots & \vdots \\ \vdots & \vdots & \ddots & \vdots \\ \mathbf{0} & \mathbf{0} & \cdots & \mathbf{M}_{NB} \end{bmatrix} \begin{bmatrix} \mathbf{\Phi}^t & \Delta\mathbf{\Phi} \end{bmatrix}, \tag{18}$$

$$\mathbf{k} = \begin{bmatrix} \mathbf{\Phi}^t & \Delta\mathbf{\Phi} \end{bmatrix}^T \begin{bmatrix} \mathbf{K}_1 & \mathbf{0} & \cdots & \mathbf{0} \\ \mathbf{0} & \mathbf{K}_2 & \cdots & \vdots \\ \vdots & \vdots & \ddots & \vdots \\ \mathbf{0} & \mathbf{0} & \cdots & \mathbf{K}_{NB} \end{bmatrix} \begin{bmatrix} \mathbf{\Phi}^t & \Delta\mathbf{\Phi} \end{bmatrix}, \tag{19}$$

$$\mathbf{f} = \begin{bmatrix} \mathbf{\Phi}^t & \Delta\mathbf{\Phi} \end{bmatrix}^T \mathbf{F}. \tag{20}$$

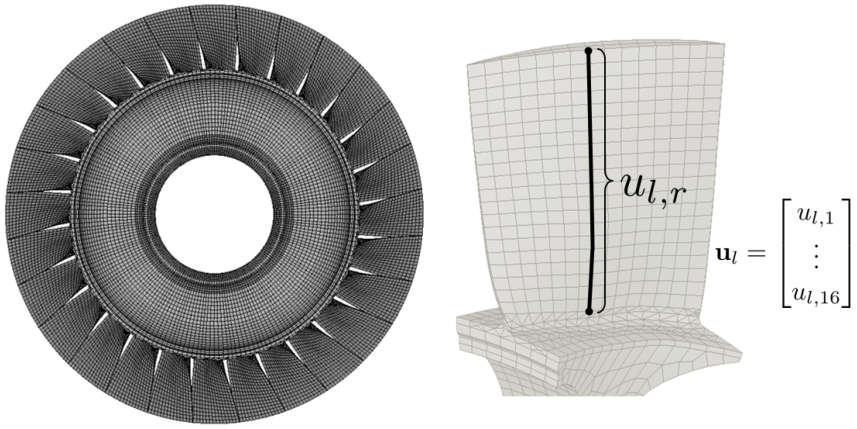

Figure 5: Finite element model of the academic blisks and the blade model at sector l

The block diagonal structure of the large matrices in Eqs. (18) and (19) allows one to obtain $\mathbf{m}$ and $\mathbf{k}$ with only single sector calculations. The natural frequencies and (residual order) modes $\mathbf{\Phi}^{m,ROM}$ of a mistuned system can be obtained by solving the eigenvalue problem

$$\mathbf{k}\mathbf{\Phi}^{m,ROM} = \omega_n^{m2}\mathbf{m}\mathbf{\Phi}^{m,ROM}, \tag{21}$$

where ω_n^m are the natural frequencies of the mistuned system. The ROM given in Eq. (15) can be validated by comparing its natural frequencies and forced response with the natural frequencies and forced response obtained from the full order system.

2.3. Results

An academic blisk finite element model with 28 blades is used to demonstrate the proposed ROMs. The full model consists of 95,648 linear solid elements with 235,788 DOFs, and its finite element mesh is shown in Fig. 5. In this finite element model, there are sixteen radial lines of nodes on each blade (Fig. 5 right). The length of each radial line of nodes is denoted by $u_{l,r}$, where l and r represent the sector number and

Table 1: Values of the random variable $\xi_{1,r}$

$\xi_{1,1}$	$\xi_{1,2}$	$\xi_{1,3}$	$\xi_{1,4}$	$\xi_{1,5}$	$\xi_{1,6}$
-0.403	-1.223	-0.855	-0.478	-0.013	-0.845
$\xi_{1,7}$	$\xi_{1,8}$	$\xi_{1,9}$	$\xi_{1,10}$	$\xi_{1,11}$	$\xi_{1,12}$
0.007	0.278	-0.759	-0.703	-0.440	-0.230
$\xi_{1,13}$	$\xi_{1,14}$	$\xi_{1,15}$	$\xi_{1,16}$		
-1.287	-0.844	0.503	-1.427		

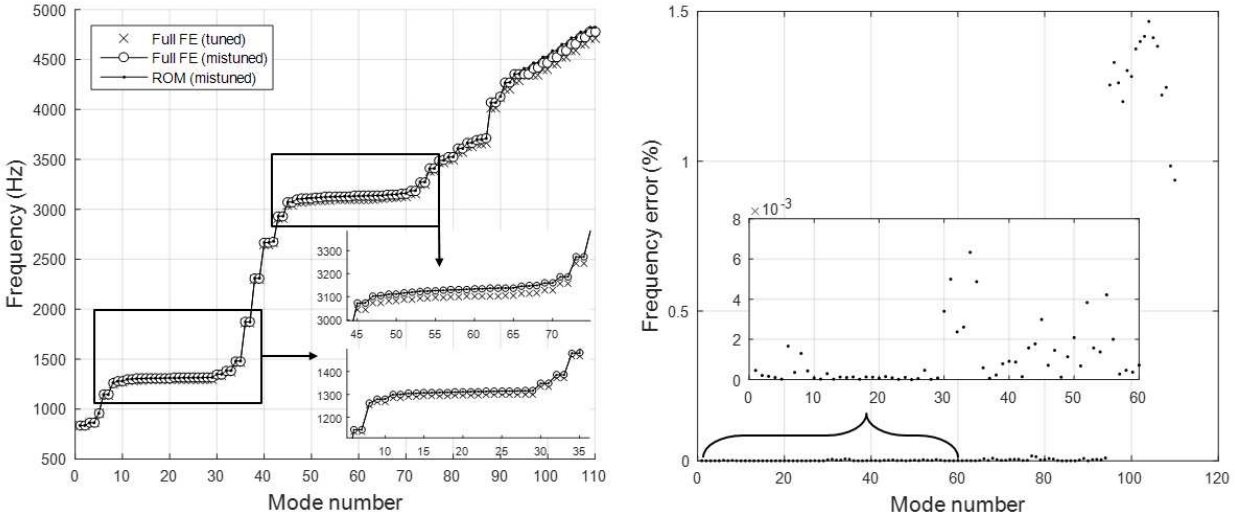

Figure 6: The system frequencies (left) and the system frequency errors (right)

the node column index, respectively. Thus, the nominal tuned sector has a vector $\mathbf{u}_l$ representing lengths of radial lines of nodes between the blade tip and the blade root.

By multiplying random values to the vector $\mathbf{u}_j$, we can introduce geometric mistuning patterns to model variability in the blade length as well as unevenness of the blade tip. The mistuning pattern at a sector l can be expressed as

$$\bar{\mathbf{u}}_l = diag\left[(1+\zeta_l)(1+\xi_{l,r})\right]\mathbf{u}_l, \qquad r = 1, 2, ..., 16, \tag{22}$$

where $diag[\cdot]$ refers to a diagonal matrix which consists of values $(1+\zeta_l)(1+\xi_{l,r})$. The random variable ζ_l defines a uniform blade length deformation at sector l. The second random variable, $\xi_{l,r}$ describes uneven blade tips by changing the length of each line of nodes. The random variables have values within a certain range to maintain the mesh quality. In this simulation, the range of ζ_l and $\xi_{l,r}$ are $\pm 1\%$ and $\pm 2\%$, respectively. For example, at sector 1, a values of -1% is used for ζ_1, and the values listed in the Table 1 are used for $\xi_{l,r}$.

The deformed geometry of blade 1 is shown in Fig. 7. The mistuned blade is shortened by -1% from its original length, with an uneven blade tip. Likewise, all 28 blades in the full finite element model are modified by different random mistuning values for ζ_l and $\xi_{l,r}$.

In Fig. 8, the first cantilevered blade frequency of each mistuned blade is plotted together with the frequency of the tuned cantilevered blade.

The system frequencies of the mistuned blisk obtained from the full finite element model and the ROM are compared in Fig. 6. The system frequencies obtained using the ROM match very well the full order model prediction. However, an error jump to the level of 1% is observed beyond the 95^{th} mode. The jump is because sets of only 110 modes were used in the projection matrix $\mathbf{T}_3$. Nevertheless, the first 60 modes have very small errors. Note the inset figure on the right side. Small errors are observed between the 10^{th} and the 30^{th} mode, which are the blade dominant modes. The frequency error between the 30^{th} and 40^{th} modes are

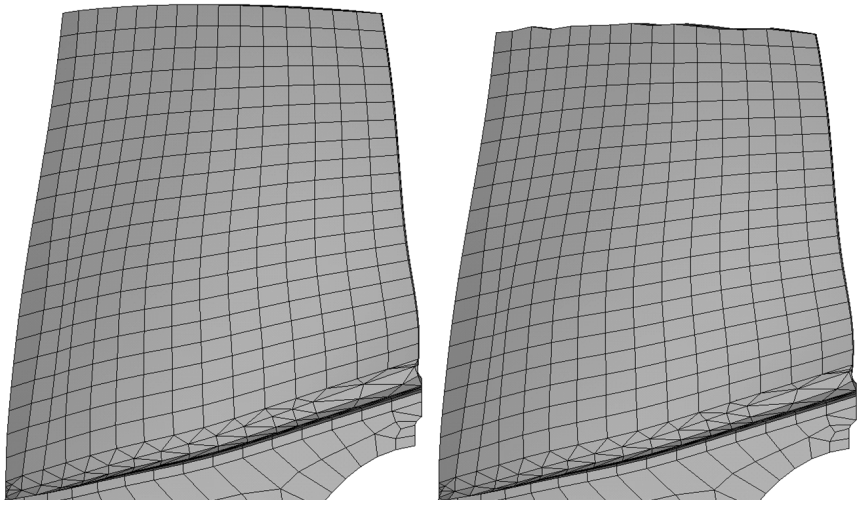

Figure 7: Tuned blade (left) and geometrically mistuned blade (right)

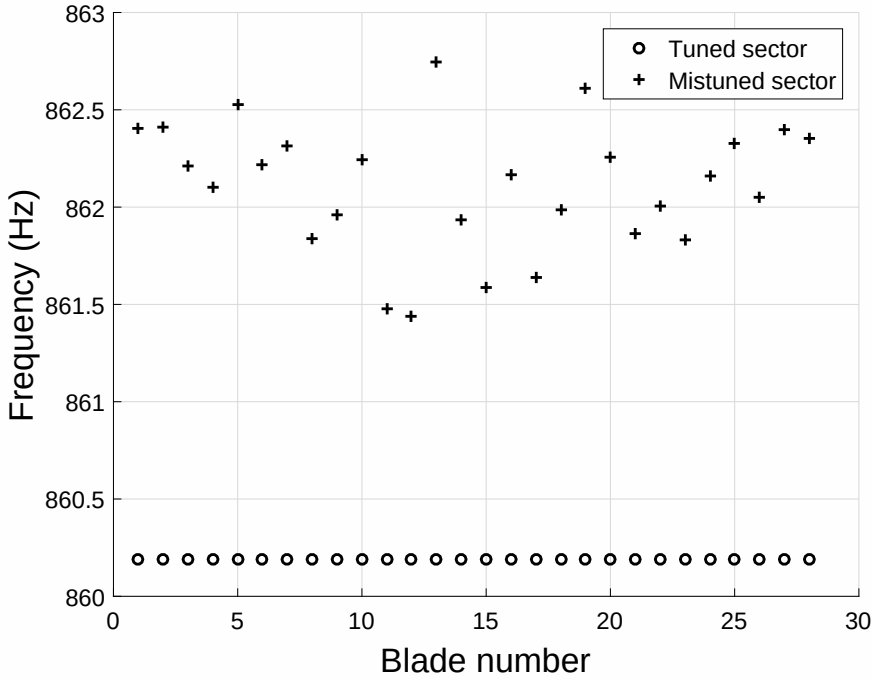

Figure 8: Blade alone frequences

higher. This region corresponds to the slanted line in the nodal diameter plot in Fig. 3, where there are disk dominant modes. In this region, the assumption that the modes differences in the disk portion are nearly 0 (namely $\mathbf{\Phi}^m_{j,D}\mathbf{b}_j \approx \mathbf{\Phi}^t_{j,D}$) is ineffective. Errors can be observed also in the second blade dominant region, from the 40^{th} to 60^{th} modes. Nonetheless, the errors are small enough for all the first 60 modes to conclude that the ROM can estimate natural frequencies of the mistuned system with good accuracy and less than 0.01% error.

Next, we consider the forced response of the blisk. Both tuned and mistuned systems are examined by

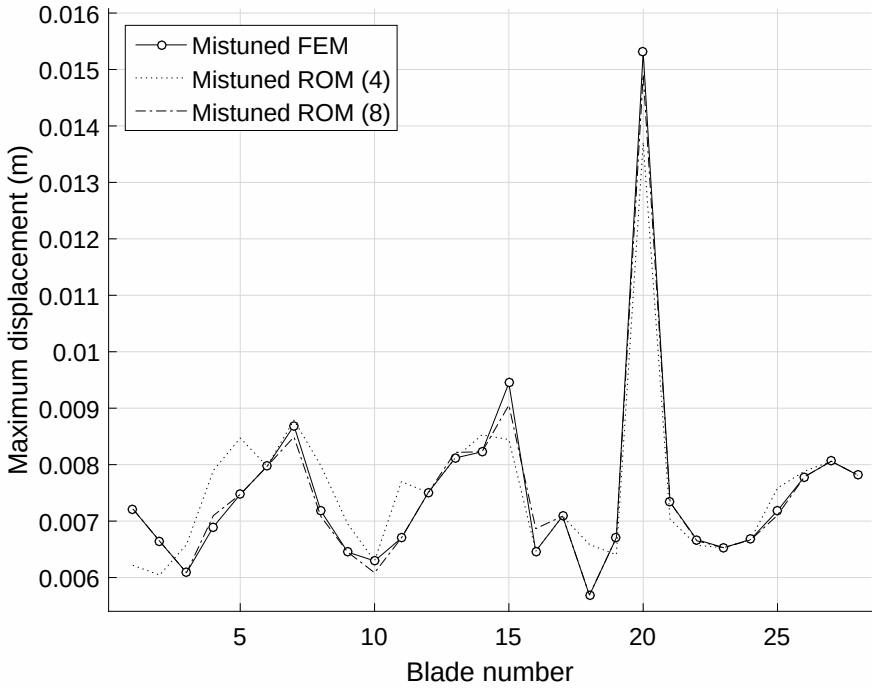

Figure 9: Mistuned response at the natural frequency of the 6^{th} mode (1,284.98 Hz), obtained by using full order model, a ROM with 4 additional $\mathbf{\Delta\Phi}$ modes at each mistuned sector, and a ROM with 8 additional $\mathbf{\Delta\Phi}$ modes at each mistuned sector

applying traveling wave excitation. The excitation consists of a unit nodal load applied on the tip of each blade leading edge into the axial direction. To compare the responses predicted by the ROM and the full order model, we compute the Euclidean norm of the displacement amplitudes by summing the norm of the physical displacement amplitudes for all DOFs and for each blade l. To illustrate the correlation between the full finite element model and the ROM, the maximum displacements in the blade nodes are determined as

$$d_l = \underset{l=1,\cdots,v/3}{max} \sqrt{\mathbf{X}_{l,k}^{R^2} + \mathbf{X}_{l,k}^{\theta^2} + \mathbf{X}_{l,k}^{Z^2}}. \tag{23}$$

where l is the blade number, k is the node number, which varies from 1 to $v/3$, with v being the numbers of DOFs in a blade. The displacement amplitudes in the radial ($\mathbf{X}_{l,k}^{R}$), tangential ($\mathbf{X}_{l,k}^{\theta}$) and axial ($\mathbf{X}_{l,k}^{Z}$) directions are indicated by superscripts R, θ and Z respectively.

The natural frequencies of the tuned system are plotted as a function of the nodal diameter in Fig. 3. Lines are drawn to help visualize mode families. The excitation frequencies are selected from the first mode family. In the first mode family, the blade dominant modes appear as a horizontal line between 1,250 Hz and 1,300 Hz. In this particular frequency range, the mistuned modes are not pure nodal diameter modes, and can be excited by all engine order excitations. For example, Fig. 9 shows the maximum forced response at each blade at 1,284.98 Hz (6^{th} mistuned natural frequency). The vibration energy is localized at blade 20.

Furthermore, frequency sweep excitations through resonance are performed. The frequency range selected

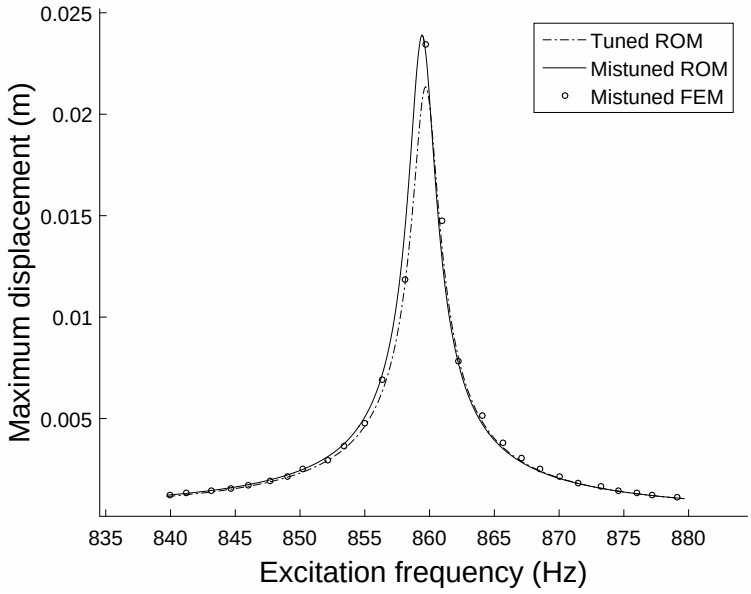

Figure 10: Engein order 1 excitation

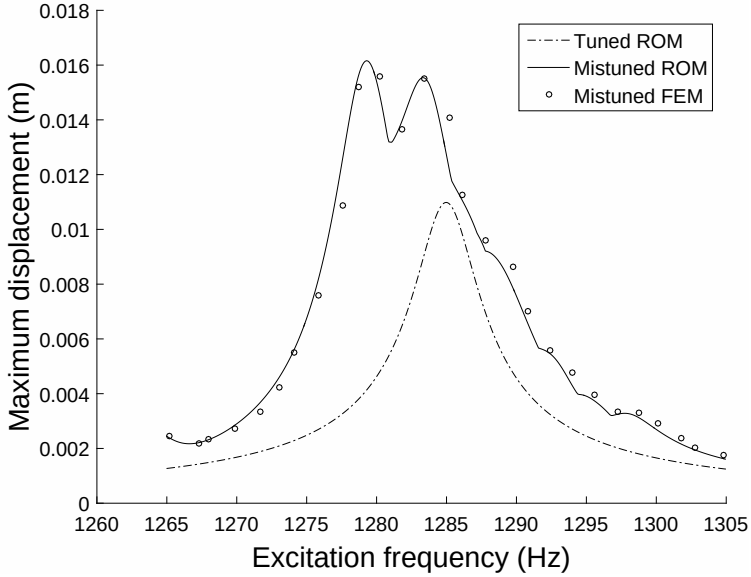

Figure 11: Engein order 6 excitation

is ± 20 Hz from the natural frequencies of the tuned system. Figs. 10 and 11 shows results obtained when the bladed disk is excited separately at engine order excitations 1 and 6. The vertical axes represent $\underset{l=1,\cdots,28}{max}(d_l)$ for the entire mistuned system, where d_l is given by Eq. (23). The response of the mistuned system at engine order excitation 1 only shows a single resonance frequency, shifted near 860 Hz. However, engine order excitations 6 and 8 lead to substantial increases in peak response amplitudes and a very significant widening of the frequency response curve compared to the response of the tuned bladed disk. The predicted responses from the ROM, and the responses calculated by the full finite element model show very good agreement.

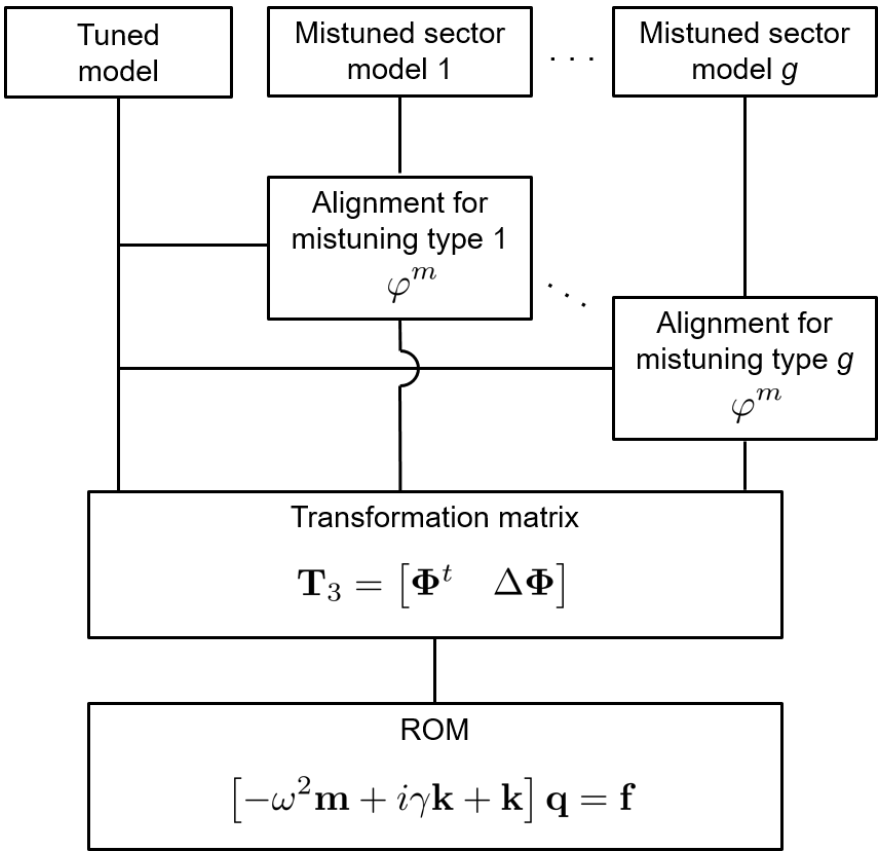

Figure 12: Schematic of ROM precedure

2.4. Discussion and conclusions

A novel reduced order modeling method was presented to model small geometric mistuning in bladed disk systems. The method is a modification and extension of several other methods [14, 63, 64, 65]. A novel modeling framework was developed by partitioning the system into a (whole) tuned bladed disk and (several) mistuning components. A flow chart of the reduction process is provided in Fig. 18. First, sector level modes, and mass and stiffness matrices are obtained for both the tuned and mistuned sectors. Second, modes are aligned using a proper phase shift given by Eq. (14). Lastly, the tuned system modes expanded from the sector modes are used to form the ROM transformation matrix $\mathbf{T}_3$ given by Eq. (7) together with several additional vectors in $\Delta\mathbf{\Phi}$ which compensate for mode discrepancies due to small geometric variability. The additional vectors in $\Delta\mathbf{\Phi}$ were obtained by algebraically manipulating the difference between tuned and (aligned) cyclic mistuned modes.

The new approach uses only sector-level calculations which provide significant savings in computational resources while accurately predicting system level frequencies and forced response. Moreover, only the blade portion of the modes are needed in $\Delta\mathbf{\Phi}$, and that further reduces the need for numerical computational resources. In the specific example, the total number of DOFs of the whole model was 235,788, compared to only 620 of the ROM.

Repeated computations of cyclic symmetry analysis are required according to the number of mistuned blades to obtain the transformation matrix $\mathbf{T}_3$. However, the transformation matrix is computed using only sector level calculations, eliminating the need for extracting full order matrices.

The vectors in $\Delta\mathbf{\Phi}$ are obtained by an algebraical subtraction between tuned and mistuned modes. Thus, those modes have to have the same number of DOFs. Missing parts of blades or large changes in the mesh might cause this approach to fail.

Numerical results for the academic blisk model were presented to demonstrate the effectiveness of the approach. The predicted natural frequencies and forced response results obtained for the ROM were in excellent agreement with the results from full order finite element analysis. The mistuning patterns used in this study include deformations in the length of the blades and in uneven blade tips which mimic some of the geometric mistuning observed in practice.

CHAPTER 3

3. Reduced Order Modeling of Tuned Blisks with Friction Ring Damper

3.1. Introduction

One of the challenges of gas turbine engines is that bladed disks under severe operating conditions can experience high vibration levels and resonances. Once the driving frequency is close to any one of the system's natural frequencies, blades can experience high cycle fatigue and failure. Therefore, avoiding excessive vibrations has been an important issue to prevent blade failures. To extend the working life of bladed disks, there have been many efforts to reduce vibrational amplitudes by introducing specific devices and by improved designs [67, 68]. In particular, friction is a major source of damping adopted to dissipate vibration energy.

Various types of friction dampers have been studied. For example, shroud contacts and under-platform dampers have been studied extensively [69, 35, 70, 71, 72, 73]. Those types of dampers act between a vibrating surface on the blade and a rigid structure (such as a cover plate) or between neighboring blades. However, integrally bladed disks (blisks) where the blades and the disk are manufactured as one single piece have no inherent contact surfaces for energy dissipation via friction. Therefore, ring-shaped substructures have been proposed as a damper solution for blisks [39, 40, 41, 42, 43]. Dry friction ring dampers are substructures of blisk system's located inside dedicated grooves under the rim. Ring dampers maintain contact with the blisk due to centrifugal effects (Fig. 13).

Structures with frictional contacts between components can be modeled using finite element (FE) analysis. However, their dynamic analysis is complicated and nonlinear. Due to the complexity of the nonlinear behavior of friction dampers in bladed disk systems, several computational methods have been suggested. The most commonly used method for obtaining the response of nonlinear structures is direct numerical integration of the equations of motion[44, 45, 46]. Numerical integration can be used to determine time-varying displacements, strains, stresses, and forces in a structure as it responds to a combination of static, transient, and harmonic loads. This approach calculates the dynamic responses and loads for all degrees of freedom (DOFs) at all FE nodal points in the most accurate manner; however, it requires very heavy computation and tremendous time. Thus, the harmonic balance method (HBM) is often applied to reduce the computational cost.

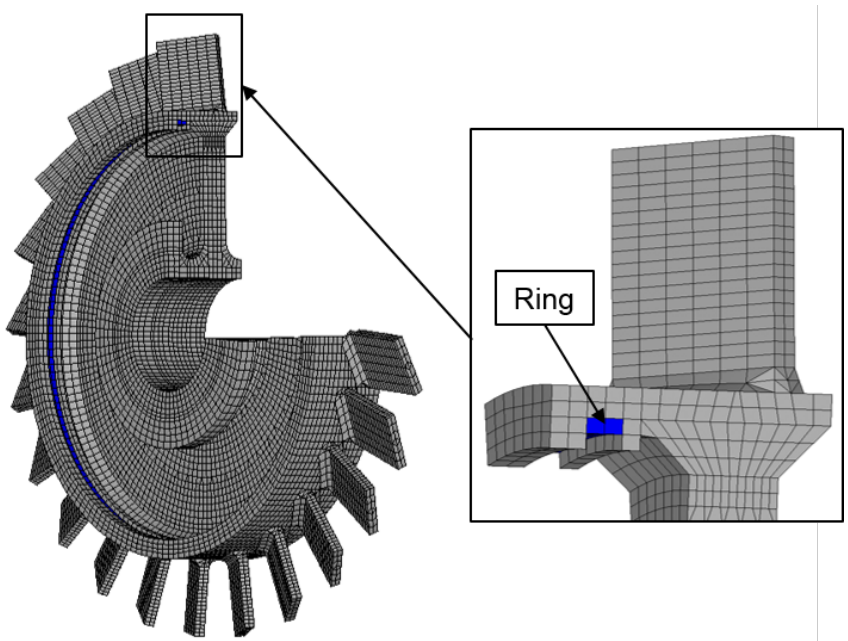

Figure 13: Blisks and ring damper FE model

Frequency-domain methods such as HBM allow for a significant reduction in computational costs compared to time-domain numerical integration[39, 34, 47, 48, 49, 50, 51]. Although the HBM method is efficient for large FE models, the computational cost is still expensive due to the large number of governing equations caused by the many DOFs involved in the nonlinearity.

To address this issue, efficient reduced-order models (ROMs) are proposed herein. Specifically, a new method for the prediction of the nonlinear steady-state response of a bladed disk system with a friction ring damper is presented. An isolated pair of modes is introduced in the transformation matrix together with additional basis vectors which can capture the relative motions between the contact surfaces. In the ROMs, the nonlinear parameters due to the friction force at the contact interfaces (between the disk and the ring damper) are expressed as equivalent structural damping and stiffness in the form of response-dependent matrices. The energy dissipation due to friction is pre-calculated under traveling wave motion by using a sector model, and the dissipation mechanism is integrated into a full wheel system. The equations of motion are converted into a set of nonlinear algebraic equations and solved iteratively. Since ROMs have relatively small size, they can reduce drastically the computational time needed to obtain the nonlinear forced response. The proposed ROMs are validated by comparing their predictions of forced responses under traveling wave excitation with results from time integration of the full FE model.

3.2. Vibration analysis of ring damper system

3.2.1. Harmonic response under traveling wave excitation

Turbomachinery bladed disks are cyclically symmetric structures which can be obtained by successive rotations of one of their sectors even in the case of nonlinear vibrations [74]. The equations of motion of a bladed disk system can be written as

$$\mathbf{M}\ddot{\mathbf{X}}(t) + \frac{\beta}{\omega}\mathbf{K}\dot{\mathbf{X}}(t) + \mathbf{K}\mathbf{X}(t) + \mathbf{F}_{nl}(t) = \mathbf{F}(t), \tag{24}$$

where $\mathbf{M}$ and $\mathbf{K}$ are the mass and stiffness matrices, β is the structural damping coefficient, $\mathbf{X}(t)$ is the vector of displacements measured from the pre-stressed equilibrium, $\mathbf{F}_{nl}(t)$ is the vector of nonlinear forces, $\mathbf{F}(t)$ is the vector of external harmonic excitations of frequency ω, and i is the imaginary unit. Note that the stiffness matrix $\mathbf{K}$ is from the slip state and does not contain the tangential stiffness at the contact surfaces. The effects of the tangential forces at the contact are captured in $\mathbf{F}_{nl}(t)$. With an engine order EO and frequency ω, the external harmonic force of each sector can be expressed as a rotating component [66] as

$$\mathbf{F}_j = \Re\{\mathbf{F}_1 e^{[-i(\omega t-(j-1)\frac{2\pi EO}{N})]}\}, \quad (j = 1, \cdots, N) \tag{25}$$

where $\mathbf{F}_1$ denotes the complex amplitude vector of the excitation applied in the reference sector, j is the index of the sector, and N is the number of sectors. The first sector is chosen as the reference sector of the cyclic structure. If it is assumed that the blisk vibrates periodically with the same nodal diameter pattern as the engine order of the external harmonic excitation, the displacements of the cyclic structure can also be expressed as a function of the reference sector as

$$\mathbf{X}_j(t) = \Re\{\mathbf{x}(t)e^{-i(j-1)\frac{2\pi EO}{N}}\}, \tag{26}$$

where $\mathbf{x}$ refers to the complex vector of displacements of the reference sector. Vector $\mathbf{x}$ can be expressed as

$$\mathbf{x}(t) = (\mathbf{u} + i\bar{\mathbf{u}})qe^{i(\omega t-\varphi)}, \tag{27}$$

where vectors $\mathbf{u}$ and $\bar{\mathbf{u}}$ are a pair of real vectors defined for the reference sector, q is the real value of the amplitude of the response, and φ is the phase lag between the excitation and the response of the system. Vectors $\mathbf{u}$ and $\bar{\mathbf{u}}$ are orthogonal and normalized at a system level instead of a sector level. By generalizing Eq. (51), the harmonic response of the system can be described as a linear combination of modeshapes and their modal amplitudes as

$$\mathbf{X}_j(t) = \begin{bmatrix}\mathbf{\Phi}_j(t) & \bar{\mathbf{\Phi}}_j(t)\end{bmatrix}\hat{\mathbf{q}}, \tag{28}$$

where

$$\begin{aligned}
\mathbf{\Phi}_j(t) &= \mathbf{u}cos\left(\omega t-(j-1)\frac{2\pi p}{N}\right) + \bar{\mathbf{u}}sin\left(\omega t-(j-1)\frac{2\pi p}{N}\right),\\
\bar{\mathbf{\Phi}}_j(t) &= \mathbf{u}sin\left(\omega t-(j-1)\frac{2\pi p}{N}\right) - \bar{\mathbf{u}}cos\left(\omega t-(j-1)\frac{2\pi p}{N}\right),\\
\hat{\mathbf{q}} &= q\begin{bmatrix}cos\varphi & sin\varphi\end{bmatrix}^T,
\end{aligned} \tag{29}$$

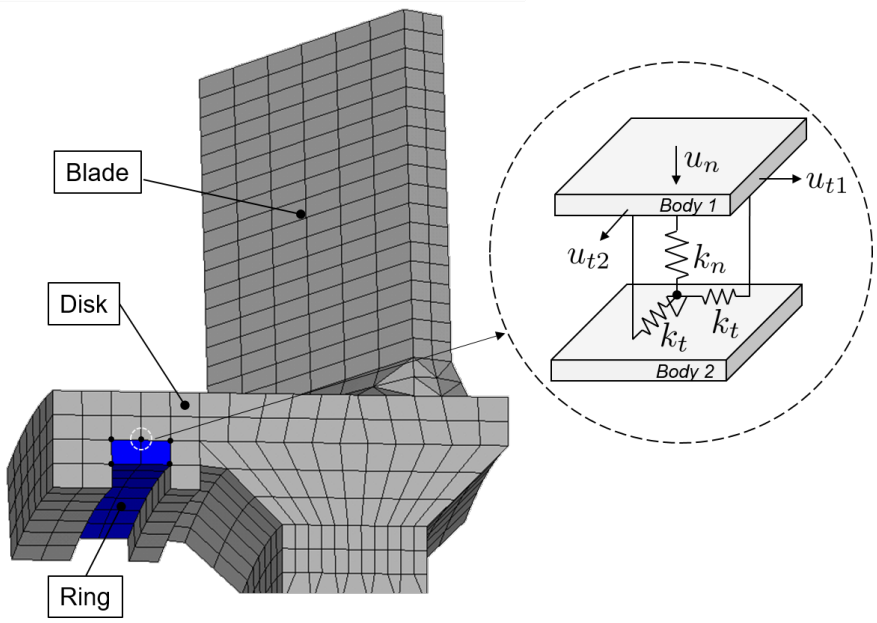

Figure 14: Contact model

where $\mathbf{\Phi}_j$ and $\bar{\mathbf{\Phi}}_j$ are the modeshapes fixed to the rotating frame corresponding to the traveling wave excitation, p is the nodal diameter of the dominant mode pair, and $\hat{\mathbf{q}}$ is the vector of modal amplitudes. Note that $\dot{\mathbf{\Phi}}_j = \omega\bar{\mathbf{\Phi}}_j$, $\dot{\bar{\mathbf{\Phi}}}_j = -\omega\mathbf{\Phi}_j$. Vectors $\mathbf{\Phi}$ and $\bar{\mathbf{\Phi}}$ can be defined for the entire system by grouping vectors $\mathbf{\Phi}_j$ and $\bar{\mathbf{\Phi}}_j$ for all j. Note that $\mathbf{\Phi}^T\mathbf{K}\mathbf{\Phi} = \bar{\mathbf{\Phi}}^T\mathbf{K}\bar{\mathbf{\Phi}} = \omega_n^2$, where ω_n is the natural frequency of the bladed disk system in the slip state corresponding to modeshape $\mathbf{\Phi}$.

3.2.2. Contact modeling and hysteresis curve

In the FE model, the interface between the ring damper and the disk is modeled as distributed discrete contact points. At each pair of contact points, additional stiffnesses are used to account for the elasto-plastic shear deformation [34]. The contact elements contain three linear springs: one normal stiffness k_n in the direction normal to the contact surfaces, and two orthogonal tangential stiffness k_t in the contact plane (Fig. 14). The contact force F changes based on the three possible contact states: stick, slide and separation. When the two bodies undergo tangential stick-slip, the frictional contacts are assumed to obey the Coulomb friction law. When contact elements are stuck, exhibiting no slip motion, F increases proportional to the tangential stiffness. When the contact is in slip, F is equal to the maximum friction force μF_N, where μ is the friction coefficient, and F_N is the normal force at that contact. The transition from the stick state to the slip state occurs when the contact force F is equal to the maximum friction force μF_N. If the bodies move toward the negative u_n direction, the contact normal load may vanish. This causes the interface to separate. In this study, however, the separation is neglected because the centrifugal forces maintain the contact surfaces always in contact by pressing toward the positive direction of u_n.

In modeling dry friction damping mechanisms, the entire friction surface is modeled as an elastic body,

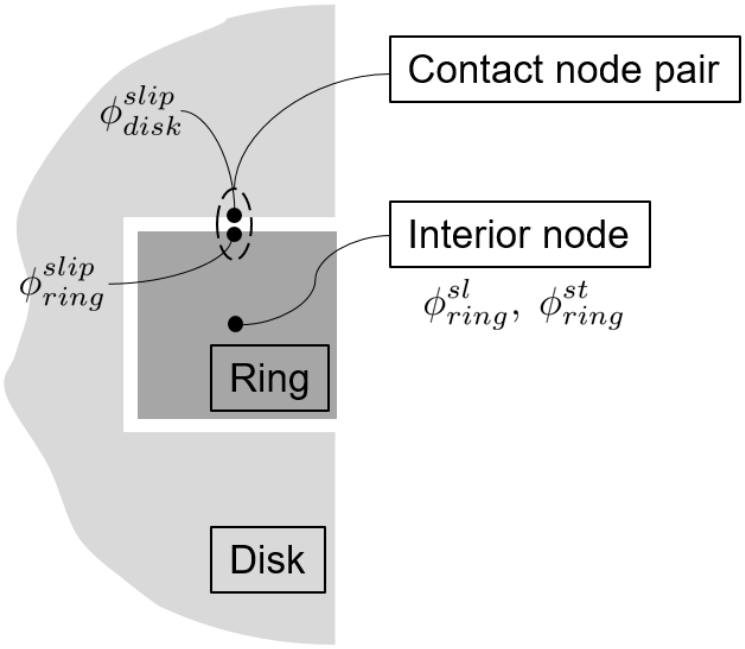

Figure 15: Contact node pairs and interior nodes for the contact model

which enables local relative motion with sliding. Therefore, energy dissipation can be obtained even only with localized relative motions at the contact surface. To obtain the energy dissipation at the contact surfaces during a period of the motion, a quasi-static analysis is introduced. The steady-state motion due to the periodic traveling excitation is described using Eqs. (28) and (55) as

$$\mathbf{X}(t) = \tilde{\mathbf{\Phi}}(t)q, \tag{30}$$

where $\tilde{\mathbf{\Phi}} = \left[\mathbf{\Phi} \quad \bar{\mathbf{\Phi}}\right] [cos\varphi \;\; sin\varphi]^T$. The friction forces $\mathbf{F}_f$ resulting from the quasi-static motion can be obtained for this given motion. However, relative motions only occur between the contact surfaces, and the friction force $\mathbf{F}_f$ only exists at the interface DOFs. Also, the relative motions are expressed using relative displacements of the slip modeshapes which dominate the dynamics. The relative motion $\mathbf{\Phi}^{rel}$ due to motion along those modeshapes is obtained by subtracting the motion of the nodes of the disk and from the motion of the nodes of the ring at the interface.

The cross section of the ring and the damper is sketched in Fig. 15. The dark grey rectangle and the light grey shape represent the ring and disk. At each contact node pair, the relative motion (in each of the two directions along the contact surface; directions r and θ in Fig. 15) is captured by subtracting the displacement of the disk ϕ_{disk}^{slip} from that of the ring ϕ_{ring}^{slip}, namely $\phi_{contact}^{rel} = \phi_{ring}^{slip} - \phi_{disk}^{slip}$, where superscript *slip* indicates a modeshape of the system in slip.

Since the motion caused by a traveling wave excitation has a symmetric pattern around the rotor, each sector undergoes the same pattern of response during a cycle of the traveling excitation. Therefore, the

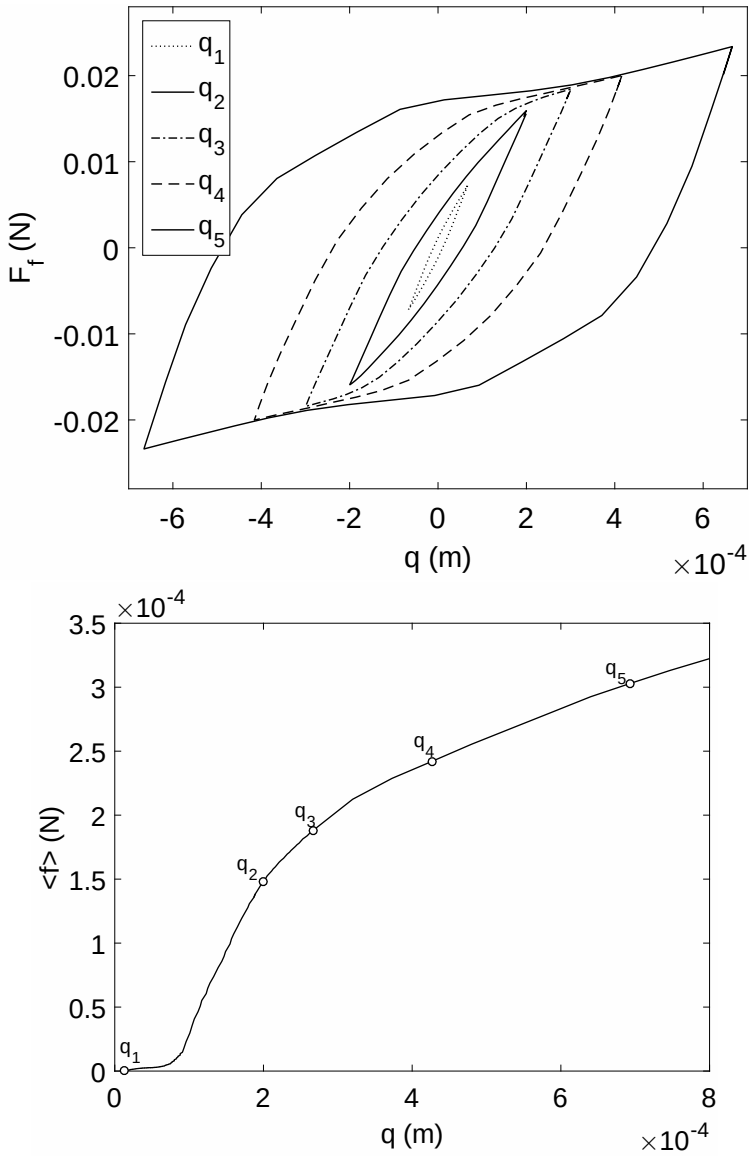

Figure 16: Examples of hysteresis loops and modal friction forces given by Eq. (61) for various modal amplitudes: $q_1 = 1.0 \cdot 10^{-5}$; $q_2 = 3.0 \cdot 10^{-4}$; $q_3 = 4.5 \cdot 10^{-4}$; $q_4 = 6.2 \cdot 10^{-4}$; $q_5 = 1.0 \cdot 10^{-3}$

forces in the full-order system during a revolution can be obtained from a sector level analysis. The friction force of the full system projected onto the vector of relative displacements $\mathbf{\Phi}^{rel}$ can be expressed as

$$\begin{aligned} f(t) &= \mathbf{\Phi}^{rel^T} \mathbf{F}_f \left(\mathbf{X}(t) \right) \\ &= \sum_{j=1}^{N} \mathbf{\Phi}_j^{rel^T} \mathbf{F}_{f,j}(\mathbf{X}_j(t)) = N \mathbf{\Phi}^{rel^T}_1 \mathbf{F}_{f,1}(\mathbf{X}_1(t)), \end{aligned} \tag{31}$$

where $\mathbf{F}_f$ is the friction force on the contact surfaces, $\mathbf{\Phi}_1^{rel}$ is the vector of relative displacements in sector j, and $\mathbf{F}_{f,j}$ is the friction force at the contact surfaces in sector j. The average friction force projected onto

the relative displacement is obtained by taking the average value of the friction force in Eq. (59) to obtain

$$< f >= \frac{1}{T}\int_{T} f(t)d(\omega t) = \frac{1}{2\pi}\int_{0}^{2\pi} f\left(\frac{\theta}{\omega}\right)d\theta. \tag{32}$$

Note that $f\left(\frac{\theta}{\omega}\right)$ is a function which depends explicitly only on θ and not on ω because the time t appears only in terms of ωt.

3.2.3. Equivalent nonlinear damping and stiffness

Hysteresis loops establish the relationship between the input displacements and the resulting friction forces. Examples of such loops are plotted in Fig. 16. These loops are obtained from a motion along the second mode (nodal diameter 1 in the first mode family). Each loop is created under different modal amplitudes.

The energy dissipated by the friction force is the area inside the loop. The dissipated energy is a function of the physical relative displacement at the contact pairs during slip. Therefore, as the modal amplitude increases, slip motions between contact pairs grow from a few to the entire contact surface. This mechanism corresponds to an increase in area inside the hysteresis loop. Once the motion reaches full slip, in which the entire contact surface slips, the growth of the area slows down, starting to linearly increase with the amplitude.

The area inside the hysteresis loop is independent of the velocity of the motion, but depends on the amplitude of the displacements. This type of energy dissipation is called hysteresis damping or structural damping. Hysteresis damping is often expressed in complex form as $i\gamma\mathbf{K}$, where γ is a structural damping factor [75, 76, 77], and $\mathbf{K}$ is the stiffness matrix.

The nonlinear force $\mathbf{F}_{nl}$ associated with friction comprises locally elastic restoring forces (stick phase) and dissipative forces (slide phase) at the contact surfaces. An equivalent structural damping coefficient γ is defined to account for the energy dissipation due to $\mathbf{F}_{nl}(t)$ at the contact. Over a period of motion, the dissipated energy from a structural damping force in a traveling wave response can be expressed as

$$\begin{aligned} W_c &= \oint_{D} j\gamma\left(\mathbf{K}\mathbf{X}\right)^T d\mathbf{X} \\ &= \frac{\gamma}{\omega}\int_{T} \dot{\mathbf{X}}^T\mathbf{K}\dot{\mathbf{X}}dt \\ &= \frac{\gamma}{\omega}\int_{T} -\omega\tilde{\bar{\mathbf{\Phi}}}^T q\mathbf{K}(-\omega\tilde{\bar{\mathbf{\Phi}}}q)dt \\ &= \gamma\omega q^2\int_{T}\omega_n^2 dt \\ &= 2\pi\gamma\omega_n^2 q^2, \end{aligned} \tag{33}$$

where $\mathbf{X} = \tilde{\mathbf{\Phi}}q$, and thus $\dot{\mathbf{X}} = -\omega\tilde{\bar{\mathbf{\Phi}}}q$, where $\tilde{\bar{\mathbf{\Phi}}} = \begin{bmatrix}\bar{\mathbf{\Phi}} & -\mathbf{\Phi}\end{bmatrix}[cos\varphi \;\; sin\varphi]^T$. Note also that $\tilde{\mathbf{\Phi}}^T\mathbf{K}\tilde{\mathbf{\Phi}} = \tilde{\bar{\mathbf{\Phi}}}^T\mathbf{K}\tilde{\bar{\mathbf{\Phi}}} = \omega_n^2$. A stiffness matrix $\mathbf{K}_f$ is defined to account for the elastic effects in the contact. The average

elastic energy in the contact can be expressed using the equivalent stiffness matrix $\mathbf{K}_f$ as

$$\begin{aligned} W_s &= \frac{1}{T}\int_0^T \mathbf{X}^{rel^T}\mathbf{K}_f\mathbf{X}^{rel}dt \\ &= \frac{1}{T}\int_0^T q\mathbf{\Phi}^{rel^T}\mathbf{K}_f\mathbf{\Phi}^{rel}qdt \\ &= \frac{\omega}{2\pi}\int_0^{2\pi} k_f q^2\frac{d\theta}{\omega} \\ &= k_f q^2, \end{aligned} \tag{34}$$

where $\mathbf{X}^{rel} = \mathbf{\Phi}^{rel}q$ is the relative displacement at the contact surfaces, and $k_f = \mathbf{\Phi}^{rel^T}\mathbf{K}_f\mathbf{\Phi}^{rel}$. Equivalently, the energy dissipation due to the friction force $\mathbf{F}_f$ is obtained as

$$\begin{aligned} E_c &= -\int_T \mathbf{F}_f^T\dot{\mathbf{X}}^{rel}dt = -\int_T \mathbf{F}_f^T\dot{\mathbf{\Phi}}^{rel}qdt \\ &= -\int_T \mathbf{F}_f^T(-\omega\bar{\mathbf{\Phi}}^{rel})qdt \\ &= 2\pi\left(\frac{1}{2\pi}\int_0^{2\pi}\mathbf{F}_f^T\bar{\mathbf{\Phi}}^{rel}d\theta\right)q \\ &= 2\pi < \bar{f} > q, \end{aligned} \tag{35}$$

where $\bar{\mathbf{\Phi}}^{rel}$ is defined (similar to $\mathbf{\Phi}^{rel}$) as the difference between the ring and the disk motions in $\bar{\mathbf{\Phi}}$, and hence $\dot{\mathbf{\Phi}}^{rel} = -\omega\bar{\mathbf{\Phi}}^{rel}$ (similar to $\dot{\mathbf{\Phi}} = -\omega\bar{\mathbf{\Phi}}$). Also, $\bar{f}$ is defined as $\bar{f} = \bar{\mathbf{\Phi}}^{rel^T}\mathbf{F}_f$, and the average stored energy due to the friction force $\mathbf{F}_f$ is

$$\begin{aligned} E_s &= \frac{1}{T}\int_T \mathbf{F}_f^T\mathbf{X}^{rel}dt = \frac{\omega}{2\pi}\int_T \mathbf{F}_f^T\mathbf{\Phi}^{rel}q\frac{d\theta}{\omega} \\ &= \frac{1}{2\pi}\int_0^{2\pi}\mathbf{F}_f^T\mathbf{\Phi}^{rel}d\theta q \\ &= < f > q. \end{aligned} \tag{36}$$

Note that $\mathbf{\Phi}^{rel^T}\mathbf{F}_f = f$ as shown in more detail in Eq. (59).

The dissipated energy at the contact interface in the form of structural damping in Eq. (64) and the energy dissipation by the friction force in Eq. (63) are defined to be the same. Thus, the expression of the equivalent damping factor is

$$\gamma = \frac{< \bar{f} >}{\omega_n^2 q}. \tag{37}$$

Likewise, the average elastic energy in the contact in Eq. (65) and the average energy stored due to the friction force in Eq. (62) are defined to be the same. Thus, the equivalent stiffness at the contact pair can

be written as

$$k_f = \frac{< f >}{q}. \tag{38}$$

3.2.4. Reduced order modeling

A FE model of a turbomachinery bladed disk with a ring damper is shown in Fig. 13. In the stick state, contact pairs are linked with springs adding shear stiffness to the system. In the slip state, however, all contact pairs are maintained in contact without stiffness in the tangential direction. The key idea of this study is to capture the relative motion between the disk and the ring to predict the friction force and the energy dissipation. Thus, a transformation matrix is constructed by using the modeshapes from the stick state together with additional vectors which can describe the relative motions. Thus, the response of the bladed disk and ring system is approximated as

$$\mathbf{X}_j = \begin{bmatrix} \mathbf{X}_{j,B} \\ \mathbf{X}_{j,R} \end{bmatrix} = \underbrace{\begin{bmatrix} \boldsymbol{\Phi}^{st}_{j,B} & \mathbf{0} & \bar{\boldsymbol{\Phi}}^{st}_{j,B} & \mathbf{0} \\ \boldsymbol{\Phi}^{st}_{j,R} & \boldsymbol{\Phi}^{rel}_{j,R} & \bar{\boldsymbol{\Phi}}^{st}_{j,R} & \bar{\boldsymbol{\Phi}}^{rel}_{j,R} \end{bmatrix}}_{\mathbf{T}_j} \begin{bmatrix} \mathbf{q}^{st} \\ \mathbf{q}^{rel} \\ \bar{\mathbf{q}}^{st} \\ \bar{\mathbf{q}}^{rel} \end{bmatrix} = \mathbf{T}_j \mathbf{q}, \tag{39}$$

where B refers to DOFs of the blade together with the disk, R refers to DOFs of the ring, and $\boldsymbol{\Phi}^{rel}_{j,R}$ is a vector which characterizes the relative motion of the ring with respect to the disk. On the contact surfaces, $\boldsymbol{\Phi}^{rel}_{j,R}$ is the same as $\boldsymbol{\Phi}^{rel}_{j}$. In the interior nodes shown in Fig. 15, $\boldsymbol{\Phi}^{rel}_{j,R}$ is defined as $\phi^{sl}_{ring} - \phi^{st}_{ring}$ (the difference between corresponding slide and stick modes in the ring). Note that the size of the matrix $\mathbf{T}_j$ is the number of physical DOFs in a single sector by the total number of modes contained in $\boldsymbol{\Phi}^{st}$, $\boldsymbol{\Phi}^{rel}$, $\bar{\boldsymbol{\Phi}}^{st}$ and $\bar{\boldsymbol{\Phi}}^{rel}$, which is denoted by m. A similar but distinct concept was used by Chen and Menq [78] to obtain a transformation basis. In their work, they introduced a constrained mode together with a free mode to predict the resonant response of a frictionally constrained blade system. The constrained modes are obtained from a FE model of the blade in which the contact is considered lumped at a single point, and that point is connected to the ground with springs. In this study, however, both of the contact bodies are elastic and moving. Thus, the contact cannot be lumped at a single point. Also, the relative motion between the contact points has to be captured correctly, e.g. by using the slip and the stick modes. The current method uses $\boldsymbol{\Phi}^{rel}_{j,R}$ and $\bar{\boldsymbol{\Phi}}^{rel}_{j,R}$ to address this issue.

Once the ring is fully stuck, the magnitude of the relative coordinate $\mathbf{q}^{rel}$ approaches 0. In contrast, for the frictionless condition, the ring slips and the magnitude of the relative motion $\mathbf{q}^{rel}$ has a magnitude similar to the magnitude of $\mathbf{q}^{st}$.

The mass and stiffness matrices in Eq. (50) are block matrices comprised of matrices $\mathbf{M}_j$, with $j = 1, \cdots, N$. Each matrix $\mathbf{M}_j$ is the free-interface mass matrix for the j^{th} sector. Expanding the transformation matrix into the system level with duplicated modal information at each sector interface, and plugging the transformation matrix $\mathbf{T}_j$ into Eq. (50), the equation of motion can be written as

$$\left[-\omega^2 \mathbf{m} + (i\beta + 1)\mathbf{k}\right] \mathbf{q} + \mathbf{f}_{nl} = \mathbf{f}_{ex}, \tag{40}$$

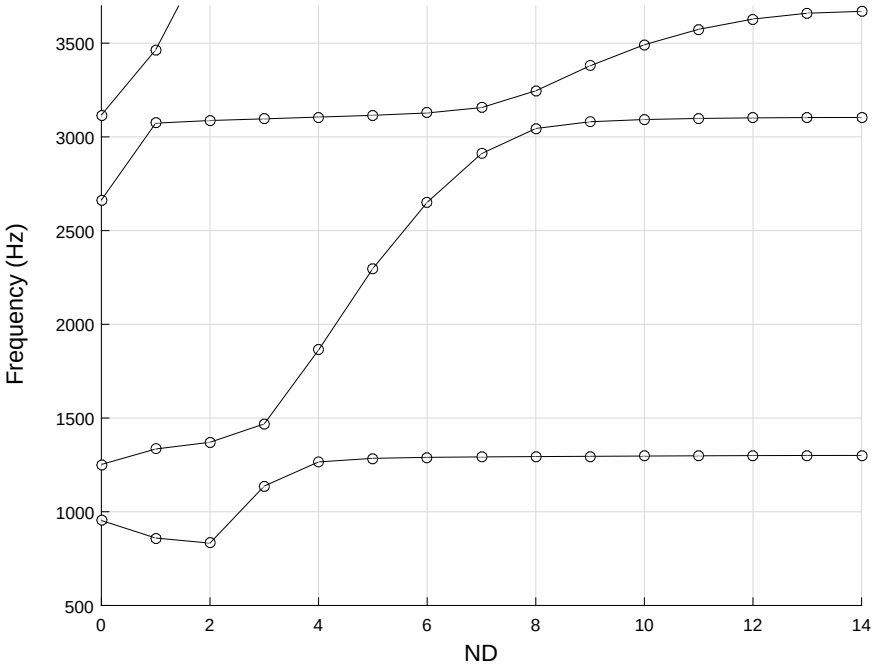

Figure 17: Frequency vs. nodal diameter plot

where $\mathbf{m}$ is the reduced mass matrix ($\mathbf{m} = \sum_{j=1}^{N} \mathbf{T}_j^T \mathbf{M}_j \mathbf{T}_j$), $\mathbf{k}$ is the reduced stiffness matrix where the contact surfaces are in full slip, and β is the structural damping coefficient for the blisk structure. The stiffness matrix $\mathbf{k}$ can be expressed as

$$\mathbf{k} = \mathbf{k}^{st} - \mathbf{k}_f^o, \tag{41}$$

where

$$\mathbf{k}^{st} = \sum_{j=1}^{N} \mathbf{T}_j^T \mathbf{K}_j^{st} \mathbf{T}_j. \tag{42}$$

Note that $\mathbf{k}_f^o$ is a reduced stiffness matrix which accounts for the tangential stiffness at the contact pairs, and the matrix $\mathbf{k}_f^o$ is obtained in the calculation of the equivalent stiffness when the relative motion between the contact are nearly zero ($\mathbf{q} \approx \mathbf{0}$).

As described earlier, the nonlinear force $\mathbf{f}_{nl}$ is characterized as equivalent damping and stiffness matrices as

$$\mathbf{f}_{nl} \cong (i\mathbf{\Gamma} \circ \mathbf{k}_f + \mathbf{k}_f)\mathbf{q}, \tag{43}$$

where $\circ$ is the Hadamard product, $\mathbf{\Gamma}$ is the equivalent damping matrix, and $\mathbf{k}_f$ is the equivalent stiffness matrix, respectively. The elements of the equivalent damping matrix $\mathbf{\Gamma}$ and the equivalent stiffness matrix $\mathbf{k}_f$ are defined differently depending on the motion and corresponding projection. Their elements are defined

as

$$\gamma_{(\zeta,\xi)} = \frac{N}{q}\left[\frac{1}{2\pi}\int_0^{2\pi} \mathbf{T}_{j,\zeta}^T \mathbf{F}_f\left(\bar{\mathbf{T}}_{j,\xi} q\right)\frac{d\theta}{\omega}\right],$$
$$k_{f(\zeta,\xi)} = \frac{N}{q}\left[\frac{1}{2\pi}\int_0^{2\pi} \mathbf{T}_{j,\zeta}^T \mathbf{F}_f\left(\mathbf{T}_{j,\xi} q\right)\frac{d\theta}{\omega}\right], \tag{44}$$
$$(\zeta,\ \xi = 1, \cdots, m),$$

where $\gamma_{(\zeta,\xi)}$ and $k_{f(\zeta,\xi)}$ are the elementss of the equivalent damping and the equivalent stiffness matrices, respectively. ζ and ξ indicate columns of $\mathbf{T}_j$ and $\bar{\mathbf{T}}_j$, where the matrix $\mathbf{T}_j$ is given in Eq. (68) and the matrix $\bar{\mathbf{T}}_j$ is defined as

$$\bar{\mathbf{T}}_j = \begin{bmatrix} \bar{\mathbf{\Phi}}_{j,B}^{st} & \mathbf{0} & \mathbf{\Phi}_{j,B}^{st} & \mathbf{0} \\ \bar{\mathbf{\Phi}}_{j,R}^{st} & \bar{\mathbf{\Phi}}_{j,R}^{rel} & \mathbf{\Phi}_{j,R}^{st} & \mathbf{\Phi}_{j,R}^{rel} \end{bmatrix}. \tag{45}$$

Plugging Eqs. (72) and (73) into Eq. (69), the equation of motion the bladed disk and ring system can be written as

$$[-\omega^2\mathbf{m} + (i\beta+1)(\mathbf{k}^{st} - \mathbf{k}_f^o) + i\mathbf{\Gamma}\circ\mathbf{k}_f + \mathbf{k}_f]\mathbf{q} = \mathbf{f}_{ex}. \tag{46}$$

3.3. Solution method

In this section, the procedure to obtain the ROM is summarized, and an iterative solution method is introduced. A flow chart is provided in Fig. 18 to help understand the ROM procedure as

1. The sector level 3D ring and damper FE model is constructed. The modeshapes of the slip state (no constraints to the tangential direction) $\mathbf{\Phi}^{sl}$, and the stick state (connecting the contact pairs with tangential springs) $\mathbf{\Phi}^{st}$, are obtained (prohibiting separation at the contact surfaces).
2. The dissipated energy in Eq. (63) and the average stored energy in Eq. (62) due to the friction force are calculated quasi-statically using just one sector. The motion is described by the modeshapes and is proportional to the modal amplitudes $\mathbf{q}$ as in Eq. (68). The projected friction forces are computed from these single sector calculations using Eqs. (59) and (61).
3. The equivalent damping $\mathbf{\Gamma}$ and stiffness $\mathbf{k}_f$ matrices are computed with respect to the modal amplitudes using Eq. (74).
4. The transformation matrix in Eq. (68) is introduced in the equations of motion to construct the ROM in Eq. (75) by calculating metrices $\mathbf{m}$ and $\mathbf{k}^{st}$. The nonlinear force in the ROM is described by the equivalent damping and stiffness matrices $\mathbf{k}_f^o$, $\mathbf{k}_f$ and $\mathbf{\Gamma}$.

Due to existence of the nonlinear forces, there is an equivalent linear complex stiffness in the ROM. Since the equivalent damping and stiffness are amplitude dependent, the ROM cannot be solved explicitly. Nonetheless, the response of the system to an external harmonic force can be obtained by solving Eq. (75) iteratively. First, Eq. (75) is re-written as

$$\mathbf{\Theta}^{-1}\mathbf{q} = \mathbf{f}_{ex}, \tag{47}$$

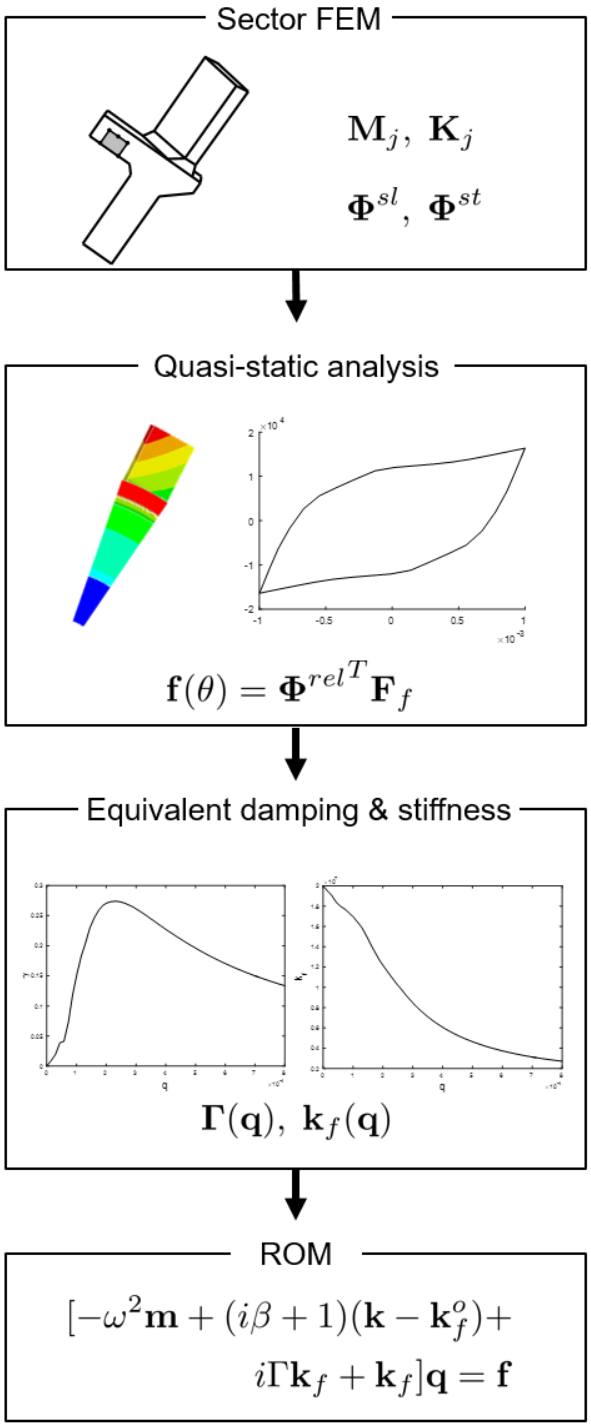

Figure 18: Flow chart of ROM procedures

where

$$\mathbf{\Theta} = \left[-\omega^2\mathbf{m} + (i\beta+1)(\mathbf{k}-\mathbf{k}_f^o) + i\mathbf{\Gamma}(\mathbf{q}) \circ \mathbf{k}_f + \mathbf{k}_f(\mathbf{q})\right]^{-1}. \tag{48}$$

Since the nonlinear friction force represented as equivalent damping $\mathbf{\Gamma}$ and equivalent stiffness $\mathbf{k}_f$ matrices

are pre-calculated, $\mathbf{\Theta}^{-1}$ can be obtained quickly.

The following simple iteration scheme can be used at a particular frequency ω

$$\mathbf{q}_{i+1} = \mathbf{\Theta}_i \mathbf{f}_{ex}, \tag{49}$$

Here $\mathbf{q}_{i+1}$ denotes the solution for the modal amplitude vector at the $(i+1)^{\text{th}}$ iteration step, and $\mathbf{\Theta}_i$ is obtained using $\mathbf{q}_i$ from the i^{th} iteration. Iterations continue until the percentage error $e = ||\mathbf{q}_{i+1} - \mathbf{q}_i||/||\mathbf{q}_i||$ drops below a certain value. The equivalent damping and stiffness matrices in Eq. 73 can be obtained before the ROM equations are solved. Their values are used in the solution method. Thus, it is worth to note that this energy balance approach is very close to a single mode harmonic balance method.

3.4. Results

To validate the developed ROM, force response results from the ROM are compared with results obtained by simulations of the full FE model in ANSYS. The bladed disk has 24 blades, and the ring damper has rectangular cross section with three contact surfaces (Fig. 14). The FE model consist of 52,248 nodal points, and SOLID45 elements are used for the entire structure. To construct the contact pairs, TARGE170 and CONTA174 are used for the target and the contact elements, respectively. To calculate the centrifugal force as a pre-stress, the bladed disk is rotated at 10,000 rpm. Steady-state responses under traveling wave excitation are examined.

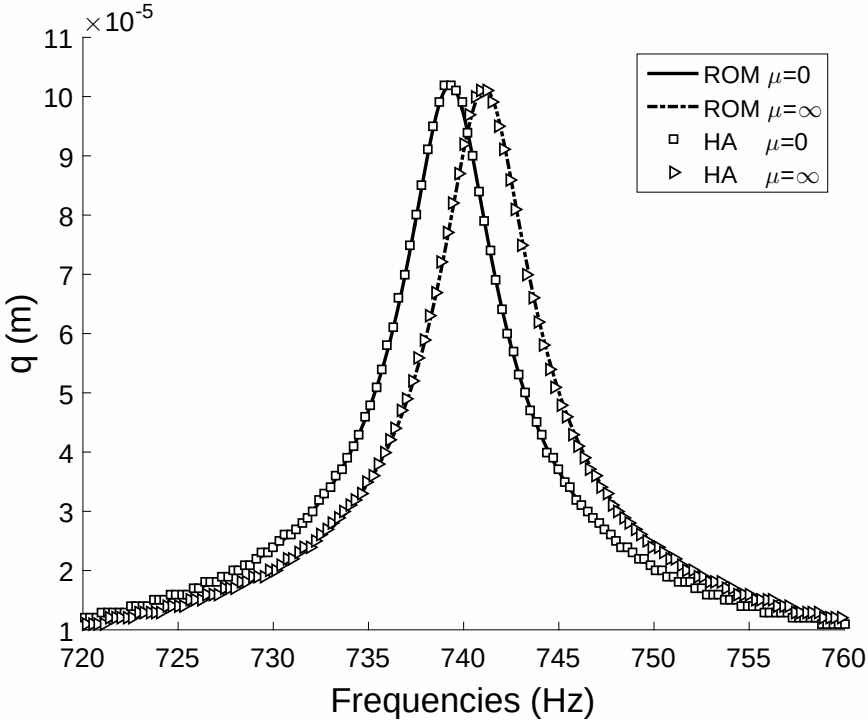

Figure 19: Frequency response plot of harmonic analysis (HA) and reduced order models (ROMs)

The force responses of the bladed disk and ring system with two contact conditions, full slip and full stick, can be obtained by harmonic or frequency-response analysis. Figure 19 shows the predicted responses using the ROM. The response in the slip state shows a peak amplitude at 739.3Hz (the lowest natural frequency

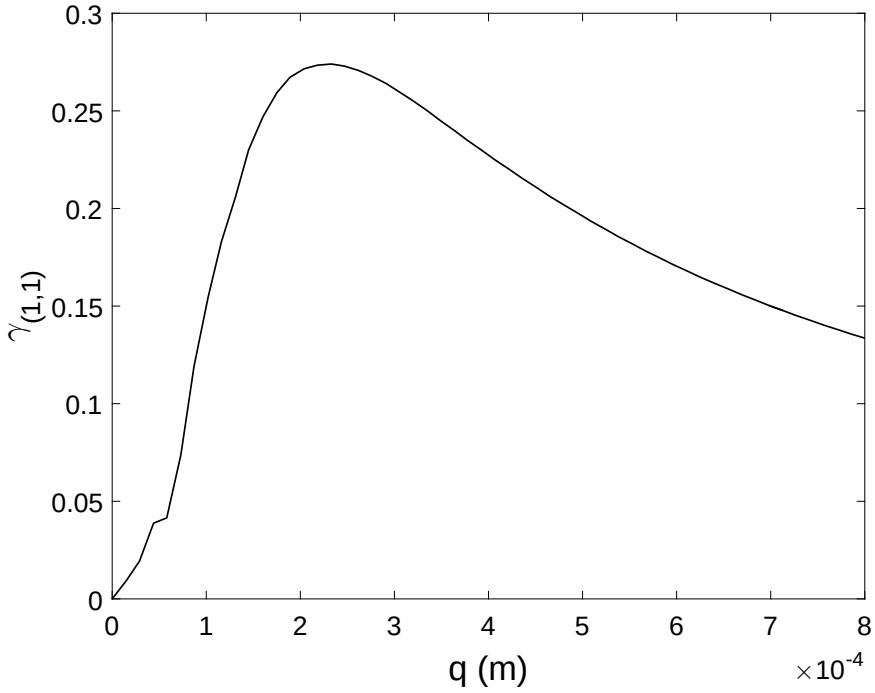

Figure 20: Example of equivalent damping $\gamma_{(1,1)}$

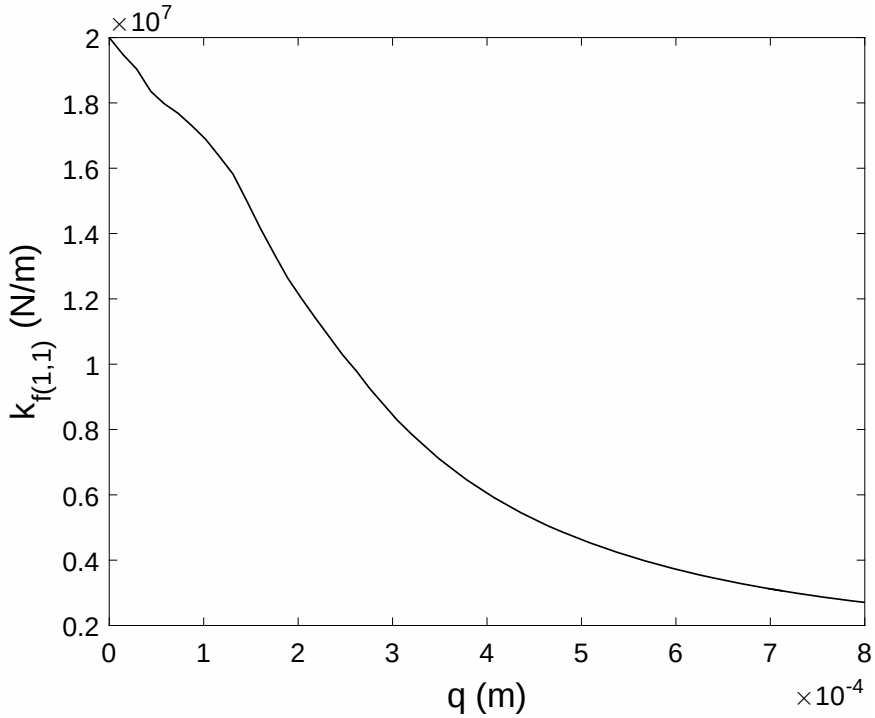

Figure 21: Example of equivalent stiffness $k_{f(1,1)}$

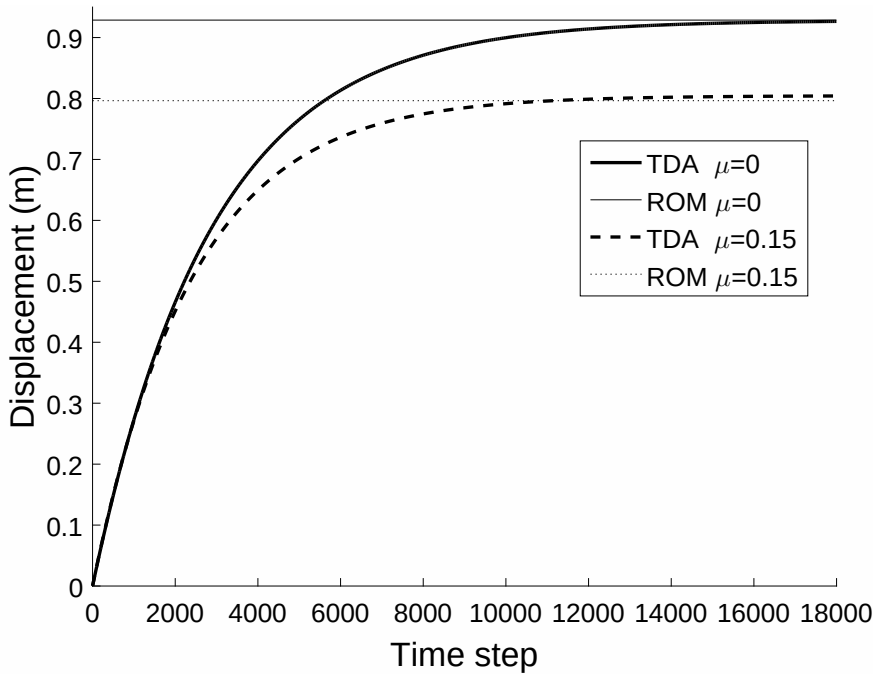

Figure 22: Estimation of steady-state response by ROM and by TDA from full size FE model

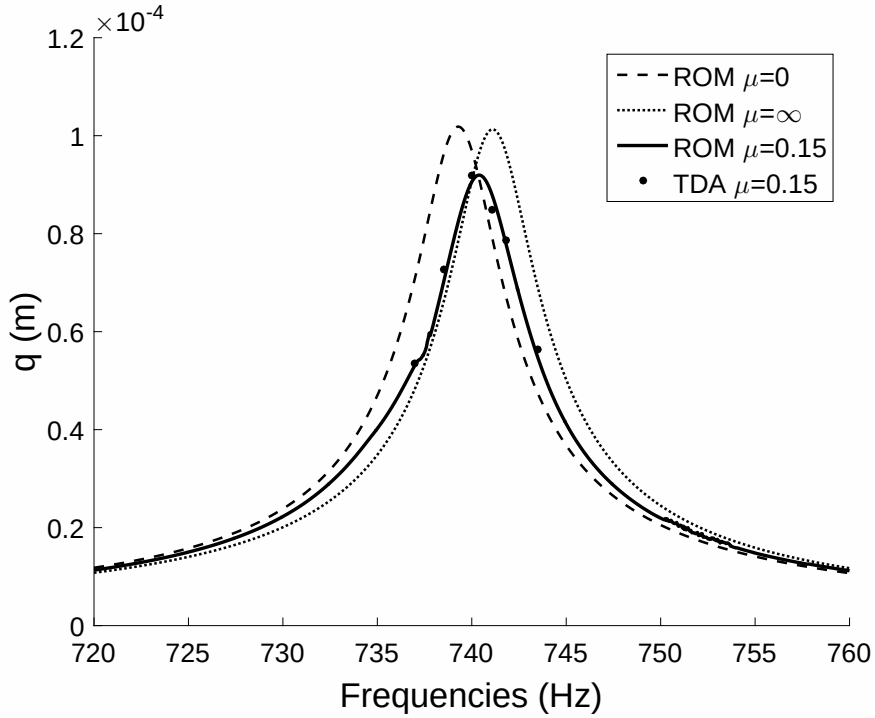

Figure 23: Validation of ROM using TDA results

shown in Fig. 25). In the stick state, the system responds the most at 741.1Hz. The predicted responses show very good match with results from a harmonic analysis (full order in ANSYS).

In the case of the nonlinear system, where stick-slip is involved, transient dynamic analysis (TDA) is

performed in ANSYS. To compute the response at a particular frequency, the bladed disk and ring system is excited at the first resonance with engine order excitation 1. TDA is performed with enough time steps to guarantee convergence at steady-state. To obtain the ROM, the equivalent damping and equivalent stiffness are precalculated by using only single sector calculation. The friction force is calculated quasi-statically by describing the motion corresponding to a traveling wave excitation of engine order 1. The resultant equivalent damping $\gamma_{(1,1)}$ and stiffness $k_{f(1,1)}$ are plotted in Figs. 20 and 21 as a function of q (modal amplitude) using Eq. (74). In Fig. 22, the (physical) amplitudes of motion at the tip of the blade are shown both for the linear ($\mu = 0$) and nonlinear cases ($\mu = 0.15$). After 1.6×10^4 time steps, the responses are assumed to reach steady-state. The steady-state response without friction has higher vibration amplitude compared to the case with friction. The relative error between the amplitudes predicted by the TDA and the ROM is below 0.1%. The amplitude variation with the excitation frequency is plotted in Fig. 23 for three different contact states. Two linear cases, slip ($\mu = 0$) and stick ($\mu = \infty$), are shown together with a nonlinear case ($\mu = 0.15$). The responses on the slip state and the stick state both have relatively the same amplitude. With friction, however, the ring damper dissipates vibration energy so that the system has lower amplitude compared to the linear systems. For more validations, TDA simulations were performed at seven different excitation frequencies. A single TDA takes 168 hours and 30 minutes of computational time for 18,000 time steps. The ROM, however, only takes 5 seconds to predict the whole frequency response in the range of interest and at the engine order of interest. Although the ROM requires approximately10 minutes of preprocessing time for obtaining the equivalent stiffness and damping values, this time is negligible compared to the time integration approach.

3.5. Discussion and conclusions

In this study, new reduced order models are developed to capture the nonlinear behavior due to contact friction. The proposed approach is based on expressing the nonlinear force as response-dependent and iteratively solving the nonlinear system with response-dependent characteristics. The equivalent structural damping and stiffness are substituted for the nonlinear friction forces. To predict the steady-state responses under traveling excitations, the equivalent damping and stiffness values are nonlinear functions obtained by quasi-static analysis with imposed harmonic motions. The pre-calculated nonlinear equivalent damping and stiffness speeds up the iterative solution. A key advantage of the proposed approach is that it requires only sector level calculations to compute the response of the full wheel system. A full size FE model of a bladed disk and a ring damper system was used to demonstrate the method. The ROMs predict the steady-state responses with a significantly reduced computation time, efficiently and accurately.

CHAPTER 4

4. Reduced Order Models for Contact Stiffness Identification Applied to Ring Damper

4.1. Introduction

In the dynamic design of turbine bladed disks, friction is a common source of damping. Friction dampers dissipate the energy of vibration in the form of heat and reduce resonance amplitudes to acceptable levels. The common types of friction damper in turbine bladed disks are the blade-disk interface [79, 33, 32], the shrouds contact at the tip of blades [34, 80, 81], underplatform dampers, and ring dampers. Modeling of friction contacts in structural dynamics has become a major issue in the design of mechanical parts and structures. To predict the dynamic responses of a structure associated with friction, a reliable level of friction modeling is essential. Structures with frictional contacts between components can be modeled using finite element (FE) analysis. Structures with frictional contacts between components can be modeled using finite element (FE) analysis. The reliable modeling of bladed disks with friction dampers depend on understanding and reproducing basic physics associated with friction interfaces. Many studies represent the friction occurring at contact interfaces by a Coulomb friction model [82, 83, 57, 58]. It has been identified that micro- and macro- slip occur along the interface as the source of change of interface stiffness and energy dissipation. The transience of slip and stick constitutes the hysteresis mechanism of the contact interface. Thus, due to the complexity and nonlinear behavior of friction dampers in bladed disk systems, the dynamic analysis using direct numerical integration of the equations of motion of full-order models requires a tremendous amount of computation time. Thus, the harmonic balanced method (HBM) is often applied to reduce the computational cost. In the literature, the HBM method has been utilized to calculate the steady-state response of a nonlinear system. Although the HBM method is efficient for large FE models, the computational cost is still quite expensive due to the large size of the governing equations and iterative solutions required for obtaining the converged solution. To address this issue, efficient reduced-order models (ROMs) are developed **??**. These ROMs, the nonlinear parameters due to the friction force at the contact interface are expressed as equivalent structural damping and stiffness in the form of response-dependent matrices. The equivalent damping coefficient and stiffness are pre-calculated by quasi-static analysis assuming the steady-state response. The developed ROM is relatively small in size, thus drastically reducing the computational time required to obtain the nonlinear forced response.

Parameters at contact interfaces are of great importance to contact dynamics and interface modeling. It is shown that contact stiffness has a significant on the accuracy of the results when it is studied using finite element methods. It is known that up to 90% of the damping and 60% of the deformation in a fabricated structure can arise from various connections [52]. The contact stiffness for the mechanical structure must be identified along with their expected ranges of variation in order to use FE models confidently. Contact surfaces can experience slipping and tension release depending on the magnitude of the normal and tangential forces at the contact interface. Due to its nonlinear behavior, identification of contact stiffness is not straightforward. There have been many efforts to investigate the contact parameters at the mechanical joint analytically [53, 54] and experimentally [55, 56, 57, 58]. Wang and Sas [59] suggested a method for finding the optimal linear joint stiffness and damping parameters from measured modal parameters (resonant frequency and damping ratio), and Ren and Beards [60] presented a method to extract the optimal linear joint parameters by using experimental frequency response data. Although those techniques are available for the identification of nonlinear joint parameters, they are only applicable to those joints with specific configurations, or when dynamic tests are performed on a fixture. In this paper, a more general method for identifying the contact parameters of a bladed disk with friction damper, directly from its observed response is developed. The surrogate measurement data which are the predicted forced responses of a bladed disk with measurement noise are investigated. Based on the developed ROM, an iterative procedure is used to find the optimal parameters which show the least residuals between the measurement data and the predictions. The method is applied to bladed disks with a ring damper system. The final ROMs generated by the procedure are comparable to small lumped parameter models and offer considerable reduction in system dimensionality. Additionally the identification method for the contact parameters by the forced responses are investigated.

4.2. Vibration analysis of bladed disks

4.2.1. Lumped parameter model of a bladed disk with ring damper

Lumped parameter models have been widely studied due to its simplicity and computational efficiency. Qualitative results for friction damping application by using lumped parameter models have been proposed by many researchers [1, 2, 3]. In this paper, we present a new lumped parameter model of a bladed disk with a friction ring damper 24. In the lumped parameter model, disk is modeled as an N degrees of freedom (DOF) system, where N is the number of blades on the disk. In the model, m_d^j, m_r^j, m_{b1}^j and m_{b2}^j stand for j^{th} disk, ring, blade root and blade tip masses, respectively. k_d^j, k_r^j, k_{b1}^j, k_{b2}^j, and k_g^j correspond to the stiffness between the j^{th} and $(j+1)^{\text{th}}$ disk elements, the stiffness between the j^{th} and $(j+1)^{\text{th}}$ ring elements, the root stiffness between the j^{th} disk element and j^{th} blade, the stiffness of the j^{th} blade, and the stiffness of j^{th} disk element constrained to the ground, respectively. At the contact points between the disk and the ring node, a normal stiffness k_n^j and tangential stiffness k_t^j are defined. The friction force changes based on the two contact states: stick and slip. When the two contect elements undergo tangential stick-slip, the frictional contacts are assumed to obey the Coulomb friction law. The friction force increases proportional

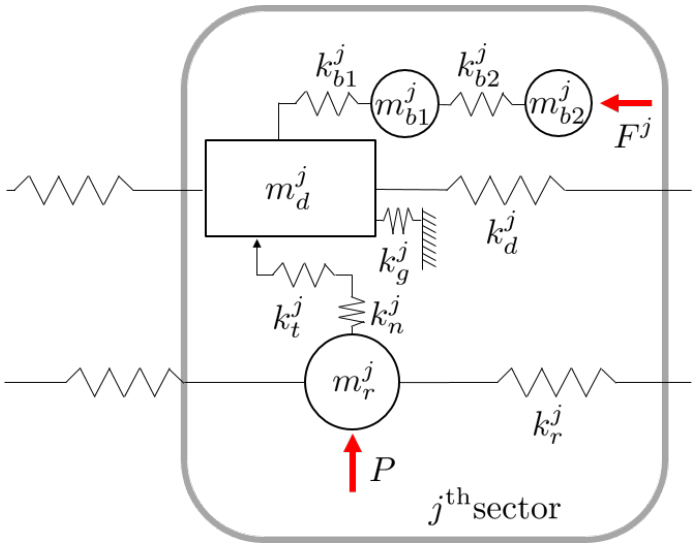

Figure 24: Lumped parameter model of bladed disks with ring damper

to the tangential stiffness when two contact nodes are stuck. When the contact is in slip, the friction force is equal to the maximum friction force μP, where μ is the friction coefficient and P is pre-stress in Fig. 24. The lumped parameter model is designed so that it represents for a real bladed disk with a friction ring damper. As an example, Fig. 25 shows the nodal diameter plot of the lumped parameter model with $N = 20$ sectors under the frictionless condition. There are various regions of modal density which are directly linked to the coupling between the blades and the disk. For instance, coupling between the blades and the disk is weak in the region of high nodal diameters whereas the coupling is stronger in the region of small nodal dimeters. The coupling between the blades and the disk is important for the performance of the friction ring damper. The energy dissipations by the friction force are obtained when there is enough the relative displacement between the disk and the ring.

The equations of motion for the model described above can be written in matrix form as

$$\mathbf{M}\ddot{\mathbf{X}}(t) + \frac{\beta}{\omega}\mathbf{K}\dot{\mathbf{X}}(t) + \mathbf{K}\mathbf{X}(t) + \mathbf{F}_{nl}(t) = \mathbf{F}(t), \tag{50}$$

where $\mathbf{M}$ and $\mathbf{K}$ are the mass and stiffness matrices, β is the structural damping coefficient, $\mathbf{X}(t)$ is the vector of displacements, $\mathbf{F}_{nl}(t)$ is the vector of nonlinear forces, and $\mathbf{F}(t)$ is the vector of external harmonic excitations of frequency ω. The effects of the tangential forces at the contact are captured in $\mathbf{F}_{nl}(t)$, thus the stiffness matrix $\mathbf{K}$ is from the slip state. The displacement vector and harmonic force at sector j can be expressed as

$$\mathbf{X}_j(t) = \Re\{\mathbf{x}(t)e^{-i(j-1)\frac{2\pi EO}{N}}\}, \quad (j = 1, \cdots, N) \tag{51}$$

and

$$\mathbf{F}_j = \Re\{\mathbf{F}_1 e^{[-i(\omega t-(j-1)\frac{2\pi EO}{N})]}\}, \quad (j = 1, \cdots, N) \tag{52}$$

where i is $\sqrt{-1}$, $\mathbf{F}_1$ denotes the complex amplitude vector of the excitation applied in the reference sector,

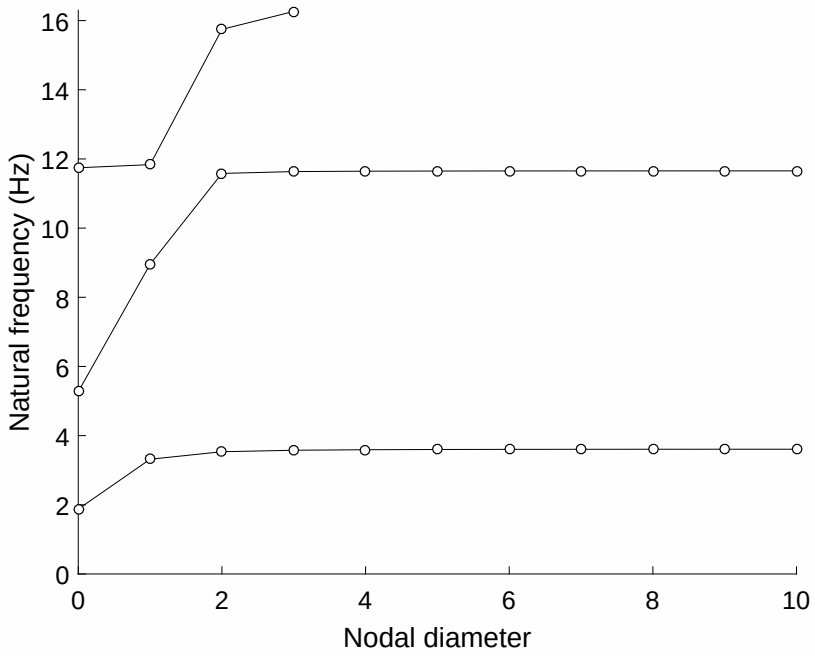

Figure 25: Frequency and nodal diameter plot

$\mathbf{x}$ refers to the complex vector of displacements of the reference sector defined as

$$\mathbf{x}(t) = (\mathbf{u} + i\bar{\mathbf{u}})qe^{i(\omega t - \varphi)}, \tag{53}$$

where vectors $\mathbf{u}$ and $\bar{\mathbf{u}}$ are a pair of real vectors, q is the real value of the amplitude of the response, and φ is the phase lag between the excitation and the response of the system.

At the steady-state, the motion at the j^{th} sector due to the periodic traveling excitation can be described by using Eqs. (51) and (53) as

$$\begin{aligned} \mathbf{X}_j(t) &= \mathbf{\Phi}_j(t)q, \\ &= \left[\mathbf{\Phi}_j^a(t) \quad \mathbf{\Phi}_j^b(t)\right] \left[cos\varphi \quad sin\varphi\right]^T q, \end{aligned} \tag{54}$$

where

$$\begin{aligned} \mathbf{\Phi}_j^a(t) &= \mathbf{u}cos\left(\omega t - (j-1)\frac{2\pi n}{N}\right) + \bar{\mathbf{u}}sin\left(\omega t - (j-1)\frac{2\pi n}{N}\right), \\ \mathbf{\Phi}_j^b(t) &= \mathbf{u}sin\left(\omega t - (j-1)\frac{2\pi n}{N}\right) - \bar{\mathbf{u}}cos\left(\omega t - (j-1)\frac{2\pi n}{N}\right). \end{aligned} \tag{55}$$

Modeshapes $\mathbf{\Phi}_j^a$ and $\mathbf{\Phi}_j^b$ are the fixed to the rotating frame corresponding to the traveling wave excitation, n is the nodal diameter of the dominant mode pair, and q is the modal amplitude. The derivative of $\mathbf{X}_j(t)$ in Eq. (54) with respect to time t gives

$$\dot{\mathbf{X}}_j(t) = -\omega\bar{\mathbf{\Phi}}_j(t)q, \tag{56}$$

where

$$\bar{\mathbf{\Phi}}_j(t) = \left[\mathbf{\Phi}_j^b(t) \quad -\mathbf{\Phi}_j^a(t)\right], \tag{57}$$

since

$$\begin{aligned}\dot{\mathbf{\Phi}}_j^a &= -\omega \mathbf{\Phi}_j^b, \\ \dot{\mathbf{\Phi}}_j^b &= \omega \mathbf{\Phi}_j^a.\end{aligned} \tag{58}$$

4.2.2. Nonlinear friction force

The nonlinear force $\mathbf{F}_{nl}$ in Eq. (50) associated with friction the local elastic restoring forces at the stick phase and dissipative forces at the slide phase. Since the aim of this study is to obtain the steady-state response of the system under a periodic forcing, the dissipative energy at the contact during a period of the motion is calculated by a quasi-static analysis. The motion caused by a traveling wave excitation has a symmetric pattern around the blades. Due to its cyclically periodic but traveling forcing, each sector undergoes the same pattern of response during a cycle of the excitation. Therefore, the friction forces in the system during a revolution can be obtained from a sector level calculation. The friction forces at the sector j, $\mathbf{F}_{f,j}$, resulting from the quasi-static motion and the projection onto the vector of relative displacement at sector j can be expressed as

$$f(t) = \sum_{j=1}^{N} \mathbf{\Phi}_j^{rel^T} \mathbf{F}_{f,j}(\mathbf{X}_j(t)) = N \mathbf{\Phi}^{rel}{}_1^T \mathbf{F}_{f,1}(\mathbf{X}_1(t)), \tag{59}$$

where $\mathbf{\Phi}_j^{rel}$ is the vector of relative displacements in sector j. The relative motion $\mathbf{\Phi}_j^{rel}$ is obtained by subtracting the motion of the nodes of the disk $\mathbf{\Phi}_{j,disk}^a$ and from the motion of the nodes of the ring $\mathbf{\Phi}_{j,ring}^a$ at the contact:

$$\begin{aligned}\mathbf{\Phi}_j^{rel} &= \mathbf{\Phi}_{j,disk}^a - \mathbf{\Phi}_{j,ring}^a, \\ \bar{\mathbf{\Phi}}_j^{rel} &= \mathbf{\Phi}_{j,disk}^b - \mathbf{\Phi}_{j,ring}^b,\end{aligned} \tag{60}$$

where each element in $\mathbf{\Phi}_{j,disk}^a$ and $\mathbf{\Phi}_{j,ring}^a$ are aligned as same contact points. Note that the relative motions are also satisfy the relationship in Eq. (58) as $\dot{\mathbf{\Phi}}_j^{rel} = -\omega \bar{\mathbf{\Phi}}^{rel}$ and $\dot{\bar{\mathbf{\Phi}}}_j^{rel} = \omega \mathbf{\Phi}^{rel}$.

The friction force projected onto the relative displacement at a steady state is obtained by taking the average during a period of the motion. The average friction force $< f >$ is written as

$$< f >= \frac{1}{T} \int_T f(t) d(\omega t) = \frac{1}{2\pi} \int_0^{2\pi} f\left(\frac{\theta}{\omega}\right) d\theta. \tag{61}$$

During the stick phase, the nonlinear force due to the friction is associated with the elastic restoring forces. Thus, the average stored energy due to the friction force is

$$\begin{aligned}E_s &= \frac{1}{T} \int_T N \mathbf{X}_1^{rel^T} \mathbf{F}_{f,1} dt = \frac{\omega}{2\pi} \int_0^{2\pi} \left(\mathbf{\Phi}_1^{rel^T} q\right) \mathbf{F}_{f,1} d\left(\frac{\theta}{\omega}\right) \\ &= \left(\frac{1}{2\pi} \int_0^{2\pi} N \mathbf{\Phi}_1^{rel^T} \mathbf{F}_{f,1} d\theta\right) q =< f > q,\end{aligned} \tag{62}$$

where $N\boldsymbol{\Phi}_1^{rel^T}\mathbf{F}_{f,1} = f$ as shown in Eq. (59). Also, the friction force dissipates the energy at the contact surface in form of the heat during the slip phase. The energy dissipation due to the friction force is obtained as

$$\begin{aligned} E_c &= -\int_T N\dot{\mathbf{X}}_1^{rel^T}\mathbf{F}_{f,1}dt = -\int_T N\left(\dot{\boldsymbol{\Phi}}_1^{rel^T}q\right)\mathbf{F}_{f,1}dt \\ &= -\int_T N(-\omega\bar{\boldsymbol{\Phi}}_1^{rel^T}q)\mathbf{F}_{f,1}dt = 2\pi\left(\frac{1}{2\pi}\int_0^{2\pi} N\bar{\boldsymbol{\Phi}}_1^{rel^T}\mathbf{F}_{f,1}d\theta\right)q \\ &= 2\pi < \bar{f} > q. \end{aligned} \tag{63}$$

4.2.3. Equivalent nonlinear damping coefficient and stiffness

The relationship between the input displacements and the resulting friction forces can be plotted to establish hysteresis loop. The energy dissipated by the friction force is the area inside the loop. The area inside the hysteresis loop is independent of the velocity of the motion, but depends on the amplitude of the displacements. This type of energy dissipation is called hysteretic or structural damping. To account for the energy dissipation due to the friction at the contacts, an equivalent structural damping coefficient γ is defined. Therefore the energy dissipation by the equivalent damping force during a period of motion can be obtained as

$$\begin{aligned} W_c &= \oint_D j\gamma\left(\mathbf{K}\mathbf{X}\right)^T d\mathbf{X} = \frac{\gamma}{\omega}\int_T \dot{\mathbf{X}}^T\mathbf{K}\dot{\mathbf{X}}dt \\ &= \frac{\gamma}{\omega}\int_T (\dot{\boldsymbol{\Phi}}^T q)\mathbf{K}(\dot{\boldsymbol{\Phi}}q)dt = \frac{\gamma}{\omega}\int_T -\omega\boldsymbol{\Phi}^T q\mathbf{K}(-\omega\boldsymbol{\Phi}q)dt \\ &= \gamma\omega q^2\int_T \omega_n^2 dt = 2\pi\gamma\omega_n^2 q^2, \end{aligned} \tag{64}$$

where vectors $\boldsymbol{\Phi}$ and $\bar{\boldsymbol{\Phi}}$ can be defined for the entire system by grouping vectors $\boldsymbol{\Phi}_j$ and $\bar{\boldsymbol{\Phi}}_j$ for all j, and $\boldsymbol{\Phi}^T\mathbf{K}\boldsymbol{\Phi} = \bar{\boldsymbol{\Phi}}^T\mathbf{K}\bar{\boldsymbol{\Phi}} = \omega_n^2$. Also, a equivalent stiffness associated with the elastic restoring forces by the friction is defined to account for the elastic effects which exist locally during the stick phase. The average elastic energy in the contact can be expressed using the equivalent stiffness matrix $\mathbf{K}_f$ as

$$\begin{aligned} W_s &= \frac{1}{T}\int^T \mathbf{X}^{rel^T}\mathbf{K}_f\mathbf{X}^{rel}dt = \frac{1}{T}\int^T q\boldsymbol{\Phi}^{rel^T}\mathbf{K}_f\boldsymbol{\Phi}^{rel}qdt \\ &= \frac{\omega}{2\pi}\int_0^{2\pi} k_f q^2\frac{d\theta}{\omega} = k_f q^2, \end{aligned} \tag{65}$$

where $\mathbf{X}^{rel} = \boldsymbol{\Phi}^{rel}q$ is the relative displacement at the contact surfaces, and $k_f = \boldsymbol{\Phi}^{rel^T}\mathbf{K}_f\boldsymbol{\Phi}^{rel}$.

The dissipated energy at the contact interface in the form of structural damping in Eq. (64) and the energy dissipation by the friction force in Eq. (63) are defined to be the same. Likewise, the average elastic energy in the contact in Eq. (65) and the average energy stored due to the friction force in Eq. (62) are

defined to be the same. Thus, the expression of the equivalent damping factor and the equivalent stiffness at the contact pair can be written as

$$\gamma = \frac{< \bar{f} >}{\omega_n^2 q}, \tag{66}$$

and

$$k_f = \frac{< f >}{q}, \tag{67}$$

repectively.

4.2.4. Reduced order modeling

The transformation matrix is constructed in Eq. (68). The transformation matrix comprises modeshapes from the stick state ($\mathbf{\Phi}^{st}_{j,B},\ \mathbf{\Phi}^{st}_{j,R}$) and additional vectors for capturing the relative motion ($\mathbf{\Phi}^{rel}_{j,R}$),

$$\begin{aligned} \mathbf{T}_j &= \begin{bmatrix} \mathbf{\Phi}^{st}_{j,B} & \mathbf{0} & \bar{\mathbf{\Phi}}^{st}_{j,B} & \mathbf{0} \\ \mathbf{\Phi}^{st}_{j,R} & \mathbf{\Phi}^{rel}_{j,R} & \bar{\mathbf{\Phi}}^{st}_{j,R} & \bar{\mathbf{\Phi}}^{rel}_{j,R} \end{bmatrix} \\ \bar{\mathbf{T}}_j &= \begin{bmatrix} \bar{\mathbf{\Phi}}^{st}_{j,B} & \mathbf{0} & \mathbf{\Phi}^{st}_{j,B} & \mathbf{0} \\ \bar{\mathbf{\Phi}}^{st}_{j,R} & \bar{\mathbf{\Phi}}^{rel}_{j,R} & \mathbf{\Phi}^{st}_{j,R} & \mathbf{\Phi}^{rel}_{j,R} \end{bmatrix}, \end{aligned} \tag{68}$$

where B refers to DOFs of the blade together with the disk and R refers to DOFs of the ring. At the full-stuck state, the magnitude of the relative coordinate $\mathbf{q}^{rel}$ approaches 0. For the frictionless condition, on the otherhand, the magnitude of the relative motion $\mathbf{q}^{rel}$ has a magnitude similar to the magnitude of $\mathbf{q}^{st}$.

By plugging the transformation matrix $\mathbf{T}_j$ into Eq. (50), the equation of motion can be written as

$$\left[-\omega^2\mathbf{m} + (i\beta + 1)\mathbf{k}\right]\mathbf{q} + \mathbf{f}_{nl} = \mathbf{f}_{ex}, \tag{69}$$

where

$$\mathbf{m} = \sum_{j=1}^{N} \mathbf{T}_j^T \mathbf{M}_j \mathbf{T}_j, \tag{70}$$

and

$$\mathbf{k} = \sum_{j=1}^{N} \mathbf{T}_j^T \mathbf{K}_j \mathbf{T}_j. \tag{71}$$

Note that reduced stiffness matrix where the contact surfaces are in full slip. The mass and stiffness matrices in Eq. (50) are block matrices comprised of matrices $\mathbf{M}_j$, with $j = 1, \cdots, N$. Each matrix $\mathbf{M}_j$ is the free-interface mass matrix for the j^{th} sector. However, the stiffness matrix $\mathbf{k}$ can be expressed as

$$\mathbf{k} = \mathbf{k}^{st} - \mathbf{k}^{o}_{f}, \tag{72}$$

where $\mathbf{k}^{st}$ is reduced stiffness matrix with contact surface are in full stick. Note that $\mathbf{k}^{o}_{f}$ is a reduced stiffness matrix which accounts for the tangential stiffness at the contact pairs, $\mathbf{k}^{o}_{f}$ is obtained in the calculation of the equivalent stiffness when the relative motion between the contact are nearly zero ($\mathbf{q} \approx \mathbf{0}$).

Since the nonlinear force $\mathbf{f}_{nl}$ is characterized as equivalent damping and stiffness matrices. Thus, the nonlinear force vector can be written as,

$$\mathbf{f}_{nl} \cong (i\mathbf{\Gamma} \circ \mathbf{k}_f + \mathbf{k}_f)\mathbf{q}, \tag{73}$$

where $\circ$ is the Hadamard product, $\mathbf{\Gamma}$ is the equivalent damping matrix, and $\mathbf{k}_f$ is the equivalent stiffness matrix, respectively. The elements of the equivalent damping matrix $\mathbf{\Gamma}$ and the equivalent stiffness matrix $\mathbf{k}_f$ are defined differently depending on the motion and corresponding projection. Their elements are defined as

$$\begin{aligned} \gamma_{(\zeta,\xi)} &= \frac{N}{q}\left[\frac{1}{2\pi}\int_0^{2\pi} \mathbf{T}_{j,\zeta}^T \mathbf{F}_f\left(\bar{\mathbf{T}}_{j,\xi} q\right)\frac{d\theta}{\omega}\right], \\ k_{f(\zeta,\xi)} &= \frac{N}{q}\left[\frac{1}{2\pi}\int_0^{2\pi} \mathbf{T}_{j,\zeta}^T \mathbf{F}_f\left(\mathbf{T}_{j,\xi} q\right)\frac{d\theta}{\omega}\right], \\ &\qquad (\zeta,\ \xi = 1, \cdots, m), \end{aligned} \tag{74}$$

where $\gamma_{(\zeta,\xi)}$ and $k_{f(\zeta,\xi)}$ are the elementss of the equivalent damping and the equivalent stiffness matrices, respectively. ζ and ξ represent the indices of the columns of $\mathbf{T}_j$ and $\bar{\mathbf{T}}_j$. Plugging Eqs. (72) and (73) into Eq. (69), the equation of motion the bladed disk and ring system can be written as

$$[-\omega^2\mathbf{m} + (i\beta + 1)(\mathbf{k}^{st} - \mathbf{k}_f^o) + i\mathbf{\Gamma} \circ \mathbf{k}_f + \mathbf{k}_f]\mathbf{q} = \mathbf{f}_{ex}. \tag{75}$$

4.2.5. Solution method

Sinc the ROM cannot be solved explicitly, an iterative solution method is performed. First, Eq. (75) is re-written as

$$\mathbf{\Theta}^{-1}\mathbf{q} = \mathbf{f}_{ex}, \tag{76}$$

where

$$\mathbf{\Theta} = \left[-\omega^2\mathbf{m} + (i\beta + 1)(\mathbf{k} - \mathbf{k}_f^o) + i\mathbf{\Gamma}(\mathbf{q}) \circ \mathbf{k}_f + \mathbf{k}_f(\mathbf{q})\right]^{-1}. \tag{77}$$

The following simple iteration scheme can be used at a particular frequency ω

$$\mathbf{q}_{i+1} = \mathbf{\Theta}_i \mathbf{f}_{ex}, \tag{78}$$

where $\mathbf{q}_{i+1}$ denotes the solution for the modal amplitude vector at the $(i+1)^{\text{th}}$ iteration step, and $\mathbf{\Theta}_i$ is obtained using $\mathbf{q}_i$ from the i^{th} iteration. Iterations terminates when the percentage error fall into a small enough value ε

$$e = ||\frac{\mathbf{q}_{i+1} - \mathbf{q}_i||}{||\mathbf{q}_i}|| < \varepsilon \tag{79}$$

The equivalent damping and stiffness matrices in Eq. 73 can be obtained before the ROM equations are solved.

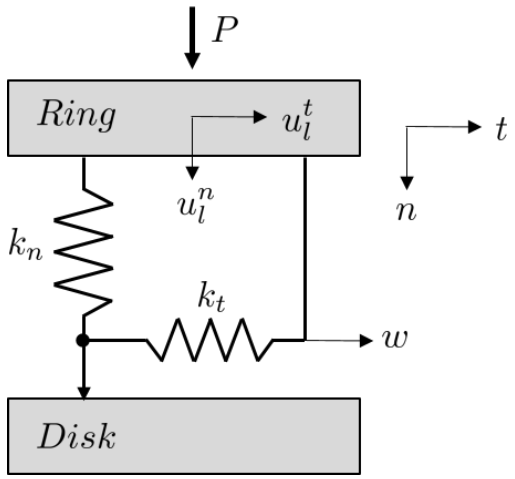

Figure 26: Schematic view of contact modeling between the ring and the disk

4.3. Contact stiffness identification

The response vector for a bladed disk system with a dry friction damper described in Eq. (50) can be written as,

$$\mathbf{X}(t) = \left(-\omega^2\mathbf{M} + \beta\mathbf{K} + \mathbf{K}\right)^{-1}\left(\mathbf{F}(t) - \mathbf{F}_{nl}(t)\right) \tag{80}$$

where $\mathbf{M}$, $\mathbf{K}$, $\mathbf{F}(t)$, $\mathbf{F}_{nl}(t)$, and $\mathbf{X}(t)$ are the mass matrix, stiffness matrix, traveling wave excitation force vector, nonlinear force vector associated with friction and displacement vector respectively. $\mathbf{F}_{nl}(t)$ is is determined by Coulomb's law. A blade and a ring damper in contact are shown in Fig. 26. The contact stiffnesses at the contact pair l in the local coordinate system (n, t) are represented by a spring. The relative motion in normal direction n causes normal load variation $\bar{P}$ and possible separation, according to the following equation,

$$\bar{P} = \begin{cases} P + k_n u_l^n & \text{if } u_l^n \geq -P/k_n \\ 0 & \text{if } u_l^n < -P/k_n \end{cases}, \tag{81}$$

and the resulting friction force is related to the tangential relative motion u_l^t according to the following equation,

$$F_{nl}(X_l) = \begin{cases} k_t(u_l^t - w) & \text{if } k_t|u_l^t - w| \leq \mu\bar{P} \\ -\mu n \text{sign}(\dot{w}) & \text{if } k_t|u_l^t - w| \geq \mu\bar{P} \end{cases}. \tag{82}$$

Therefore, the dynamic response $\mathbf{X}(t)$ of the given bladed disk with system matrices $\mathbf{M}$ and $\mathbf{K}$ can be determined by the parameters k_n, k_t, μ, P, ω, and amplitude of the excitation force vector $\mathbf{F}(t)$:

$$\mathbf{X}(t) = \mathbf{X}(t)(\omega, k_n, k_t, F_{amp,k}, \mu, P), \tag{83}$$

where $F_{amp,k}$ is the amplitude of the excitation force vector $\mathbf{F}(t)$.

Under the known friction coefficient μ and the normal load P, the residuals between the normalized forced responses of measurements and the normalized forced responses predictions by the ROM can be defined as

$$R_i(\omega, k_n, k_t, F_{amp,k}) = \frac{\bar{X}_i(\omega, F_{amp,k}) - X_i(\omega, k_n, k_t, F_{amp,k})}{F_{amp,k}}, \tag{84}$$

where $\bar{X}_i$ is the measured forced response at i^{th} excitation frequency and X_i is the forced response predictions from the ROM. The root mean square of the residuals over the forcing frequencies is written as

$$R(k_n, k_t, F_{amp,k}) = \sqrt{\frac{1}{N}\sum_{i=1}^{N}\{R_i(\omega, k_n, k_t, F_{amp,k})\}^2}, \tag{85}$$

where N is the number of excitation frequencies. Friction in the contact exhibit two different effects of the bladed disk system. The relative motion at the friction contact dissipates energy, adding damping to the system. Moreover, friction dampers stiffen a structure compared to a structure with free interfaces which can significantly affect resonance frequencies of a bladed disk. The stiffness properties of damper contact pair are dependent on the relative motion of contact pairs. Therefore, different amplitudes of forcing amplitudes can lead to different regimes of system response which can help in identification of the contact parameters. To exploit this fact residuals in Eq. (85) with multiple cases of forcing amplitude is required. Thus a representative residual can be defined by the root mean square of the residuals obtained from different forcing amplitudes as follows:

$$R_F(k_n, k_t) = \sqrt{\frac{1}{p}\sum_{k=1}^{p}\{R(k_n, k_t, F_{amp,k})\}^2} \tag{86}$$

where p is the number of forcing amplitudes.

To identify the contact stiffnesses we must find the values of k_n and k_t which minimizes this representative residual.

$$k_n, k_t \in arg \min_{k_n, k_t} R_F(k_n, k_t) \tag{87}$$

4.4. Results and discussion

o validate the developed ROM, force response results from the ROM are compared with results obtained by a time domain analysis. The lumped parameter model in Fig. 24 with $N = 20$ is excited at the blade tip node with the forcing amplitude 5 with an engine order 1 excitation pattern. Steady-state responses under the traveling wave excitation are calculated. The equivalent damping coefficient and stiffness associated with the friction force is calculated quasi-statically by describing the motion corresponding to a traveling wave excitation of engine order 1. The resultant equivalent stiffness and the equivalent damping coefficients are plotted in Figs. 27 and 28 with various friction coefficients.

The responses of the model during full stick and full slip conditions is linear and can be obtained by using linear calculation methods such as harmonic response analysis. Figure 29 shows the predicted responses under full slip, full stick and $\mu = 0.2$ contact conditions. The predicted response for the linear cases match

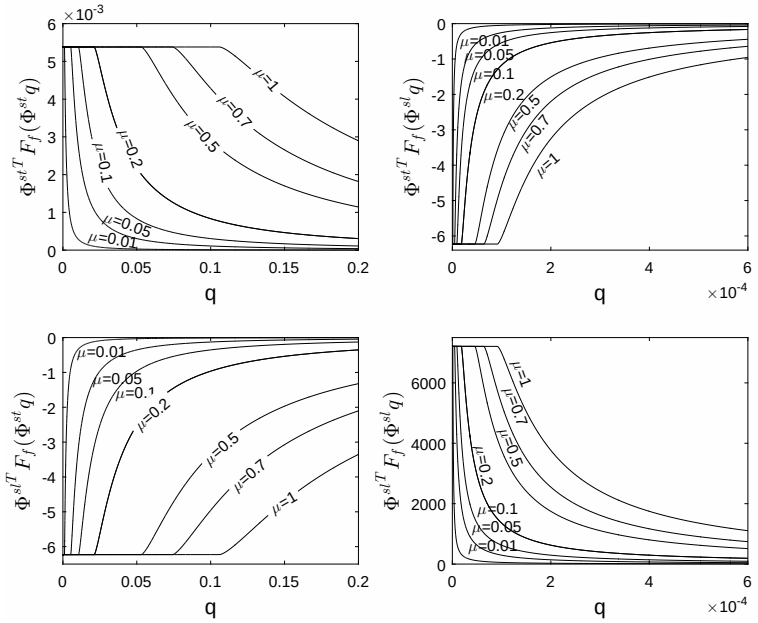

Figure 27: Equivalent stiffness and at various friction coefficients $\mu = 0.01 \sim 1$

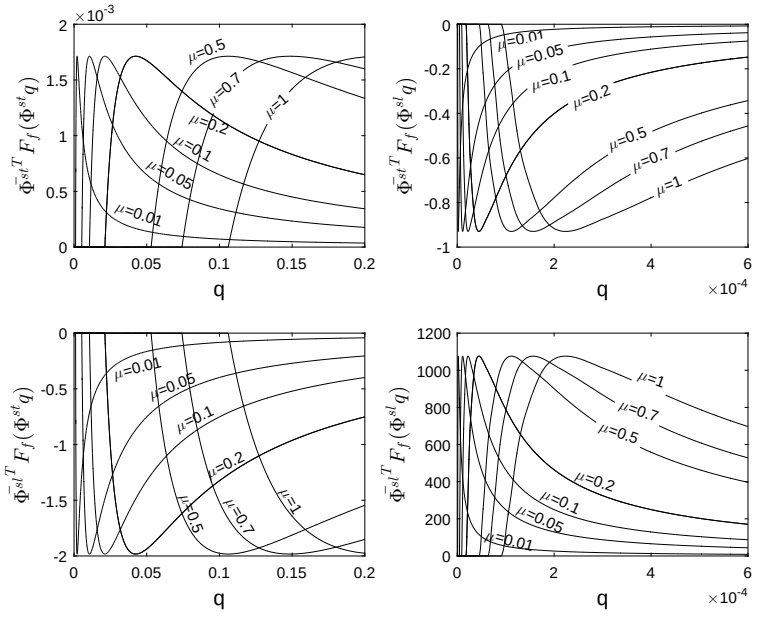

Figure 28: Equivalent damping at various friction coefficients $\mu = 0.01 \sim 1$

well with results from a harmonic analysis. In the case of the nonlinear system, where stick-slip phase changes are involved, time domain analysis by using Newmark method is performed. To compute the response at a particular frequency, the bladed disk and ring system is excited at the first resonance with engine order excitation 1. The relative error between the amplitudes predicted by the TDA and the ROM is below 0.03% for the nonlinear case.

To identify the contact stiffness, measurements at 8 different excitation frequencies across the half-power bandwidth are chosen. As shown in Fig. 30, 8 discrete excitation frequencies are selected across the half-

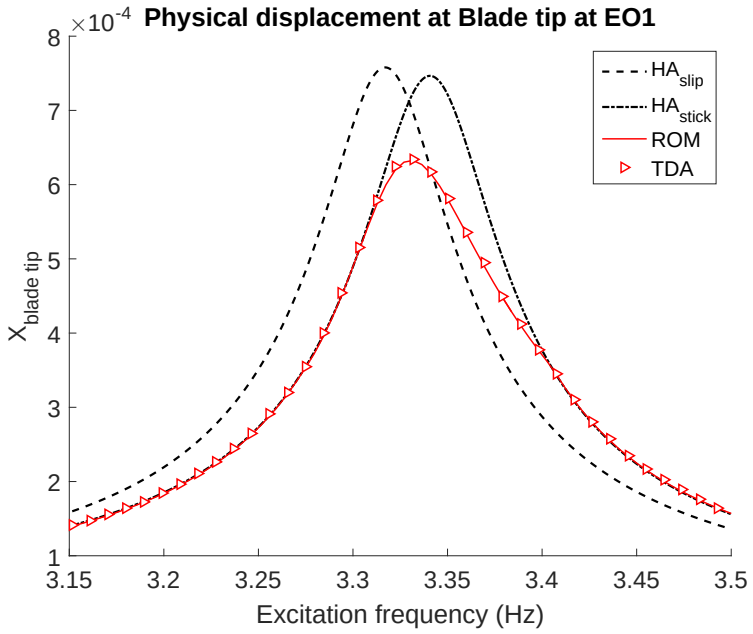

Figure 29: Physical displacement at the blade tip ($\mu = 0.2$)

power bandwidth. For maximum efficiency, a non-uniform frequency step size is used. Smaller frequency spacing is used in regions near resonant frequencies, and larger frequency step sizes are used in regions away from resonant frequencies. Measurements with 1% random measurement noise are performed 20 times at

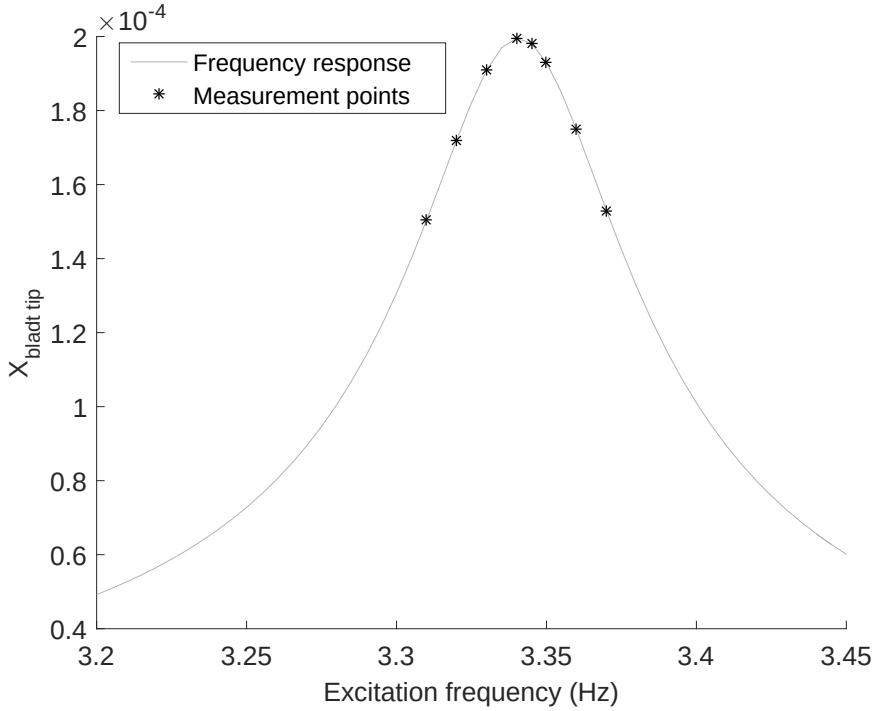

Figure 30: Measurement points within the half-power bandwidth

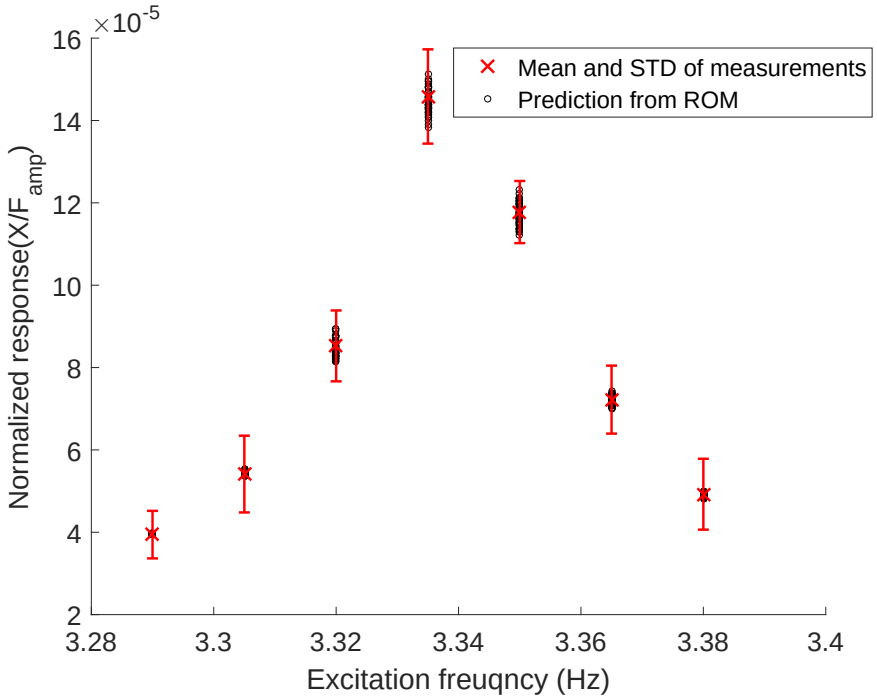

Figure 31: Mean and STD of measurements, and predictions of ROM

each excitation frequency. The measured forced response, the standard deviation (STD) and the mean values are plotted in Fig. 31.

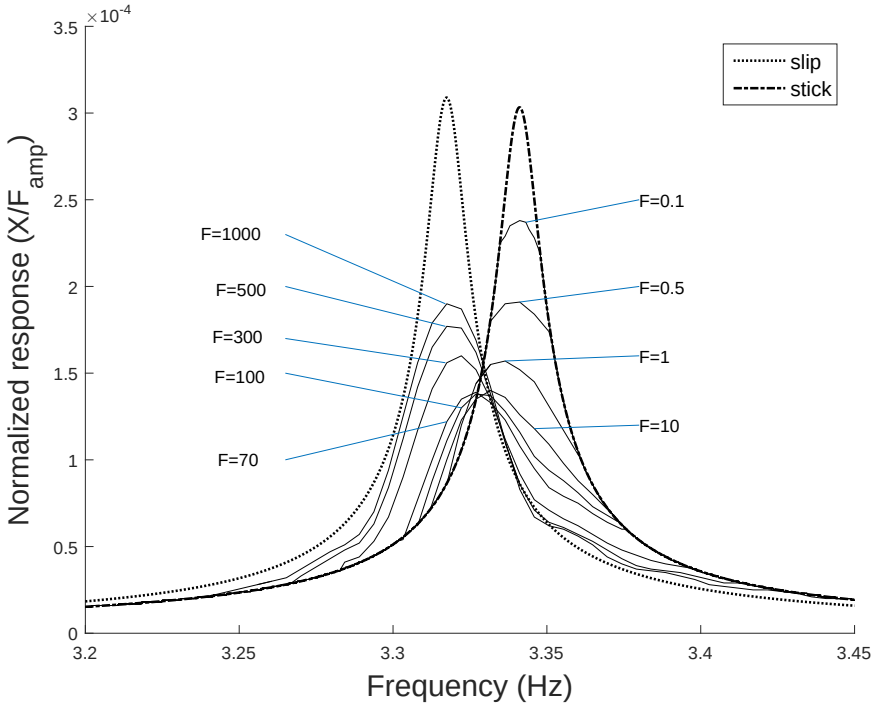

Figure 32: Normalized forced response under different excitation levels

Normalized forced response levels obtained from different excitation levels are shown in Fig. 32. The normalization is carried out by dividing the forced response by the excitation level. This allows comparison of nonlinear effects of dampers on forced response at different forcing magnitudes. In the forced responses of the system with very small forcing excitation we observe only a few contact pairs contributing to the slip phase. Although the energy dissipation is localized in small regions of contact points, the contribution of the damping to the system is significant. For example, the forced response with the forcing amplitude $F = 0.1N$ shows reduction of the peak amplitude by 23%, while the change of the natural frequency is 0.71%. The regimes of the forced responses with small excitation level provide important information for the identification of the normal stiffness k_n. On the other hand, for higher forcing amplitude (eg. $10N \sim 70N$ amplitudes which exhibit lower normalized force responses, the effect of the damping due to the friction force tends to remain the same. Also, the shift in natural frequencies is relatively large compared to in that of the small forcing amplitude cases. In this region, the tangential stiffness k_t can be identified efficiently.

If the forcing amplitude is too large, the most of contact points may move to slip phase during some time in their response period, so that the system converges to the gross slip when all the points are in slip at all times during the period. When all the contack points are in gloss slip, the recognition of the tangential stiffness from the forced response is not feasible. The residuals between the forced responses from the experiments and the estimation by the ROM are calculated (Eq. (86)). The residuals obtained from the different range of the excitation levels are plotted in Figs. 33 and 34. The contact stiffness ranges are obtained based on the forced response predictions in between the two linear cases (stick and slide), and upto 1% of measurement error is introduced. The sum of the residuals from the forcing amplitude of $0.1N$ to $10N$ exhibits a distinctive local minimum at $k_n = 4.5 \times 10^8 N/m$ and $k_t = 5.5 \times 10^8 N/m$. However, the local minimal value of the residuals from all the forcing amplitudes is not distinguishable. It is spread in a range of the tangential stiffness. In Fig. 36, the residuals near the local minimum are examined with a finer resolution of the contact stiffness.

At the given range of the contact stiffness, the residual surface is convex. A gradient based method is used to find the minima of the residual surface. A line search algorithm may also be employes along each of the axes, k_n and k_t. For example, at a fixed tangential stiffness k_t, the minimum residual can be found as follows,

$$\begin{cases} \text{1. For } k = 0 & : \text{Select } k_{n,0},\ \varepsilon \\ \text{2. For } k > 0 & : \text{Compute } \alpha_k = \arg \min_{\alpha} R(k_{n,k} - \alpha g_k) \\ & \quad \text{Set } k_{n,k+1} = k_{n,k} - \alpha_k g_k \\ \text{3. For } k = k+1 & : \text{Stop, if } ||g_{k+1}|| < \varepsilon \end{cases}, \tag{88}$$

where g_k is the gradient at step k ($g_k = \delta R(k_{n,k}, k_t)/\delta k_{n,k}$), and α_k is adjustable step size at step k. Searching along the line determined by g_k, the gradient of residuals with a fixed k_t, the iteration terminates at the point that gives the smallest value of the residual.

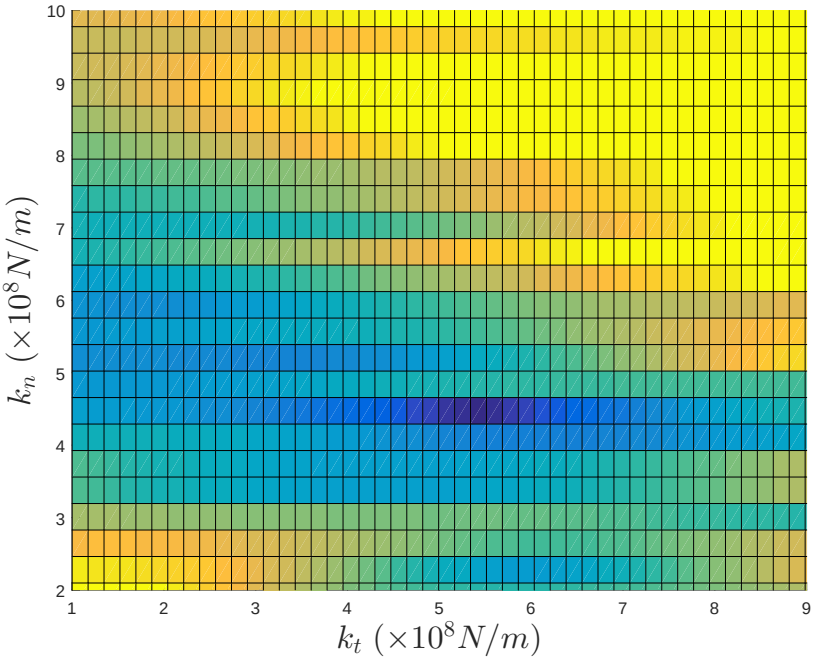

Figure 33: RMS of residuals of forcing amplitudes from $F = 0.1N$ to $F = 10N$

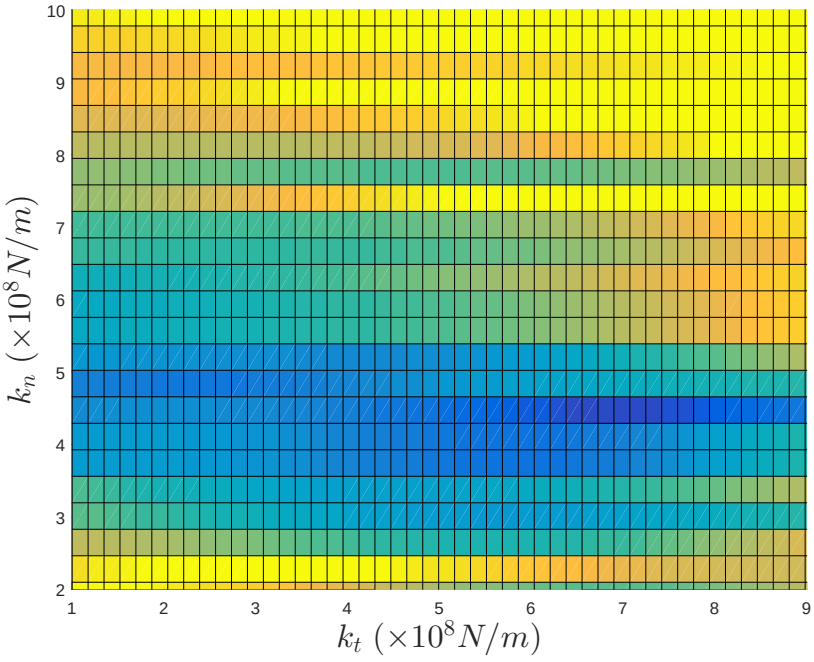

Figure 34: RMS of residuals of forcing amplitudes from $F = 0.1N$ to $F = 1000N$

The friction coefficient is identified by the comparison of the minimal residuals obtained from various friction coefficients. First, the optimization problem with the variables of contact stiffnesses is solved by the gradient method. And the procedure is repeated by changing the friction coefficient until the residual reaches the minimum. The gradient method is also applied at this step. The friction coefficients and corresponding residuals are shown in Fig. 37. For the ideal case, absence of the measurement noise, the R_F is found to be

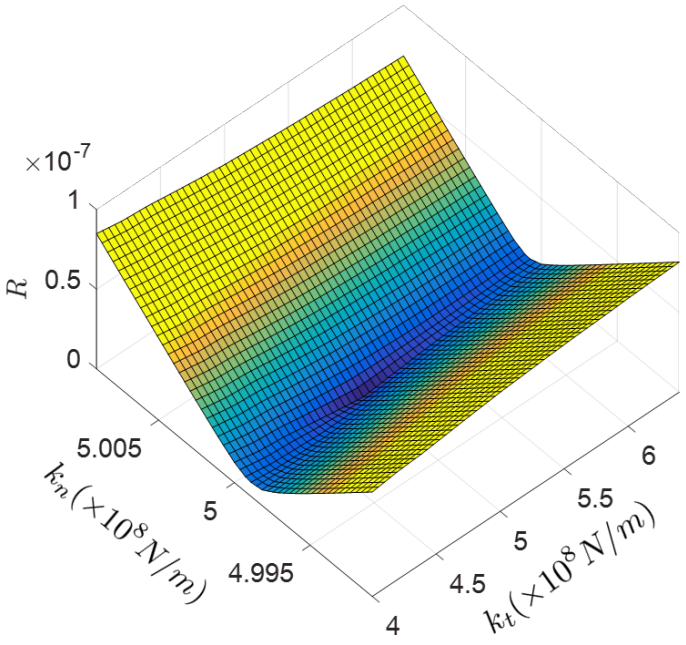

Figure 35: Residual contour plot

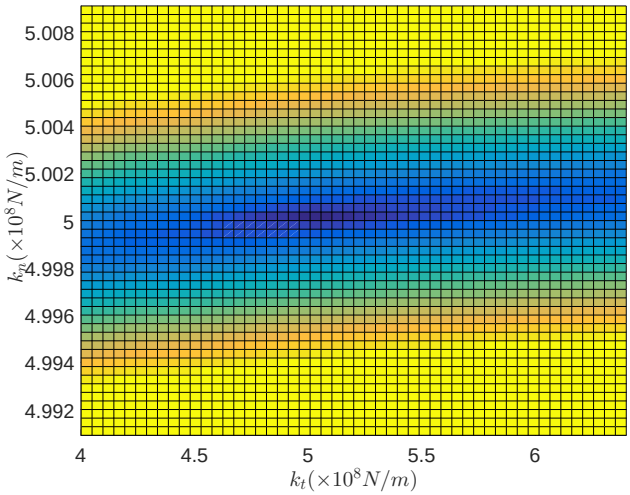

Figure 36: Residual contour plot (top view)

0 at $\mu = 0.2$. With measurement error of 1%, the residual rises to 0.006; however, it still gives the minimum at the $\mu = 0.2$. The forced response prediction based on the identified parameters of the contact stiffnesses and the friction coefficient is plotted in Fig. 38.

4.5. Conclusions

Based on the ROM for a bladed disk with a ring damper, a method for the identification of the dynamic characteristics of nonlinear contact parameters has been developed. Contact parameters include the normal

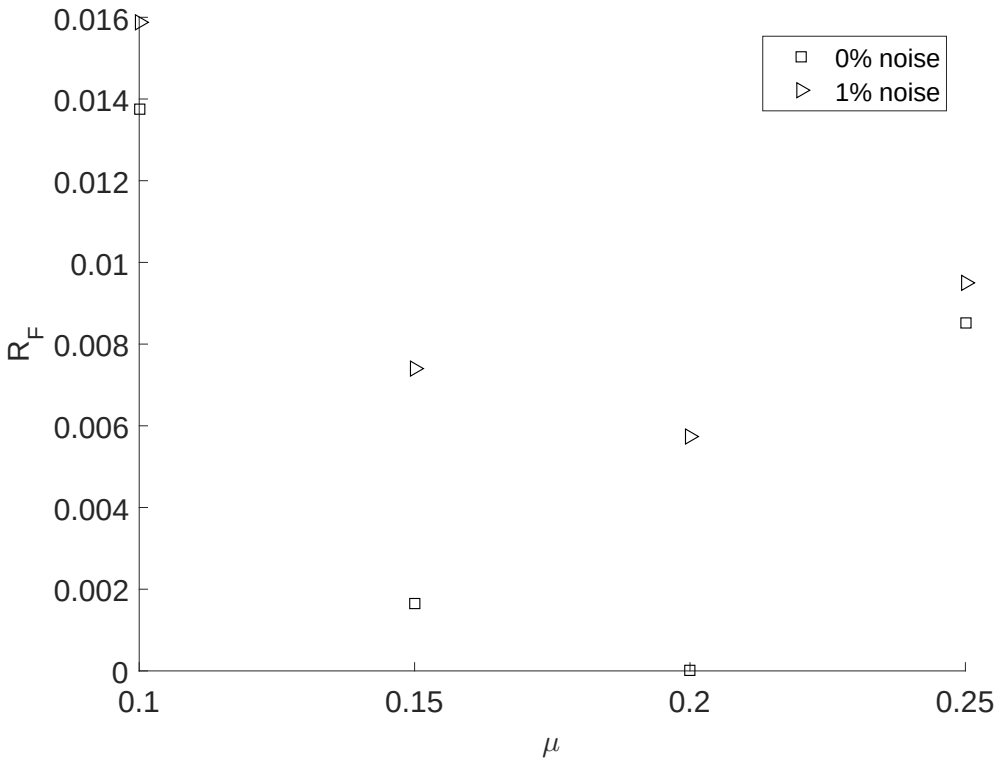

Figure 37: The least residuals along the friction coefficients. The lower boundary of the residuals obtained from 0% (□) measurement noise and residual distribution for 20 different measurement noise patterns at each 1% (▷) random relative measurement noise

stiffness, tangential contact stiffness and contact friction coefficient. The analysis of nonlinear forced response for bladed disks with friction damping is performed by employing the lumped parameter model. The lumped parameter model comprises blade tip, blade root, disk and ring elements. Nonlinear contact force associated with friction is expressed by the nonlinear equivalent damping coefficient and stiffness. The response dependent equivalent damping and stiffness are pre-calculated by quasi-static analysis, and are substituted for the nonlinear friction forces in the iterative solution. The developed ROM is verified by comparing the steady-state responses from time domain analysis and the ROM. Surrogate measurement points are obtained by selecting the forced responses near the peak response. By injecting a 1% error for each measurement, the uncertainty of the measurement is included. The residual between the surrogate measurement point and the estimation by the ROM is obtained. The problem for finding the minimum residual with respect to contact parameters is solved by using a gradient method. The procedure to obtain the residuals is repeated by changing the forcing amplitude level. The root mean square of the residuals from multiple forcing amplitude improves the accuracy of the contact stiffness identification.

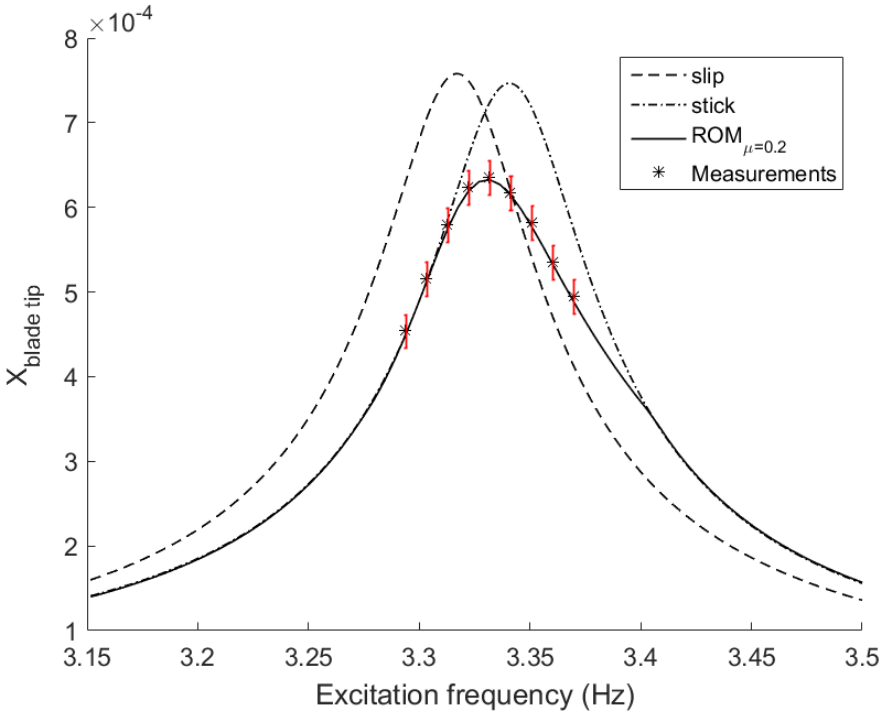

Figure 38: Forced response of the system at full-slip, full-stick, the predictions by the ROM and the measurement points with 1% of measurement errors. The predicted forced response by the ROM is based on the identified values: $k_n = 5 \times 10^8 N/m$, $k_t = 5 \times 10^8 N/m$ and $\mu = 0.2$

CHAPTER 5

5. Damping Mistuning Effects On The Amplification Factor and Statistical Investigation of Vane Packet

5.1. Introduction

Turbine engine compressors consist of rotating and stationary components. The rotating components, which are called bladed disks or rotors, accelerate the mixture of gas and air. The stationary airfoils, also known as stators or vanes, convert the increased rotational kinetic energy into static pressure, redirecting the flow paths of the fluid. The excitation forces induced from the interactions between the fluid and the mechanical components act on the airfoils of the rotors and vanes. Rotors are designed to be cyclically symmetric, where all sectors carry identical structural property. In practice, however, structural properties variations exist among individual sectors due to a variety of reasons: manufacturing tolerances, operational wear, and so forth. The blade-to-blade deviations, referred to as mistuning, affect the free vibrations and forced responses of bladed disk assemblies. It is known that while mistuning has a beneficial effect on flutter [84], mistuned systems may experience an undesirable effect from mistuning on the forced responses, resulting in significant increase in the maximum response amplitudes experienced by a few blades [4]. Thus, accurate predictions of mistuned forced reponses and the effect of mistuning on forced response levels have been a major concern in the design of blade assemblies. The dynamic responses of mistuned bladed disk systems have been studied using experimental, analytical and numerical approaches over the past few decades. Numerous studies to predict the increase in the maximum response amplitude of the blades have been carried out through analyzing deterministic mistuning configurations [5, 85, 21]. In practice, however, blade disks are assembled from a large population of blades and disks, which results in random mistuning, and introduces random variations in maximum amplitude. To account for the effect of random mistuning in the design of bladed disk systems (blisks), statistical analyses of the forced response must be performed by considering deviations of structural properties of individual blades random variables. Many study have used statistical approaches that consider rotor structural parameters to be the actual statistical variables [17, 18, 19, 20]. Monte Carlo simulations are one of the most popular methods to statistically analyze the forced responses of the mistuned blisks due to the accuracy of its results and the simplicity of its algorithm [18, 21, 22]. However, in the case of numerical models of large numbers of degrees of freedoms (DOFs), only limited results can be generated owing to the high computational costs. Therefore, alternative approaches have been considered to obtain the statistical characteristics of the forced responses.

Reduced-order models have been developed to predict the mistuned forced responses in a computationally efficient manner [13, 23, 14].These ROMs are sufficiently compact so that Monte Carlo simulations can be performed to collect the statistics of the forced responses from a large number of mistuned rotors. In these studies [24, 25], however, mistuning patterns are assigned only to the stiffness or blade-alone natural frequency. Since it is difficult to model damping with all damping mechanisms involved, there have been many attempts to develop ROMs approaches accounting for the different damping mechanisms separately. Lumped parameter models were used for constructing ROMs with structural damping [26, 2, 27]. AAlso, the original size of a finite element (FE) model was reduced by characterizing the modal damping mistuning at a sector level or desired nodal locations [23, 28]. Recently, Joshi [29] introduced a novel ROM to capture blade-to-blade damping variations among the blades of integrally bladed rotors.

This paper presents a novel methodology to investigate the influence of blade-to-blade variability in damping. In particular, the change of the maximum forced response amplitudes between the tuned and mistuned systems are examined. To statistically assess the influence of mistuning, an amplification factor (AF) is defined as the ratio of the maximum forced response amplitude of a mistuned system to that of a tuned system through out the frequency range of interest. The amplification factor indicates the impact of random mistuning in bladed disks in a quantitative manner. The paper begins with a brief presentation of the vane packet model used in the analysis and the study of a simple methodology for predicting the most responded mode to the traveling wave excitations. In section 3, the ROMs developed by Joshi [29] are modified and extended to the vane packet model. Based on the developed ROMs, a novel methodology which can predict amplification factors by solving a simple algebraic equation is presented and validated. Finally, the effect of damping variability amongst blades are investigated through a Monte Carlo simulation with a large number of samples of mistuned systems involved.

5.2. Most responded mode to traveling wave excitation

Cyclically symmetric bladed disk exhibits well-defined types of vibration modes. These modes are characterized by the number of equally spaced diametric nodal lines. Those lines are referred to as nodal diameters n. Also, modes of bladed disks are characterized by the number of circumferential nodal lines, referred to as nodal circles. The excitations due to aerodynamic forces travel relatively between the blades with constant speed while preserving their spatial distribution. This type of excitations is referred to as the traveling wave excitation. In terms of forced responses, the blades are subject to engine order (EO) excitation where each blade passes through evenly spaced forcing peaks per revolution. If the forcing field from the traveling wave excitation and a bladed disk mode coincides both in the frequency and the shape, a particular mode will be excited. Thus, a mode shape of nodal diameter n can only be excited by the following engine orders

$$EO = aN \pm n \tag{89}$$

where N is the number of blade and a is an integer constant. However, this approach is not applicable to vane packets since they are not cyclically symmetric structures. Therefore, it is necessary to develop a modeling

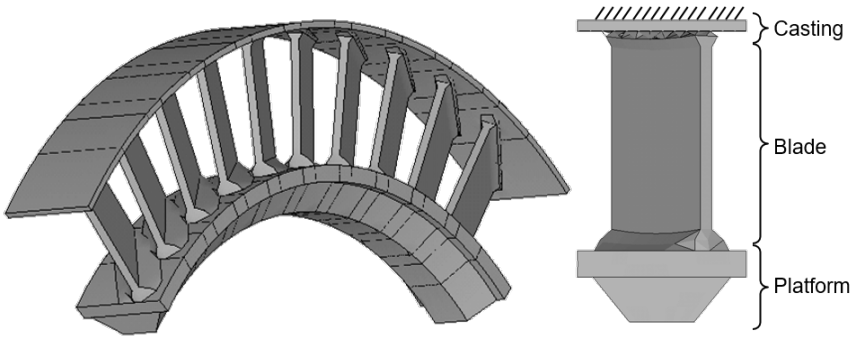

Figure 39: Vane packet FE model

technique to predict the mode of a vane packet that is most responsive to a traveling wave excitation of a specific engine order. In this section, a mode based approach is introduced for predicting which modes are most responsive to such a traveling wave excitation.

5.2.1. Vane Modeling

A three dimensional FE model of a typical vane packet is demonstrated in Fig. 39. The vane packet comprises the casting, the blades and the platform. Each vane packet has 10 blades ($N_s = 10$), and 10 vane packets ($N_p = 10$) form a full-sized vane system. The FE model has 35,116 nodes which is adequately refined for a standard modal analysis. The model has a fixed-free boundary condition where only the casting is clamped. Only one vane packet is considered in this analysis. The first fifty system natural frequencies normalized by the first natural frequency are plotted in Fig. 40.

5.2.2. Mode based prediction

Cyclically symmetric structures have a noteworthy feature that each system mode consists of identical motions in each sector, with a sector-to-sector phase difference. The phase difference between the sectors is called the inter blade phase angle (IBPA) which is a multiple of $2\pi/N$. Thus, the normal modes of the j^{th} sector of a cyclically periodic structure can be expressed as a linear combination of two vectors $\mathbf{u}_{(n)}$ and $\bar{\mathbf{u}}_{(n)}$

$$\begin{aligned} \mathbf{\Phi}^c_{j(n)} &= \mathbf{u}_{(n)} cos\left(2\pi n(j-1)/N\right) - \bar{\mathbf{u}}_{(n)} sin\left(2\pi n(j-1)/N\right) \\ \bar{\mathbf{\Phi}}^c_{j(n)} &= \mathbf{u}_{(n)} sin\left(2\pi n(j-1)/N\right) + \bar{\mathbf{u}}_{(n)} cos\left(2\pi n(j-1)/N\right) \\ &\qquad\qquad (j = 1, \cdots, N), \end{aligned} \tag{90}$$

where $\mathbf{\Phi}^c_{j(n)}$ and $\bar{\mathbf{\Phi}}^c_{j(n)}$ are a pair of modes of a cyclically symmetric structure. Note that n denotes the nodal diameter, and N is the number of sectors. It is assumed that if the m^{th} mode of the vane packet $\mathbf{\Phi}_m$ shows the maximum response level under a traveling wave excitation of an engine order EO, this mode tends to exhibit a periodic shape coinciding with the excitation of such a specific engine order. Under this assumption, the m^{th} mode of each sector can be approximated as a harmonic expansion of two vectors $\mathbf{u}_{(EO)}$

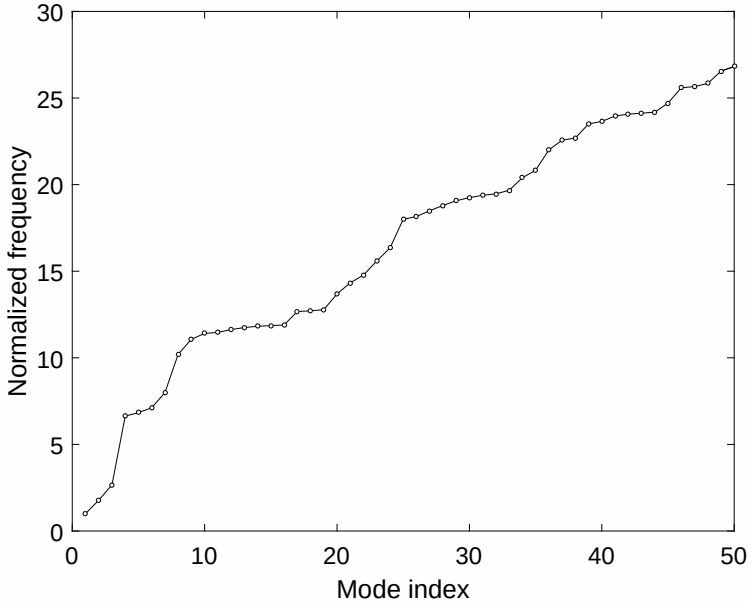

Figure 40: Vane packet model natural frequency

and $\bar{\mathbf{u}}_{(EO)}$ with IBPA $\frac{2\pi EO}{N_s N_p}$, expressed as

$$\mathbf{\Phi}_m = \begin{bmatrix} \mathbf{\Phi}_{m,1} \\ \mathbf{\Phi}_{m,2} \\ \vdots \\ \mathbf{\Phi}_{m,N_s} \end{bmatrix} \approx \underbrace{\begin{bmatrix} cos(0) \times \mathbf{I} & sin(0) \times \mathbf{I} \\ cos(\frac{2\pi EO}{N_s N_p}) \times \mathbf{I} & sin(\frac{2\pi EO}{N_s N_p}) \times \mathbf{I} \\ \vdots & \vdots \\ cos(\frac{2\pi EO}{N_s N_p}(N_s - 1)) \times \mathbf{I} & sin(\frac{2\pi EO}{N_s N_p}(N_s - 1)) \times \mathbf{I} \end{bmatrix}}_{\mathbf{Q}} \begin{bmatrix} \mathbf{u}_{(EO)} \\ \bar{\mathbf{u}}_{(EO)} \end{bmatrix}, \tag{91}$$

where $\mathbf{\Phi}_{m,1}, \cdots,$ and $\mathbf{\Phi}_{m,N_s}$ contain the mode shape of each sector which possess duplicated nodal information at the interface DOFs, N_s is the number of sectors in a vane packet, N_p is the number of vane packet required to form a full-wheel system, $\mathbf{I}$ is the identity matrix, and $\mathbf{u}_{(EO)}$ and $\bar{\mathbf{u}}_{(EO)}$ are functions of engine order excitations. Note that the total number of the blades in the entire vane packet system is $N_s \times N_p$. Eq. (91) represents the alignment of the mode to cyclic symmetry. The vector $\mathbf{u}_{(EO)}$ and $\bar{\mathbf{u}}_{(EO)}$ can be obtained by solving Eq. (91) as a least square problem. However, solving the least square problem becomes computationally expensive due to the large size of the matrix $\mathbf{Q}$ ($(N_s \times$ DOFs in a sector$) \times 2$). Meanwhile, Eq. (91) can be written in the form of a Kronecker product as

$$\mathbf{\Phi}_m = (\mathbf{H} \otimes \mathbf{I}) \begin{bmatrix} \mathbf{u}_{(EO)} \\ \bar{\mathbf{u}}_{(EO)} \end{bmatrix}, \tag{92}$$

where

$$\mathbf{H} = \begin{bmatrix} cos(0) & sin(0) \\ cos(\frac{2\pi EO}{N_s N_p}) & sin(\frac{2\pi EO}{N_s N_p}) \\ \vdots & \vdots \\ cos(\frac{2\pi EO}{N_s N_p}(N_s - 1)) & sin(\frac{2\pi EO}{N_s N_p}(N_s - 1)) \end{bmatrix}. \tag{93}$$

Thus, the least square problem becomes finding the pseudo inverse of $\mathbf{H}$. The matrix $\mathbf{H}$ consists of two vectors where entries are harmonic functions. Since the size of the matrix $\mathbf{H}$ is only $N_s \times 2$, its inverse can be easily computed as

$$\begin{bmatrix} \mathbf{u}_{(EO)} \\ \bar{\mathbf{u}}_{(EO)} \end{bmatrix} = (\mathbf{H} \otimes \mathbf{I})^{-1} \mathbf{\Phi}_m = \left(\mathbf{H}^{-1} \otimes \mathbf{I}^{-1}\right) \mathbf{\Phi}_m = \left(\mathbf{H}^{-1} \otimes \mathbf{I}\right) \mathbf{\Phi}_m. \tag{94}$$

One can determine whether the vane normal modes $\mathbf{\Phi}_m$ are nearly cyclic symmetric by checking the residual between the vane mode and harmonic expansions with the obtained vectors $\mathbf{u}_{(EO)}$ and $\bar{\mathbf{u}}_{(EO)}$:

$$\mathbf{R}_m(EO) = \mathbf{\Phi}_m - \mathbf{Q}(EO) \begin{bmatrix} \mathbf{u}_{(EO)} \\ \bar{\mathbf{u}}_{(EO)} \end{bmatrix} = \mathbf{\Phi}_m - \mathbf{Q}(EO) \left(\mathbf{H}^{-1} \otimes \mathbf{I}\right) \mathbf{\Phi}_m, \tag{95}$$

where the vector $\mathbf{R}_m(EO)$ is the vector of residuals for the mode m which is a function of the engine order excitation EO. To normalize the magnitude of the residual between a scale from 0 to 1, the norm of the residual is divided by the norm of the mode $\mathbf{\Phi}_m$, and is subtracted from 1. The normalized residual can be written as,

$$R_m(EO) = 1 - \frac{||\mathbf{R}_m(EO)||}{||\mathbf{\Phi}_m||}. \tag{96}$$

The residual in Eq. (96) represents the resemblance between a vane packet mode and a rotationally periodic motion, and consequently a traveling wave excitation. When the value of $R_m(EO)$ is close to 0, it indicates that the mode is not excited to the excitation. On the other hand, if the $R_m(EO)$ is close to 1, it implies that the mode is most responding to the excitation. The values of $R_m(EO)$ are plotted as a function of the mode number m and the engine order EO in Fig. 41. To visualize the residuals, the norm of the residuals are represented in different colors; red indicates values close to 1 and blue indicates values close to 0. The color plot in Fig. 41 shows insightful information between the harmonic excitations and the responding modes. At the engine order 46, for instance, the 16th, 36th and 44th modes are dominantly responding. At low engine orders, however, between 0 to 10, multiple modes are coupled. Those modes which are responding to low engine order excitations (boxed with solid line in Fig. 41 (top)) exhibit strong coupling between the blades and the platform. However, in the region of high modal density, boxed with dash line, it is observed that blades are dominantely responding. As the excitation frequency increases, the tendancy of the coupling between the blades and the platform changes periodically.

5.3. Reduced-order modelings

In this section, a novel ROM of a vane packet with blade-to-blade stiffness and damping variability is introduced, and a derivation of the mathematical model for calculating the amplification factors is presented.

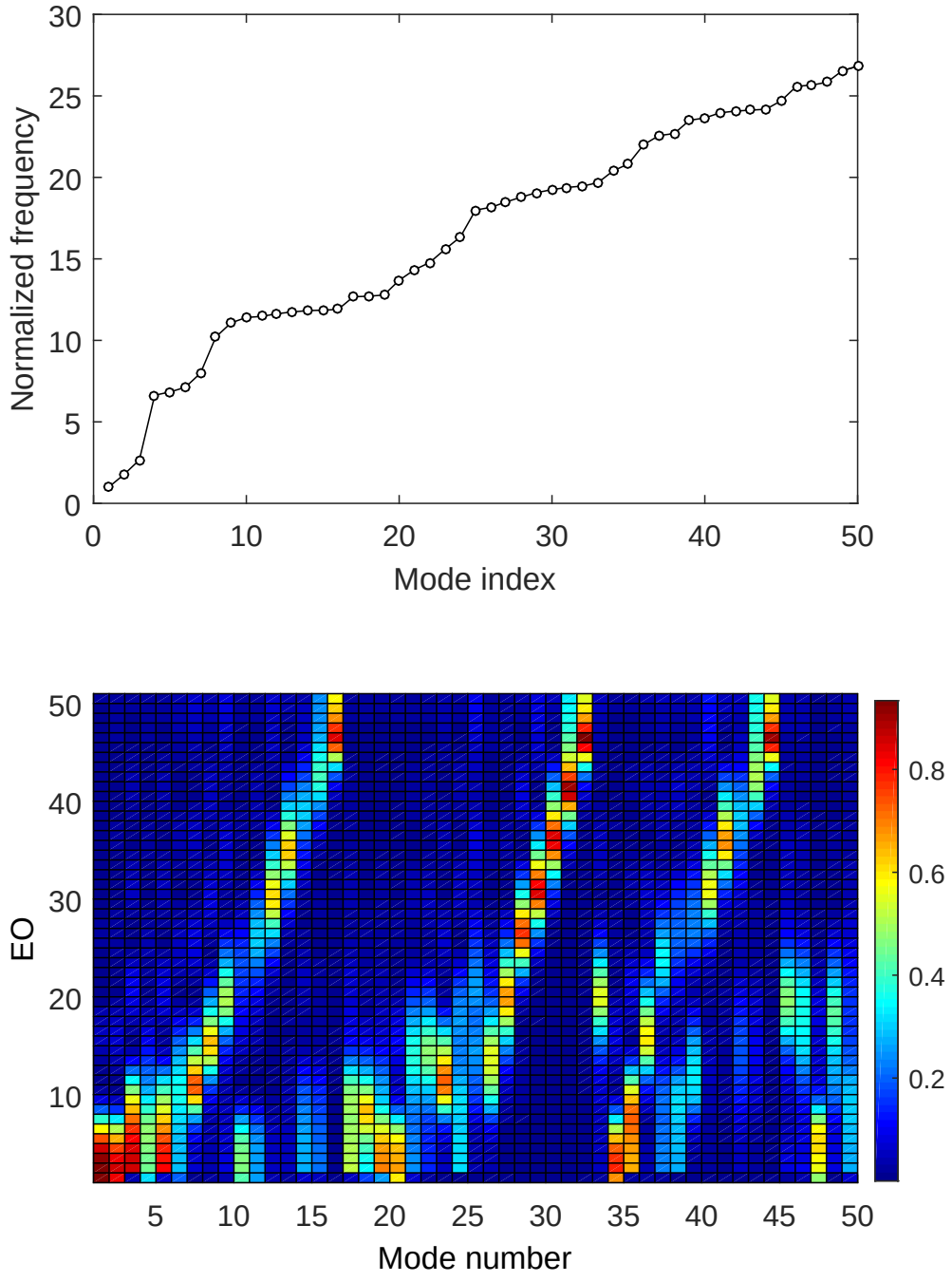

Figure 41: First 50 system frequencies of the vane model normalized by the first natural frequency (top), and waterfall plot of the magnitude of the residuals (bottom)

First, a brief review of the ROMs developed by Joshi [29] is introduced. Joshi's method, previously applied

to a general bladed disk with blade-to-blade damping variability, is modified and extended to a vane packet model. Results of the force responses from the ROMs and from the full FE model are compared. Second, an analytic model to accelerate the computation of amplification factors is derived.

5.3.1. Reduced order modeling of mistuned vane

Lim [14] developed a novel ROM, named component mode mistuning (CMM), which is capable of capturing the effect of stiffness and mass mistuning on the dynamic responses of bladed disks. Joshi [29] generalized the concept of CMM, and extended it to the case involving damping variability among blades. In this section, Joshi's ROM is reviewed briefly. Then, the ROM is applied to a vane packet model. Results of the forced responses are obtained by using the full FEM and the developed ROM. Joshi characterized each mistuning in damping as the deviations of the structural damping coefficient of each blade from its nominal (tuned) value. Thus, the damping variation at the j^{th} blade is defined as

$$\gamma_j = \gamma_{avg} + \gamma_j^{\delta}, \tag{97}$$

where γ_j is the structural damping coefficient for the j^{th} blade, γ_{avg} is the average damping in the entire blisk which is also the structural damping coefficient of the tuned configuration, and γ_j^{δ} is the deviation of the damping coefficient for the j^{th} blade. The structural damping matrix ($\mathbf{C}$) of the entire blisk can be expressed as

$$\mathbf{C} = \mathbf{C}^S + \sum_{j=1}^{N} \mathbf{C}_j^{\delta}, \tag{98}$$

where $\mathbf{C}^S$ is the structural damping matrix of the tuned blisk, $\mathbf{C}_j^{\delta}$ is the damping mistuning matrix of the j^{th} blade, and N is the number of blades. Note that the structural damping matrix can be expressed as a product of a structural damping coefficient and the stiffness matrix. Thus, Eq. (98) can be written as

$$\mathbf{C} = i\gamma_{avg}\mathbf{K}^S + \sum_{j=1}^{N} i\gamma_j^{\delta}\mathbf{K}_j, \tag{99}$$

where i is the imaginary unit, $\mathbf{K}^S$ is the stiffness matrix of the tuned system, and $\mathbf{K}_j$ is the stiffness matrix of the j^{th} blade. In CMM, motions of a blade are characterized as a linear combination of cantilevered blade (CB) normal modes and constraint modes

$$\mathbf{\Phi}_j^S = \begin{bmatrix} \mathbf{\Phi}_o^B & \mathbf{\Psi}_o^B \\ \mathbf{0} & \mathbf{I} \end{bmatrix} \begin{bmatrix} \mathbf{q}_{\Phi,j} \\ \mathbf{q}_{\Psi,j} \end{bmatrix}, \tag{100}$$

where $\mathbf{\Phi}_j^S$ is the tuned system modes of the j^{th} blade, $\mathbf{\Phi}_o^B$ is the normal modes of a tuned cantilevered blade, $\mathbf{\Psi}_o^S$ represents the constraint modes, $\mathbf{q}_{\Phi,j}$ is the modal participation factors of the cantilevered blade normal modes, and $\mathbf{q}_{\Psi,j}$ is the modal participation factors of the constraint modes. Mass and stiffness matrix of the j^{th} blade, $\mathbf{M}_j$ and $\mathbf{K}_j$ respectively, can be divided into tuned and mistuned components as

$$\begin{aligned}\mathbf{M}_j &= \mathbf{M}_j^S + \mathbf{M}_j^\delta,\\ \mathbf{K}_j &= \mathbf{K}_j^S + \mathbf{K}_j^\delta,\end{aligned} \tag{101}$$

where superscript S and δ implies tuned and mistuned terms. Note that tuned mass and stiffness matrices $\mathbf{M}_j^S$ and $\mathbf{K}_j^S$ are identical for all sectors. Since the constraint modes are negligible due to small contributions of the motion at the blade-casting interface, the mistuned mass and stiffness matrices at the j^{th} blade can be approximated as the mistuned mass and stiffness matrices of a cantilevered blade fixed at its root, i.e., $\mathbf{M}_j^\delta \approx \mathbf{M}_{CB,j}^\delta$, and $\mathbf{K}_j^\delta \approx \mathbf{K}_{CB,j}^\delta$. Thus, by introducing the transformation matrix defined in Eq. (100) to the mass and stiffness matrices from Eq. (101), the reduced mass $\boldsymbol{\mu}^{syn}$ and stiffens $\boldsymbol{\kappa}^{syn}$ matrices can be computed as

$$\begin{aligned}\boldsymbol{\mu}^{syn} &= \mathbf{I} + \sum_{j=1}^{N} \mathbf{q}^T {\boldsymbol{\Phi}_o^B}^T \mathbf{M}_{CB,j}^\delta \boldsymbol{\Phi}_o^B \mathbf{q},\\ \boldsymbol{\kappa}^{syn} &= \boldsymbol{\Lambda}^S + \sum_{j=1}^{N} \mathbf{q}^T {\boldsymbol{\Phi}_o^B}^T \mathbf{K}_{CB,j}^\delta \boldsymbol{\Phi}_o^B \mathbf{q}.\end{aligned} \tag{102}$$

Note that the the mistuning component of reduced-order stiffness matrix is approximately equal to the product of the matrix of eigenvalues of a tuned cantilevered blade $\boldsymbol{\Lambda}_{CB,j}^S$ and the diagonal matrix of the mistuning values δ_j.

$${\boldsymbol{\Phi}_o^B}^T \mathbf{K}_{CB,j}^\delta \boldsymbol{\Phi}_o^B \approx \boldsymbol{\Lambda}_{CB,j}^S \delta_j \tag{103}$$

By the same token, the damping mistuning matrix from Eq. (99) is projected onto the cantilevered blade modes as

$$\begin{aligned}\sum_{j=1}^{N} \mathbf{C}_j^\delta &\approx \sum_{j=1}^{N} \mathbf{q}^T {\boldsymbol{\Phi}_o^B}^T \mathbf{C}_{CB,j}^\delta \boldsymbol{\Phi}_o^B \mathbf{q}\\ &\approx i \sum_{j=1}^{N} \mathbf{q}^T \gamma_j^\delta \left[{\boldsymbol{\Phi}_o^B}^T (\mathbf{K}_{CB,j}^S + \mathbf{K}_{CB,j}^\delta) \boldsymbol{\Phi}_o^B \right] \mathbf{q}.\end{aligned} \tag{104}$$

Thus Eq. (104) combined with Eq. (102) and Eq. (104) gives

$$\begin{aligned}\Big[-\omega^2 \boldsymbol{\mu}^{syn} + (1 + i\gamma_{avg}) \boldsymbol{\Lambda}^S + \sum_{j=1}^{N} \mathbf{q}^T (1 + i\gamma_{avg}) \boldsymbol{\Lambda}_{CB,j}^S \delta_j \mathbf{q}\\ + i \sum_{j=1}^{N} \mathbf{q}^T \gamma_j^\delta \boldsymbol{\Lambda}_{CB,j}^S (1 + \delta_j) \mathbf{q} \Big] \mathbf{p}_\Phi^S = {\boldsymbol{\Phi}^S}^T \mathbf{f}.\end{aligned} \tag{105}$$

The ROM in Eq. (105) captures variability in damping from blade to blade along with stiffness mistuning.

5.3.2. Unit damping mistuning

The proposed ROM provides advantages of computational efficiency for simulating a huge number of damping mistuning patterns. The ROM shows good performance for a statistical analysis to characterize the

effects of random mistuning patterns. However, the performance of the ROM is considerably dependent on the length of the forcing frequency range of interest and the number of cantilevered blade modes. Moreover, the statistical analysis has to be repeated depending on the number of engine order excitations. For example, the whole vane system comprises 100 blades ($N_s \times N_p$) which requires at least 51 engine order excitations ($\frac{N_s \times N_p}{2} + 1$) to investigate the maximum response level. Therefore, repetitive analyses for each of the 51 engine orders significantly increase the computational cost. To address this issue, a new approach resolving the computational inefficiency due to a large number of statistical analyses is developed.

A damping mistuning deviation at each blade can be written as a vector $\boldsymbol{\gamma}^\delta$ in which each component indicates the deviation of the structural damping coefficient of each blade,

$$\boldsymbol{\gamma}^\delta = \left[\gamma_1^\delta \ \cdots \ \gamma_{N_s}^\delta\right]^T, \tag{106}$$

where $\gamma_1^\delta, \cdots, \gamma_{N_s}^\delta$ are the damping mistuning deviations of each blade from the nominal structural damping coefficient. Here, the unit damping mistuning is defined as a mistuning pattern that only a unit deviation $\bar{\gamma}^\delta$ is present at a single blade, while the nominal damping deviation γ_o^δ is applied to all blades to maintain zero mean damping mistuning deviation. Therefore, the unit damping mistuning vector $\boldsymbol{\gamma}^j$ is formulated for the j^{th} blade, written as

$$\boldsymbol{\gamma}^j_{N_s \times 1} = (\gamma_k)_{k=1,\cdots,N_s}, \quad \text{where } \gamma_k = \begin{cases} \gamma_o^\delta & k \neq j \\ \gamma_o^\delta + \bar{\gamma}^\delta & k = j \end{cases}. \tag{107}$$

Note that the sum of all entities in the unit damping mistuning vector is zero ($\bar{\gamma}^\delta + N_s\gamma_o = 0$). In Fig. 42, a unit damping mistuning pattern is shown where the unit damping is applied to the 3^{rd} blade.

Moreover, a damping mistuning deviation can be decomposed by the linear combination of the unit damping mistuning vectors. Thus, the damping mistuning deviation vector from Eq. (106) can be expressed as

$$\boldsymbol{\gamma}^\delta_{N_s \times 1} = \left[\boldsymbol{\gamma}^1 \ \cdots \ \boldsymbol{\gamma}^{N_s}\right] \boldsymbol{\zeta}_{N_s \times 1} = \left[\bar{\gamma}^\delta \mathbf{I} + \gamma_o^\delta \mathbf{B}\right]_{N_s \times N_s} \boldsymbol{\zeta}_{N_s \times 1}, \tag{108}$$

in which $\mathbf{B}$ is the binary matrix whose entires are all 1, $\mathbf{I}$ is the identity matrix, and $\boldsymbol{\zeta}$ is the vector of scalar multiples. From Eq. (108), the expression of the damping mistuning deviation of the j^{th} blade can be expressed as

$$\gamma_j^\delta = \gamma_o^\delta \sum_{k=1}^{N_s} \zeta_k + \bar{\gamma}^\delta \zeta_j = \gamma_o^\delta \tilde{\zeta} + \bar{\gamma}^\delta \zeta_j = \gamma_o^\delta \tilde{\zeta} - \gamma_o^\delta N_s \zeta_j, \tag{109}$$

where $\tilde{\zeta}$ is the summation of all the scalar multiples.

For simplicity, we assume that only one tuned system normal mode participates in the ROM ($\boldsymbol{\Phi}^{s^T} = \boldsymbol{\Phi}^{s^T}_{DOF \times 1}$). By adopting the expression in Eq. (109), Eq (105) can be rewritten as,

$$\left[\Theta + \sum_{j=1}^{N_s} \mathbf{q}^T (1 + i\gamma_{avg}) \boldsymbol{\Lambda}^S_{CB,j} \delta_j \mathbf{q} + i\tilde{\zeta}\gamma_o^\delta \bar{K}_{CB} - i\gamma_o^\delta N_s \sum_{j=1}^{N_s} \zeta_j \bar{K}_{CB,j}\right] p^s = \boldsymbol{\Phi}^{s^T} \mathbf{f}, \tag{110}$$

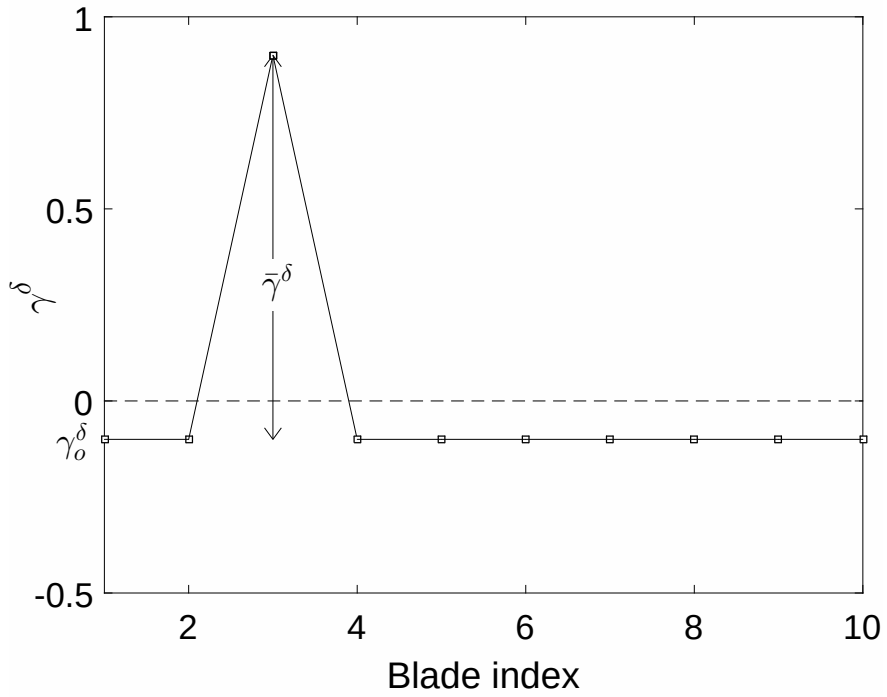

Figure 42: A unit damping mistuning pattern where the unit damping $\bar{\gamma}^\delta$ is applided at blade number 3 and the nominal damping γ_o^δ is distributed over the blades

where

$$\Theta = -\omega^2 \mu^{syn} + (1 + i\gamma_{avg})\Lambda^S, \tag{111}$$

and

$$\bar{K}_{CB} = \sum_{j=1}^{N_s} \bar{K}_{CB,j} = \sum_{j=1}^{N_s} \mathbf{q}^T \mathbf{\Lambda}^S_{CB,j}(1 + \delta_j)\mathbf{q}. \tag{112}$$

Note that the matrix Θ represents the dynamic stiffness of the tuned system, and $\mathbf{\Phi}^{sT}\mathbf{f}$ is a scalar modal force The modal amplitude of the tuned system p_t^s where the system is uniformly damped with the average structural damping γ_{avg} without stiffness mistuning ($\delta_j = 0$) can be found as $p_t^s = \Theta^{-1}\mathbf{\Phi}^{sT}\mathbf{f}$. Eq. (110) can be rearranged by factoring ζ_j out as

$$\begin{aligned}\Bigg[\sum_{j=1}^{N_s} \zeta_j \underbrace{\left(\Theta + \sum_{k=1}^{N_s} \mathbf{q}^T(1 + i\gamma_{avg})\mathbf{\Lambda}^S_{CB,k}\delta_k\mathbf{q} + i\gamma_o^\delta \bar{K}_{CB} - i\gamma_o^\delta N_s \bar{K}_{CB,j}\right)}_{\bar{\Theta}_j} \\ + (1 - \tilde{\zeta})\left(\Theta + \sum_{j=1}^{N_s} \mathbf{q}^T(1 + i\gamma_{avg})\mathbf{\Lambda}^S_{CB,j}\delta_j\mathbf{q}\right)\Bigg] p^s = \mathbf{\Phi}^{sT}\mathbf{f}.\end{aligned} \tag{113}$$

It is worth noting that the $\bar{\Theta}_j$ is the dynamic stiffness of the system when the unit damping mistuning is introduced to the j^{th} blade. Thus, the modal amplitude of the ROM with unit damping mistuning p_j^s can be predicted as $p_j^s = \bar{\Theta}_j^{-1}\mathbf{\Phi}^{sT}\mathbf{f}$. By dviding each side of Eq. (113) with $\mathbf{\Phi}^{sT}\mathbf{f}$, the following expression is

obtained

$$\sum_{j=1}^{N_s} \zeta_j \frac{1}{p_j^s} + (1-\tilde{\zeta})\frac{1}{p_m^s} = \frac{1}{p^s}, \tag{114}$$

where p_m^s is the modal amplitude of the mistuned system with only stiffness deviations

$$p_m^s = \left[\Theta + \sum_{j=1}^{N_s} \mathbf{q}^T(1+i\gamma_{avg})\mathbf{\Lambda}_{CB,j}^S \delta_n \mathbf{q}\right]^{-1} \left(\mathbf{\Phi}^{sT}\mathbf{f}\right), \tag{115}$$

and p_m^s is independent to the damping mistunings. The ratio between the tuned and mistuned modal amplitudes and the relationship among the ratios can be observed by multiplying each side of Eq. (114) by the modal amplitude of the tuned system p_t^s as

$$\sum_{j=1}^{N_s} \zeta_j \frac{p_t^s}{p_j^s} + (1-\tilde{\zeta})\frac{p_t^s}{p_m^s} = \frac{p_t^s}{p^s}. \tag{116}$$

Equation (116) represents the relationship among the amplitude ratios at a fixed mode. When the multiple modes participate in the ROM, however, the following inequality holds

$$\sum_{j=1}^{N_s} \zeta_j \frac{max(\mathbf{p}_t^s)}{max(\mathbf{p}_j^s)} + (1-\tilde{\zeta})\frac{max(\mathbf{p}_t^s)}{max(\mathbf{p}_m^s)} \leq \frac{max(\mathbf{p}_t^s)}{max(\mathbf{p}^s)}, \tag{117}$$

where $\mathbf{p}_t^s$, $\mathbf{p}^s$, $\mathbf{p}_j^s$, and $\mathbf{p}_m^s$ are the vectors of the participation factors of the tuned system, the mistuned system, the system with unit damping mistuning at sector j, and the system with stiffness mistuning, respectively. Since an amplification factor (AF) is defined as the ratio of the maximum mistuned forced response amplitude to the maximum tuned forced response amplitude, the AF can be represented as the ratio between the modal amplitudes of the mistuned system and the tuned system. Therefore, Eq. (116) can be substituted by amplification factors as

$$\frac{\zeta_1}{AF_1} + \frac{\zeta_2}{AF_2} + \cdots + \frac{\zeta_{N_s}}{AF_{N_s}} + \frac{(1-\tilde{\zeta})}{AF_m} \leq \frac{1}{AF}, \tag{118}$$

where $AF_{j,(j=1,\cdots,N_s)}$ refers to the amplification factor of the mistuned system when a unit damping is introduced at j^{th} blade, and AF_m is the amplification factor of the mistuned system in which only the sitffness variations are presented amongst the blades. The inequality in Eq. (118) represents the upper bound of an amplification factor induced from a damping variation amongst the blades. Moreover, it implies that the value of the upper bound can be calculated by decomposing the amplification factor into the amplification factors obtained from the unit damping mistuning and the stiffness mistuning. The values of the amplification factors AF_j and AF_m are pre-calculated, thus the upper bound of any amplification factors can be predicted easily by solving the simple algebraic equation, and adjusting the scalar multiples ζ_j. This eliminates the necessity for repetitive constructions of the ROM in Eq. (105) so that it accelerates the speed of the computations for statistical analyses of large numbers of mistuning patterns.

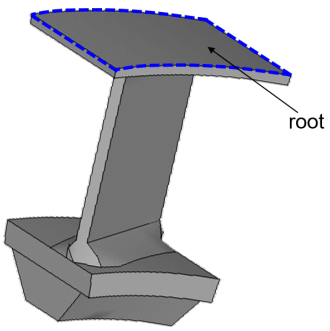

Figure 43: A cantilevered vane sector FE model

5.4. Results

5.4.1. Validation of ROM

The introduced ROM is developed primarily for general bladed disk systems. To examine the validity and the performance of the developed ROM when applied to a vane packet model, forced response results from the ROM and full FE model of the vane packet are compared. The cantilevered blade modes are obtained by extracting the normal mode of the vane sector with clamped root of the casting sketched in Fig. 43. Stiffness and damping mistuning is introduced only to the blade components. The CMM technique is based on the assumption that blade mistuning is small compared to nominal properties in the modal domain. A pattern of small stiffness deviation at each blade with 0.03 standard deviation (STD) is plotted in Fig. 44. The system frequencies calculated from the full FE analysis in ANSYS (f_{ANSYS}) and from the ROM (f_{ROM}) are compared. The relative error defined in Eq. (119) is plotted in Fig. 45. In this demonstration, the ROM only includes the first 7 CB modes. Including additional CB modes beyond the 7^{th} mode have negligible effects on the result.

$$\%\text{error in system frequency} = \frac{|f_{ANSYS} - f_{ROM}|}{f_{ANSYS}} \times 100 \tag{119}$$

To validate the ROM of the vane model including damping mistuning, the forced response results were compared to the forced response results from the harmonic response analysis on a full order FE model in ANSYS. Traveling wave excitations are adopted as the external forcing, which can be expressed as

$$\mathbf{F}_j = F_{amp} e^{i\frac{2\pi EO(j-1)}{N_s N_p}}, \tag{120}$$

where F_{amp} is the magnitude of the force applied to the blades. The traveling wave excitation consists of a fixed engine order with a unit nodal load applied on the middle of each blade leading edge along the axial direction.

For the damping variations from blade to balde, two different damping mistuning deviations are examined. The variations in the structural damping coefficient were chosen within $-90\% \sim +150\%$ of the average damping value (γ_{avg}). The damping mistuning deviation has the zero mean value so that the average value

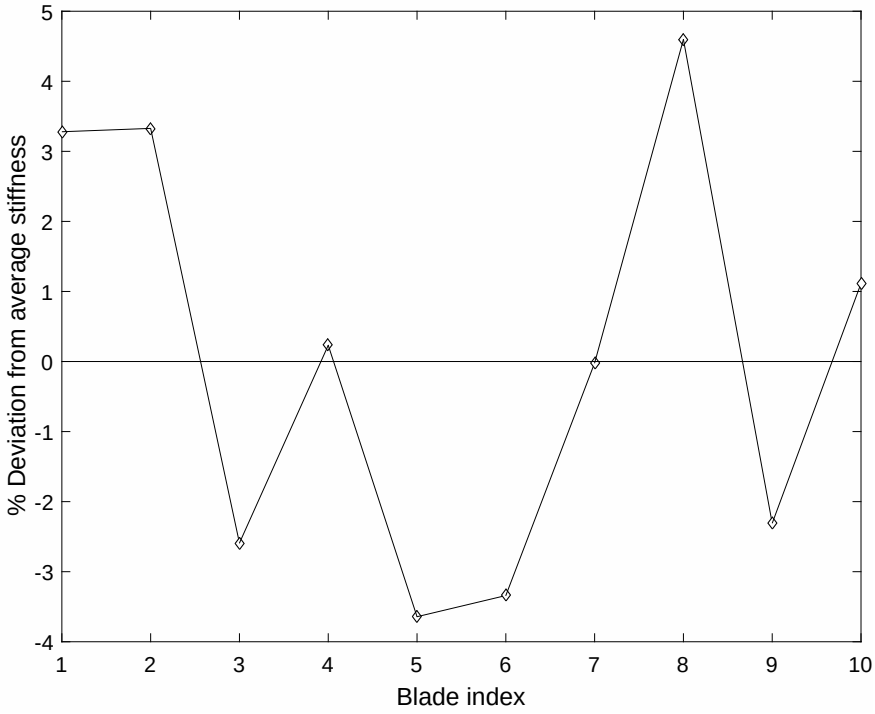

Figure 44: Stiffness mistuning variation between the blades with 0.03 standard deviation

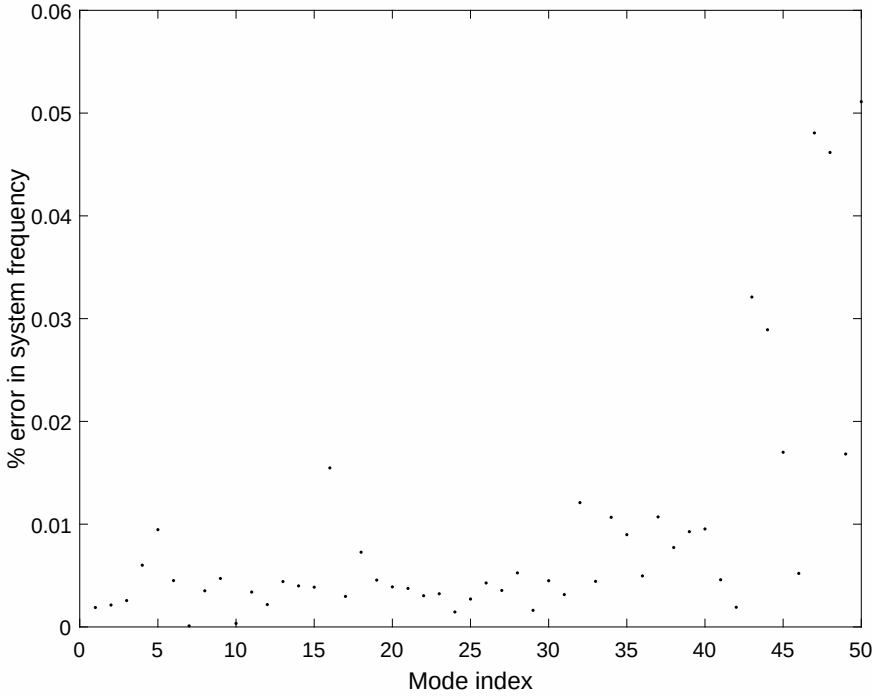

Figure 45: System frequency relative error between ROM and full order analysis

of the damping in all the blades is equal to the tuned damping coefficient. Figure 46 shows the two damping mistuning patterns with different standard deviations. The forced responses are computed by the full-order analyses and the ROM, and the maximum physical displacement amplitudes are extracted. The maximum

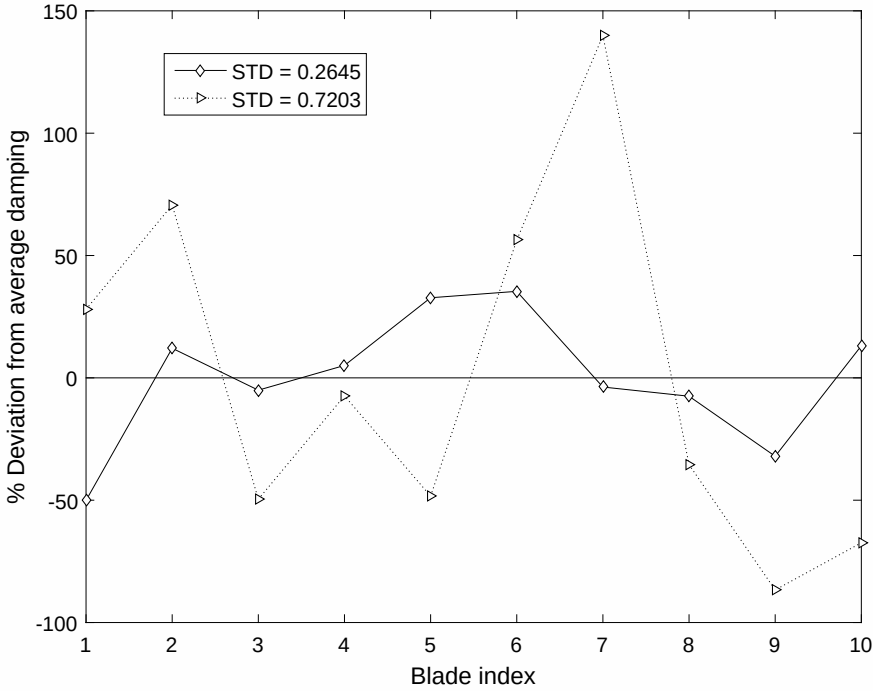

Figure 46: Damping mistuning pattern with two different standard deviations: STD = 0.2645 (-◇-) and STD = 0.7203 (-▷-)

displacement amplitudes versus forcing frequency are plotted in Fig. 47 and 48, where the forced responses excited by engine order 1, 6, 30 and 50 are shown. The relative errors comparing the predicted forced responses at the natural frequencies are plotted in Fig. 47 and 48. The ROMs capture the effect of damping variations very accurately. The maximum errors at both cases are less than 1% indicating a good agreement between the ROM and the reality.

The ROMs are used to calculate the forced responses with a large number of damping mistuning patterns with different standard deviations. The information of forced responses from the large populations of mistuning patterns can be informatively shown through the amplification factor distributions. The amplification factors (AF), the ratio of the maximum mistuned forced response amplitude to the maximum tuned forced response amplitude, are investigated within the first 20 modes. The natural frequencies associated with the first 20 modes exist within this frequency range. Figure. 49 shows a dense cloud of amplification factor distributions along the corresponding standard deviation of the damping mistuning pattern. There are 205,000 cases of pseudo-random damping mistuning patterns. For every mistuning pattern, the mean value of the damping coefficients of all the blades is equal to that of a tuned blade. The line of mean value and the 95^{th} percentile is also shown in Figs. 49 and 50.

5.4.2. Statistical investigation using unit damping mistuning

Next, statistical analyses are conducted by using a large number of damping mistuning patterns. The similar statistical studies done by the ROMs were performed by the unit damping mistuning. Comparing the results from the both approaches, the accuracy of the unit damping mistuning method are validated. One

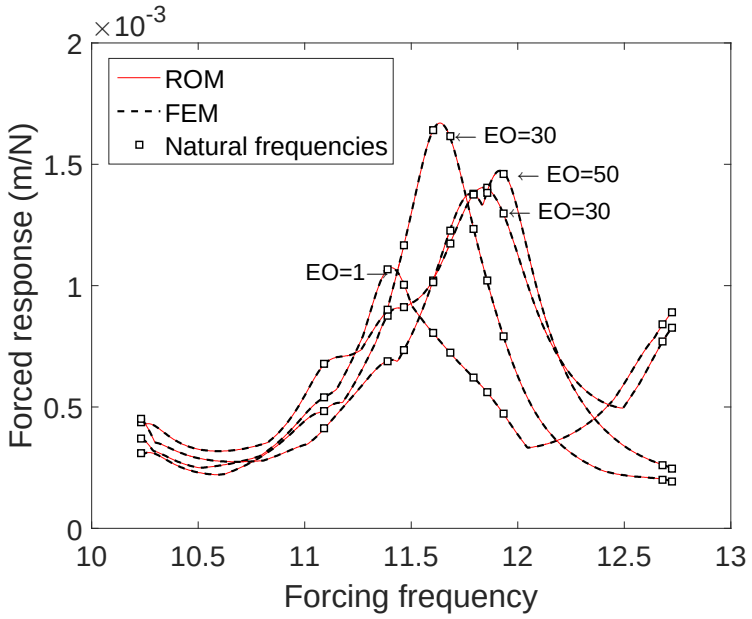

Figure 47: Forced response (STD = 0.2645)

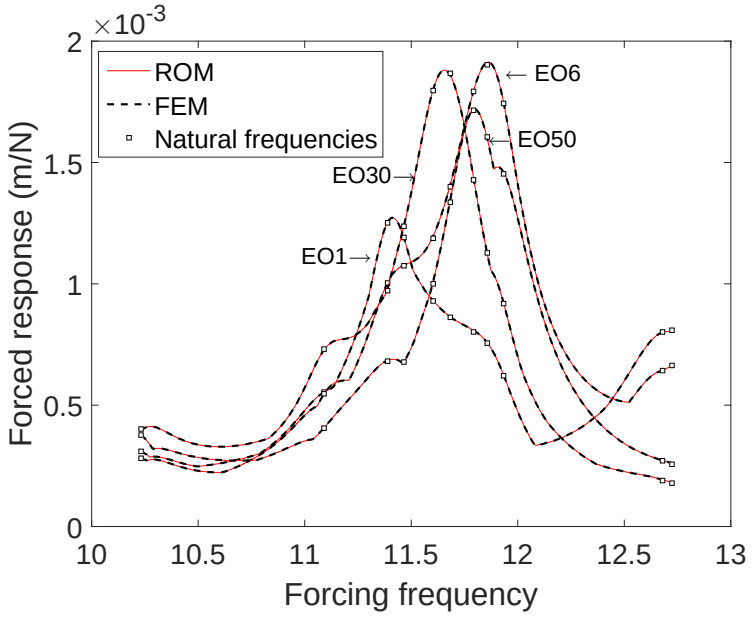

Figure 48: Forced response (STD = 0.7203)

of the damping mistuning patterns is chosen from the randomly generated patterns used in Figs. 49 and 50. The selected damping mistuning variation amongst the blades γ_j^δ and the corresponding scalar multiples ζ_j obtained by Eq. (108) are listed in Table. 2. The transformation matrix in Eq. (108) is well-conditioned since it comprises a linear combination of an identity matrix and a Binary matrix. Hence, ζ_j can be obtained easily by taking the inverse of the matrix. Note that the ζ_j values are all positive so that the sum of the multiples $\tilde{\zeta}$ is not 0. Instead, the sign of the unit damping mistuning $\bar{\gamma}_j^\delta$ is decided by the sign of the mistuning variation

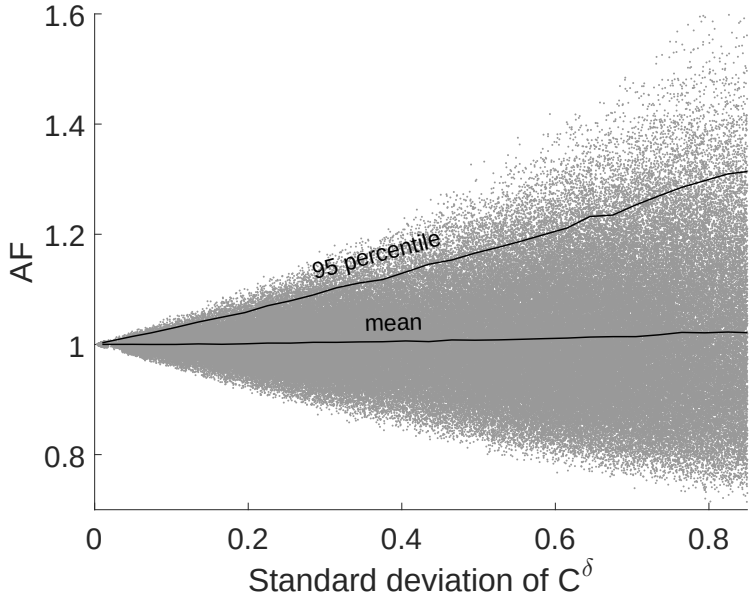

Figure 49: Amplification factor distribution of 205,000 different damping mistuning cases (EO6)

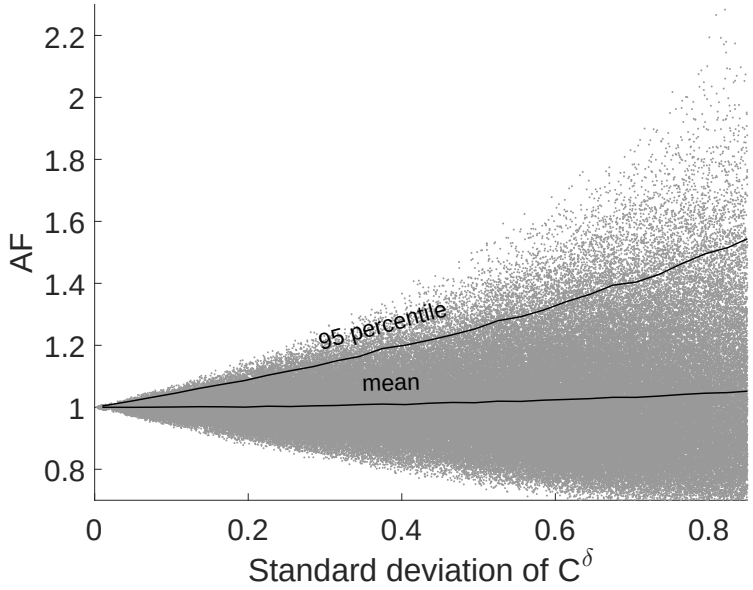

Figure 50: Amplification factor distribution of 205,000 different damping mistuning cases (EO40)

γ_j^{δ}. In Fig. 51, the damping mistuning variation and the reproduced mistuning pattern by the unit damping mistuning are plotted together.

The procedure of the unit damping mistuning method is explained as follows. First, the unit damping variation $\bar{\gamma}^{\delta}$ is introduced to the first blade, while the nominal damping variation γ_o^{δ} is applied to all blade. Note that the mean value of the overall damping variation among the blades remains 0. Second, the forced responses within the frequency range of intereset, under the excitation of each engine order, are computed by ROMs. Lastly, the amplification factors are computed by extracting the maximum response level from

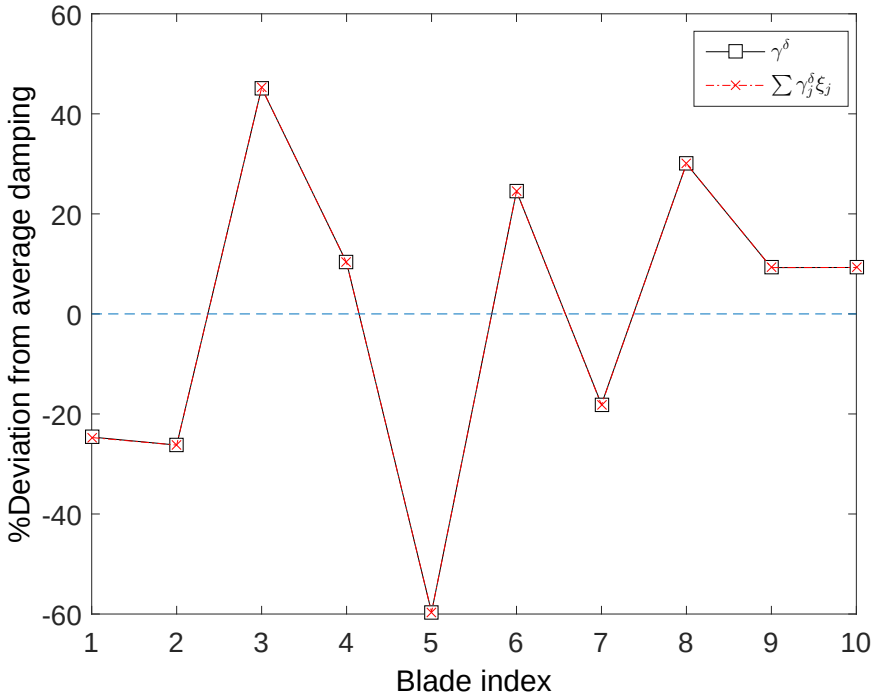

Figure 51: A pattern of damping deviation γ_j^δ from the average damping (-□-) and the replicated damping deviation by the unit damping mistuning $(\gamma_o + \bar{\gamma}^\delta)\zeta_j$ (-×-)

the results obtained in the previous step. This procedure is repeated consecutively to the other blades. In Figs. 52 and 53, the unit damping mistuning patterns are plotted. In this figure, only four examples, which the unit damping mistuning is introduced to blade 1 and 2 are shown. The corresponding amplification factors obtained from the ROMs are also plotted together.. Once this procedure is done, amplification factors of a mistuned system can be easily computed with simple algebraic calculation as described in Eq. (118).

The results in Fig. 54 show the amplification factors of the mistuned vane packet predicted by the ROM and by the unit damping mistuning method for comparision. The mistuned vane packet has the stiffness variation amongst the blades with a standard deviation of 0.03 as well as the damping variation with a standard deviation of 0.316. The stiffness and damping mistuning patterns are shown in Fig. 44 and 51, respectively. The maximum error between the ROM predictions and validation data is 0.006%, which shows

Table 2: Values of damping mistuning variation γ_j^δ, scalar multiples ζ_j, and unit damping $\bar{\gamma}^\delta$

	1	2	3	4	5	6	7	8	9	10
γ_j^δ	-0.25	-0.26	0.45	0.10	-0.60	-0.25	-0.18	-0.30	0.09	0.09
ζ_j	2.50	2.60	4.50	1.00	6.00	2.50	1.80	3.00	0.90	0.90
$\bar{\gamma}^\delta$	-0.10	-0.10	0.10	0.10	-0.10	-0.10	-0.10	-0.10	0.10	0.10

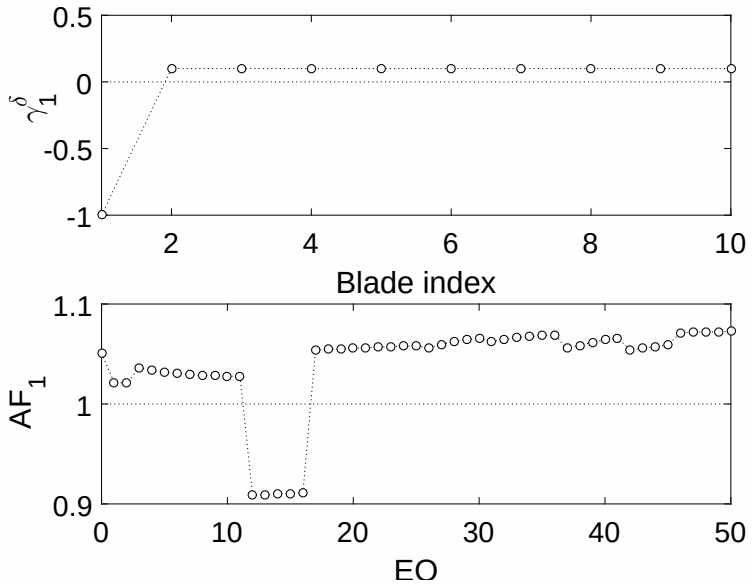

Figure 52: Unit damping mistuning pattern and corresponding amplification factors for engine order excitation from 0 to 50 (Unit damping mistuning at blade 1)

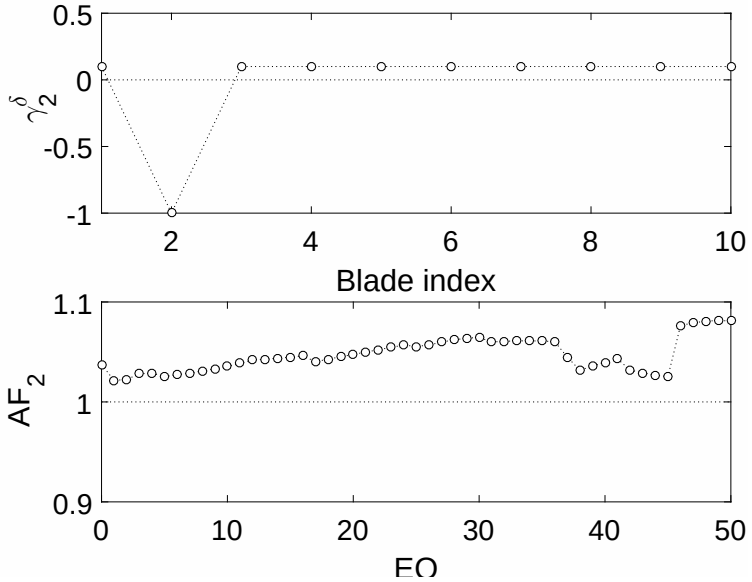

Figure 53: Unit damping mistuning pattern and corresponding amplification factors for engine order excitation from 0 to 50 (Unit damping mistuning at blade 2)

a very good agreement.

Amplification factors for any damping mistuning pattern can be predicted simply by replacing the scalar multiples ζ_j and solving the algebraic equation in Eq. (118). This methodology provides great advantages in saving the computational cost, so that it can be effectively used to accelerate the statistical analyses. The same statistical investigations which are shown in Figs. 49 and 50 are performed by using the unit damping mistuning approach.

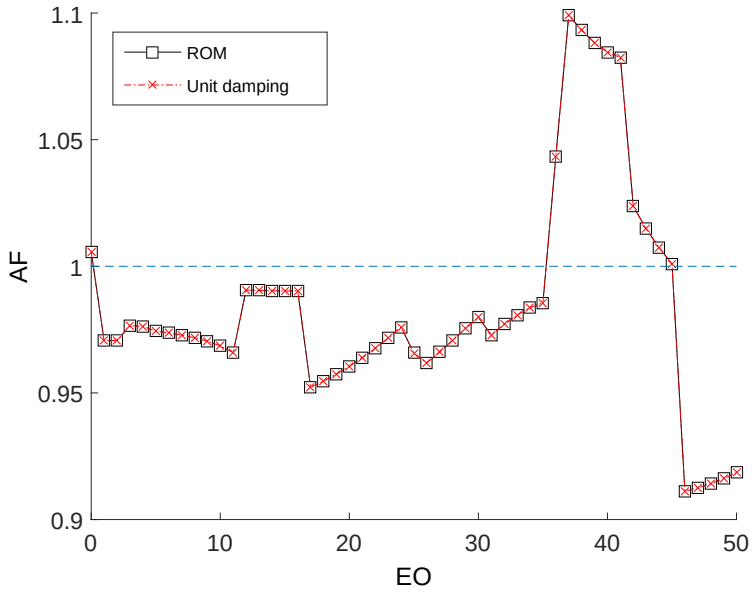

Figure 54: Amplification factors (AF) calculated from ROM (-□-) and unit damping mistuning (-∗-)

The amplification factor predictions of 205,000 different cases of damping mistuning at a fixed stiffness variation are examined. The predicted amplification factor distributions are shown in Figs. 55 and 56. Those are the amplification factor distributions under engine order excitation 6 and 40, respectively. The relative errors of the predictions between the ROM and the unit damping mistuning method are also plotted together in Fig. 57. The maximum relative errors at both engine order excitations are 4.12×10^{-5} and 5.02×10^{-4} which are the negligibly small.

Furthermore, the unit damping mistuning method reduces the computational time drastically. The total computational time is drastically decreased owing to the simplicity of the calculation. For example, the statistical analyses of a total 205,000 computations shown in Fig. 49 took 14 hrs 21 mins. However, the same task performed by the unit damping mistuning method only took 29 sec. Due to its advantage of computational efficiency, the unit damping mistuning method was used to perform similar statistical analyses to all engine order excitations.

The statistically analyses were performed with the vane system under excitations of all engine orders, from 0 to 50, and the 95^{th} percentile of the blade amplification factors were also examined for all engine order excitations. Figure 58 shows the effects of random damping mistuning on the 95^{th} percentile of the amplification factors.

5.5. Discussion and conclusions

Novel methodology was developed to investigate the effect of damping mistuning of a vane packet. From a vane FE model, the dynamics and the characteristics of the modes were discussed. A mode based method for finding the most responded mode to the traveling wave excitations was studied. The normal mode at each vane sector was approximated as harmonic expansions of a pair of vectors. The residuals between the

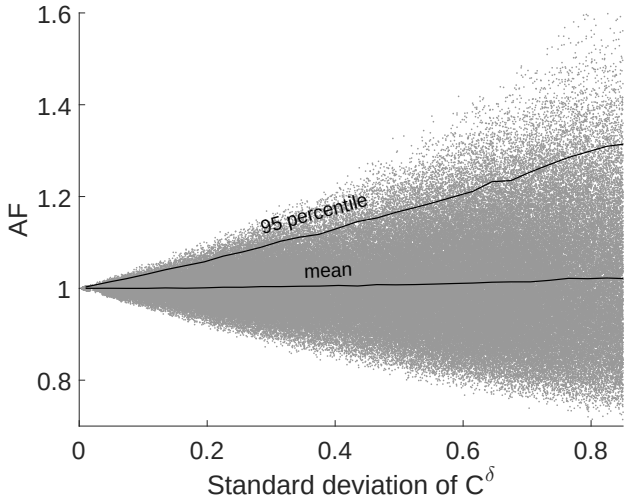

Figure 55: Amplification factor distribution of 205,000 different damping mistuning cases (EO6)

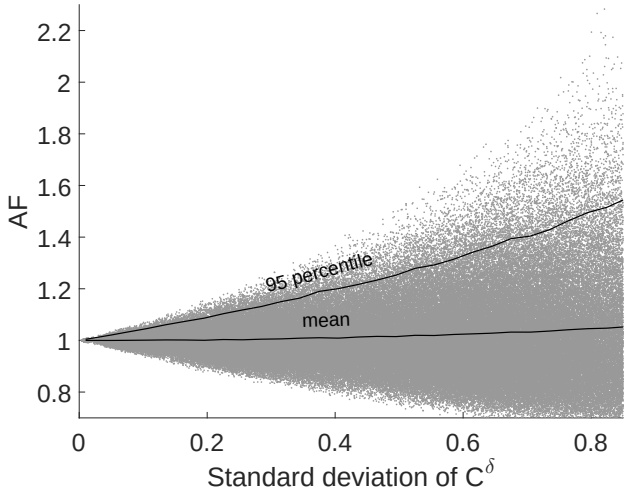

Figure 56: Amplification factor distribution of 205,000 different damping mistuning cases (EO40)

normal vane modes and the cyclically expanded modes were measured to examine the proximity of the vane mode to a cyclic symmetricity. The residuals at each engine order excitation was represented graphically in Fig. 41. The residual plot visualized the relationship between the engine order excitations and the responding modes. It was observed that the strong coupling between the platform and the blades at the low engine order excitations. The blade dominant modes were periodically shown in the regime of high modal density.

The ROMs for a vane model were developed to model damping mistuning in blades. The damping in the blades was modeled as structural damping. The ROMs used in this paper presents an extension to those studies from Joshi [29] and Lim [14]. A single structural damping coefficient was used to characterize damping in each blade. Variation in damping within a single blade was not considered. A large damping variation from the average damping value γ_{avg} was introduced between the blades. The forced responses computed from the ROMs and full order analysis showed very good match where the maximum relative error

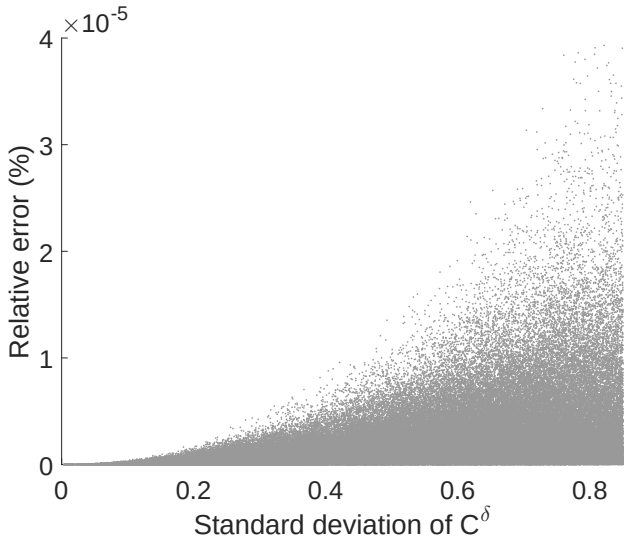

Figure 57: Amplification factor distribution of 205,000 different damping mistuning cases (EO6)

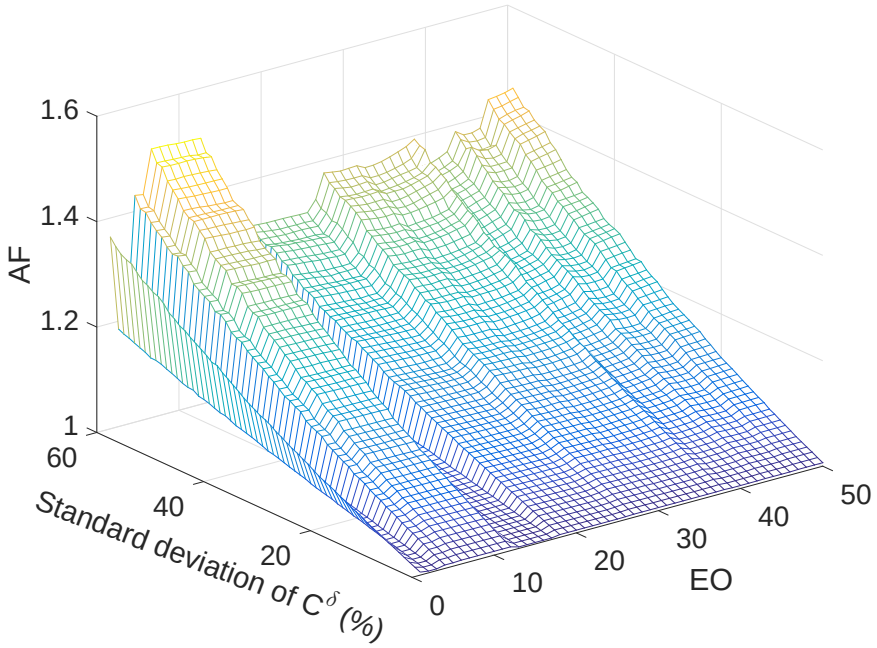

Figure 58: Surface plot of 95$^{\text{th}}$ percentile amplification factors for all engine order excitations

was 1%.

Based upon the ROM for a bladed disk with a ring damper, a method for the identification of the dynamic characteristics of nonlinear contact parameter have been developed. Contact parameters include the normal stiffness, tangential contact stiffness and contact friction coefficient. The analysis of nonlinear forced response for bladed disks with friction damping is performed by employing the lumped parameter model. The lumped parameter model comprises blade tip, blade root, disk and ring elements. Nonlinear contact force associated with friction is expressed by the nonlinear equivalent damping coefficient and stiffness. The

response dependent equivalent damping and stiffness are pre-calculated by quasi-static analysis, and are substituted for the nonlinear friction forces in the iterative solution. The developed ROM is verified by comparing the steady-state responses from time domain analysis and the ROM. Surrogate measurement points are obtained by selecting the forced responses near the peak response. By injecting 1% error for each measurement, the uncertainty of the measurement is included. The residual between the surrogate measurement point and the estimation by the ROM is obtained. The problem for finding the minimum residual with respect to contact parameters is solved by using gradient method. The procedure to obtain the residuals is repeated by changing the forcing amplitude level. The root mean square of the residuals from multiple forcing amplitude improves the accuracy of the contact stiffness identification.

CHAPTER 6

6. Summary and Key Contributions

6.1. Summary

Novel methodology was developed. There is great interest in developing a quick and reliable model for the modal mistuning of bladed disk systems. Although much research has been conducted to develop accurate models for the mistuning of the parts in these systems, many of these models are both time-consuming and computation-heavy, due to the complex nature of friction dampers in bladed disk systems as well as the vibratory patterns of mistuning. While these previous models may be useful in certain settings, a relatively accurate but efficient solution is oftentimes sufficient for testing the wear of bladed disk systems. Thus, proposed is a set of reduced-order models that retains the relative accuracy of the complex model while reducing computational time significantly. Three respective ROMs developed to predict the vibration tendencies in the bladed disk system are explained with their derivations as well as the results of their application in real-world settings.

The first ROM presented models small geometric mistuning in bladed disk systems. This novel modeling framework was developed by partitioning the system into a whole tuned bladed disk and several mistuning components in a sector level. A flow chart of the reduction process is provided in Fig. 18. First, sector level modes, mass, and stiffness matrices are obtained for both the tuned and mistuned sectors. Second, modes are aligned using a proper phase shift given by Eq. (14). Lastly, the tuned system modes expanded from the sector modes are used to form the ROM transformation matrix $\mathbf{T}_3$ given by Eq. (7) together with several additional vectors in $\mathbf{\Delta\Phi}$ which compensate for mode discrepancies due to small geometric variability. The additional vectors in $\mathbf{\Delta\Phi}$ were obtained by algebraically manipulating the difference between tuned and (aligned) cyclic mistuned modes. The new approach uses only sector-level calculations which provide significant savings in computational resources while accurately predicting system level frequencies and forced response. Moreover, only the blade portion of the modes are needed in $\mathbf{\Delta\Phi}$, and that further reduces the need for numerical computational resources. In the specific example, the total number of DOFs of the whole model was 235,788, compared to only 620 of the ROM. Repeated computations of cyclic symmetry analysis are required according to the number of mistuned blades to obtain the transformation matrix $\mathbf{T}_3$. However, the transformation matrix is computed using only sector level calculations, eliminating the need for extracting full order matrices. The vectors in $\mathbf{\Delta\Phi}$ are obtained by an algebraic subtraction between tuned and mistuned modes. Thus, those modes have to have the same number of DOFs.

Missing parts of blades or large changes in the mesh might cause this approach to fail. Numerical results for the academic blisk model were presented to demonstrate the effectiveness of the approach. The predicted natural frequencies and forced response results obtained for the ROM were in excellent agreement with the results from full order finite element analysis. The mistuning patterns used in this study include deformations in the length of the blades and in uneven blade tips which mimic some of the geometric mistuning observed in practice.

The second proposed ROM captures the nonlinear behavior due to contact friction in the ring damper element of the bladed disk system. The proposed approach is based on expressing the nonlinear force as response-dependent and iteratively solving the nonlinear system with response-dependent characteristics. The equivalent structural damping and stiffness are substituted for the nonlinear friction forces. To predict the steady-state responses under traveling excitations, the equivalent damping and stiffness values are nonlinear functions obtained by quasi-static analysis with imposed harmonic motions. The pre-calculated nonlinear equivalent damping and stiffness speeds up the iterative solution. A key advantage of the proposed approach is that it requires only sector level calculations to compute the response of the full wheel system. A full size FE model of a bladed disk and a ring damper system was used to demonstrate the method. The ROMs predict the steady-state responses with a significantly reduced computation time, efficiently and accurately.

Lastly, a ROM was developed to investigate the effects of damping mistuning of the vane packet s. From a vane FE model, the dynamics and the characteristics of the modes were discussed. A mode based method for finding the most responded mode to the traveling wave excitations was studied. The normal mode at each vane sector was approximated as harmonic expansions of a pair of vectors. The residuals between the normal vane modes and the cyclically expanded modes were measured to examine the proximity of the vane mode to a cyclic symmetricity. The residuals at each engine order excitation was represented graphically in Fig. 41. The residual plot visualized the relationship between the engine order excitations and the responding modes. It was observed that the strong coupling between the platform and the blades at the low engine order excitations. The blade dominant modes were periodically shown in the regime of high modal density. The performances of the unit damping mistuning approach were validated by comparing the results of the amplification factors to those obtained from the ROMs. The resulting amplification factors from the ROMs and the unit damping mistuning were shown in Fig. 54 along with the engine order excitations. The maximum error between the predictions was 0.006%.

Although past research has explored the independent contributors to vibration patterns and mistuning in bladed disk systems, few have been able to develop accurate models that retain the timeliness of a reduced version. All models have demonstrated high accuracy while simultaneously reducing computational power and time. The efficacy of these models proposes broad implications to the efficiency of modeling of mistuned blisks and vane system as well as the friction damper testing and design.

6.2. Key Contributions

The work described in this dissertation proposes efficient methods to accurately analyze vibrations of nonlinear systems and novel techniques to detect damages in bladed disks. The primary contributions of this dissertation are as follows:

- In Chapter 2, a novel method to construct small geometric mistuning in bladed disk systems was presented. The method allows constructing ROMs to capture the effect of small geometric mistuning in the blades by using only the sector level calculations. Since it removes the needs for extracting the full order matrix, it demonstrates a significant reduction of a computational time. It can be noted that the proposed approach is general and can be used any types of bladed disks.

- In Chapter 3, a novel methodology to investigate the nonlinear forced response of bladed disk with a dry friction ring damper was proposed. Efficient ROM was constructed replacing the nonlinear forces by the nonlinear equivalent damping and stiffness. Nonlinear terms are calculated at the previous step of the iterative solutions. The variations of the relative motions in contact pairs and the geometric complexity at the contact interfaces are accounted in the ROM. Therefore, proposed ROM is relatively easy to construct and computationally efficient to obtain the steady-state responses of the frictionally constrained bladed disk.

- In Chapter 4, a simple and straightforward method was developed to measure the contact stiffness and contact damping of realistic frictionally constrained bladed disks. The forced responses of the nonlinear structure were measured. Within the feasible ranges of the contact parameters, the forced responses of the nonlinear structure were predicted by using developed ROM in Chapter 3. The optimization problem to find the minimum residuals between the measurements and predictions was solved. It was observed that low forcing levels were adequate for identifying the contact stiffness.

- In Chapter 5, a new methodology was presented to investigate the mistuning effects on a vane packet. The most responding mode under traveling wave excitation was found by mode based calculations. This approach suggested a linear and a straight forward approach to investigate the dynamics and the characteristics of the vane structure. Based on CMM, a novel ROM was developed to examine the effect of damping mistuning in a vane packet. By using the developed ROM, only sector model was required to obtain free and forced response of the vane packet. Moreover, a simple algebraic equation for finding the upper bound of the amplification factors was derived. By removing the step for solving the ROM in every iterations, the algebraic equation drastically accelerated the speed of statistical analysis such as Monte Carlo simulations.

CHAPTER 7

7. Future work

Based on the work reported in this dissertation, some ideas for future research may be considered:

1. Prediction of the dynamic response of blisks with small geometric mistuning and a ring damper

The ROM studied in Chapter 2 shows good performances for predicting the forced responses of blisks with frictionally constrained dampers. In this study, however, the ring damper model is applied to only for the tuned bladed disk system. Bladed disk assemblies are often exposed to environments where the blades can experience geometric deformations. Thus, investigations of forced responses of a geometrically mistuned bladed disks with a ring damper may follow. In the Chapter 1, the methodology to construct the ROM for geometric mistuned bladed disks is studied. By combining the two methodologies developed in Chapter 1 and Chapter 2, the ROM can be constructed based on a sector level calculations. This can provide computationally efficient and accurate models to investigate the dynamic responses of geometrically mistuned bladed disks with a friction damper.

2. Experimental validation of the contact parameter identification

In Chapter 4, a methodology to identify the contact parameters is developed. Although the methodology represents good performances for identifying the contact parameters such as the normal stiffness, the tangential stiffness and the friction coefficients, the experimental data used in verification are surrogate measurement data which are basically numerical results. Further verifications of the methodology with experimental results are required.

3. Extension to systems with separation

The method suggested in this study shows good performances for blisks model where no separation occurs between the ring damper and the blisk. However, for certain speeds and certain geometries, the groove where the ring damper fits opens allowing for separation between the contact surfaces. Moreover, the ring damper can have three discontinuous flat contact surfaces. Some industrial models have curved ring damper designs, and that can create a gap between contact surfaces. The separation phenomenon was not considered in this study. Future work can be focused on validations of cases with separation.

4. Experimental validations of the contact parameter identification

The approach discussed in the Chapter 5 has shown promising results for finding the most responding mode at a given traveling wave excitation. The response level of a vane packet is predicted based on the mode level calculations. Also, the forced response of a mistuned vane packet are predicted and verified with full size of FE model. However, the further validations are required through the tests with experimental investigation of industrial vane models.

References

[1] D. J. Ewins, The effects of detuning upon the forced vibration of bladed-disks, Journal of Sound and Vibration 9 (1) (1969) 65–79.

[2] D. J. Ewins, Vibration chaaracteristics of bladed-disk assemblies, Journal of Mechanical Engineering 12 (5) (1973) 165–186.

[3] D. J. Ewins, Vibration modes of mistuned bladed disks, ASME Journal of Engineering for Power (3) (1976) 349–355.

[4] D. Whitehead, Effect of mistuning on the vibration of turbomachine blades induced by wakes, Journal of Mechanical Engineering Science 8 (1) (1966) 15–21.

[5] R. Dye, T. Henry, Vibration amplitudes of compressor blades resulting from scatter in blade natural frequencies, ASME Journal of Engineering for Power 91 (1969) 182–187.

[6] E. Capiez-Lernout, Soize, Nonparametric modeling of random uncertainties for dynamic response of mistuned bladed-disks, ASME Journal of Engineering for Gas Turbines and Power 126 (3) (2004) 610–618.

[7] D. J. Ewins, The effect of blade mistuning on vibration response - a survey, IFToMM 4th International conf. on Rotordynamics, Prague, Czechoslovakia.

[8] S. T. Wei, C. Pierre, Statistical analysis of the forced response of mistuned cyclic assemblies, AIAA Journal 28 (5).

[9]

[10] D. J. Ewins, Further studies of bladed disk vibration: Effects of packeting, Proceedings of the 2nd International converence on Vibrations in Rotating Machinery, Cambridge, U, K (1980) 97–102.

[11] J. H. Griffin, A review of friction damping of turbine blade vibration, International Journal of Turbo and Jet Engines 7 (1999) 297–307.

[12] R. Bladh, M. P. Castanier, C. Pierre, Reduced order modeling and vibration analysis of mistuned bladed disk assemblies with shrouds, ASME Journal of Engineering for Gas Turbines and Power 121 (3) (1999) 515–522.

[13] M. T. Yang, J. H. Griffin, A reduced order model of mistuning using a subset of nominal system modes, ASME Journal of Engineering for Gas Turbines and Power 123 (2001) 893–900.

[14] S.-H. Lim, R. Bladh, M. Castanier, Compact, generalized component mode mistuning representation for modeling bladed disk vibration, AIAA Journal 45 (9).

[15] R. Bladh, M. P. Castanier, C. Pierre, Component-mode-based reduced order modeling techniques for mistuned bladed disks-part i : Theoretical models, ASME Journal of Engineering for Gas Turbines and Power 123 (1) (2001) 89–99.

[16] R. Bladh, M. P. Castanier, C. Pierre, Component-mode-based reduced order modeling techniques for mistuned bladed disks-part ii: Application, ASME Journal of Engineering for Gas Turbines and Power 123 (1) (2001) 100–108.

[17] W.-h. Huang, Vibration of some structures with periodic random structures, AIAA Journal 20 (7). doi:10.2514/3.51159.

[18] G. Sogliero, A. V. Srinivasan, Fatigue life estimates of mistuned blades via a stochastic approach, AIAA Journal 18 (3) (1980) 318–323.

[19] K. K. Rao, E. K. Robert, Effects of mistuning on bending-torsion flutter and response of a cascade in incompressible flow, AIAA Journal April 9-10 (81-0532).

[20] A. Muszynska, D. I. G. Jones, T. Lagnese, L. Whitford, On non-linear response of multiple blade systems, Shock and Vibration Bulletin 51 (3) (May 1981) 88–110.

[21] A. V. Srinivasan, L. E. El-Bayoumy, The effect of mistuning on rotor blade vibration, AIAA Journal 13 (4). doi:10.2514/3.49731.

[22] S.-T. Wei, C. Pierre, Statistical analysis of the forced response of mistuned cyclic assemblies, AIAA Journal 28 (5) (1990) 861–868. doi:10.2514/3.25131.

[23] K. Y. S. E P Petrov, D. J. Ewins, A new method for dynamic analysis of mistuned bladed disks based on the exact relationship between tuned and mistuned systems, Journal of Engineering for Gas Turbines and Power 124 (3) (2002) 586–597. doi:10.1115/1.1451753.

[24] J. A. Judge, C. Pierre, O. Mehmed, Experimental investigation of mode localization and forced response amplitude magnification for a mistuned bladed disk, Journal of Engineering for Gas Turbines and Power 123 (2001) 940–950. doi:DOI: 10.1115/1.1377872.

[25] R. Bladh, C. Pierre, M. P. Castanier, M. J. Kruse, Dynamics response predictions for a mistuned industrial turbomachinery rotor using reduced-order modeling, Journal of Engineering for Gas Turbines and Power 124 (2) (2002) 311–324. doi:10.1115/1.1447236.

[26] J. J. H. Jeffrey S. Turcotte, R. W. Gordon, Vibration of a mistuned bladed-disk assembly using structurally damped beams, AIAA Journal 36 (12) (1998) 2225–2228. doi:10.2514/2.330.

[27] D. H. Afolabi, Vibration mistuned bladed disc assemblies, PhD. Thesis, University of London, London, UK.

[28] C. Siewert, H. Stuer, Forced response analysis of mistuned turbine bladings, ASME Turbo Expo 2010 6 (2010) 14–18. doi:10.1115/GT2010-23782.

[29] A. G. S. Joshi, B. I. Epureanu, Reduced order models for blade-to-blade damping variability in mistuned blisks, Journal of Vibration and Acoustics 134 (5). doi:10.1115/1.4006880.

[30] J. Awrejcewicz, D. Grzelczyk, Y. Pyryev, A novel dry friction modeling and its impact on differential equation and lyapunov exponents estimation, Journal of Vibroengineering 10 (4) (2008) 475–482. doi:ISSN 1392-8716.

[31] E. P. Petrov, D. J. Ewins, Effects of damping and varying contact area at blade-disc joints in forced response analysis of bladed disk assemblies, Journal of Turbomachinery 128 (2) (2006) 403–410. doi:ISSN 0889-504.

[32] M. Allara, S. Zucca, M. M. Gola, Effect of crowning of dovetail joints on turbine blade root damping, Key Engineering Material 347 (2007) 317–322.

[33] D. Charleux, F. T. C Gibert, J. Dupeux, Numerical and experimental study of friction damping blade attachments of rotating bladed disks, Journal of Rotating Machinery 2006 (71302).

[34] B. D. Yang, C. H. Menq, Characterization of 3d contact kinematics and prediction of resonant response of structures having 3d frictional constraint, Journal of Sound and vibration 217 (5) (1998) 909–925. doi:ISSN 0022-460X.

[35] a. D. J. E. K Y Sanliturk, A. B. Stanbridge, Underplatform dampers for turbine blades: Theoretical modelling, analysis and comparison with experimental data, Journal of Engineering for gas turbines and power 123 (4) (2001) 919–929. doi:ISSN 0742-4795.

[36] L. Panning, K. Popp, W. Sextro, F. Goetting, A. Kayser, I. Wolter, Asymmetrical underplatform dampers in gas turbine bladings: theory and application, Proceedings of ASME Turbo Expodoi:ISSN 0-7918-417-5.

[37] L. Panning, K. Popp, W. Sextro, F. Goetting, A. Kayser, I. Wolter, Advanced modeling of underplatform friction dampers for analysis of bladed disk vibration, Journal of Turbomachinery 129 (1) (2007) 143–150. doi:ISSN 0889-504X.

[38] Petrov, E.P., Ewinds, Analytical formulation of friction interface elements for analysis of nonlinear multiharmonic vibrations of bladed disks, Journal of Turbomachinery 125 (2003) 364–371.

[39] D.Laxalde, F.Thouverez, J.-J.Sinou, J.-P.Lombard, Qualitative analysis of forced response of blisks with friction ring dampers, European Journal of Mechanics A/Solids 26 (2007) 676–687.

[40] M.A.Niemotka, J.C.Ziegert, Optimal design of split ring dampers for gas turbine engines, Journal of Engineering for Gas Turbines and Power 117 (1995) 569575.

[41] D. Laxalde, F. Thouverez, Non-linear vibrations of multi-stage bladed disks systems with friction ring dampers, ASME 5 (2007) 3–10. doi:10.1115/DETC2007-34473.

[42] D. Laxalde, F. Thouverez, Forced reponse analysis of integrally bladed disks with friction ring dampers, Journal of Vibration and Acoustics 132. doi:10.1115/1.4000763.

[43] S. Roques, M. Legrand, P. Cartraud, C. Stoisser, C. Pierre, Modeling of a rotor speed transient response with radial rubbing, Journal of Sound and Vibration 329 (2010) 527–546. doi:10.1016/j.jsv.2009.09.016.

[44] M. A. Dokainish, K. Subbaraj, Influence of contact states on the dynamic behavior of rubbing structures, Journal Name 6-9 (2005) 1–3.

[45] M. A. Dokainish, K. Subbaraj, A survey of direct time integration methods in computational structural dynamics—ii. explicit methods, Computers and Structures 32 No. 6 (1989) 1387–1401.

[46] C. W. Bert, J. D. Stricklin, Comparative evaluation of six different numerical integration methods for nonlinear dynamic systems, Journal of Sound and Vibration 127 No. 2 (1988) 221–229.

[47] K. Y. Sanliturk, D. J. Ewins, Modeling two-dimensional friction contact and its application using harmonic balance method, Journal of sound and vibration 193 (1996) 511–523. doi:10.1006/jsvi.1996.0299.

[48] C. H. Menq, B. D. Yang, Non-linear spring resistance and friction damping of frictional constraint having two-dimensional motion, Journal of sound and vibration 217 (1998) 127–143. doi:10.1006/jsvi.1998.1739.

[49] B. D. Yang, C. H. Menq, Characterization of 3d contact kinematics and prediction of resonant response of structures having 3d frictional constraint, Journal of sound and vibration 217 (1998) 909–925. doi:10.1006/jsvi.1998.1802.

[50] K. H. Koh, J. H. Griffin, S. Filippi, A. Akay, Characterization of turbine blade friction dampers, Transaction of the ASME 127 (2005) 856–862. doi:10.1115/1.1926312.

[51] S. Zucca, J. Borrajo, M. M. Gola, Forced response of bladed disks in cyclic symmetry with underplatform damper, ASME Turbo Expo 2006: Power for Land, Sea and Air May 8-11.

[52] C. F. Beards, The damping of structural vibration by controlled inter-facial slip in joints, ASME 8.

[53] K. L. Johnson, Contact mechanics, cambridge university press, lon-don.

[54] J. A. Greenwood, J. P. B. Williamson, Contact of nominally flat surfaces, Proc. R. Soc. London, Ser.A 295 (1966) 300–319.

[55] A. A. Polycarpou, A. Soom, Boundary and mixed friction in the presence of dynamic normal loads. i. system model, ASME 117 (1995) 255–260.

[56] Y. Song, C. J. Hartwigsen, L. A. Bergman, A. F. Vakais, Simu-lation of dynamics of beam structures with bolted joints using adjustediwan beam elements, Journal of sound and vibration 273(1-2) (2004) 249–276.

[57] L. Gaul, S. Bohlen, Bohlen, identification of nonlinear structural joint models and implementation in discretized structure models, Proceedings of 11th ASME Conference on Mechanical Vibration and Noise: The Role of Damping in Vibration and Noise, Boston 5 (1987) 213–219.

[58] B. S. H. A A Ferri, Vibration analysis of dry friction damped turbine blades using singular perturbation theory, American Society of Mechanical Engineers, Journal of Vibration and Acoustics 120 (1998) 588–595.

[59] J. Wang, P. Sas, A method for identifying parameters of mechanical joints, American Society of Mechanical Engineers, Journal of Applied Mechanics 57 (1990) 337–342.

[60] Y. Ren, C. F. Beards, Identification of "effective" linear joints using coupling and joint identification techniques, American Society of Mechanical Engineers, Journal of Vibration and Acoustics 120 (1998) 331–338.

[61] S. A. Tobias, R. N. Arnold, The influence of dynamical imperfection on the vibration of rotating disks, Proceedings of the Institution of Mechanical Engineers 171 (1957) 669–690.

[62] J. T. Wagner, Coupling of turbomachine blade vibrations through the rotor, ASME Journal of Engineering for Power 89 (4) (1967) 502–512.

[63] A. Madden, B. I. Epureanu, S. Filippi, Reduced-order modeling approach for blisks with large mass, stiffness, and geometric mistuning, AIAA Journal 50 (2).

[64] S.-H. Lim, C. M.P., Pierre, Vibration modeling of bladed disks subjected to geometric mistuning and design changes, Proceedings of the 45th AIAA/ASME/ASCE/AHS/ASC Structures, Structural Dynamics, and Material Conference.

[65] A. Sinha, Reduced-order model of a bladed rotor with geometric mistuning, Journal of Turbomachinery 131 (031007) (2009) 1–7. doi:10.1115/1.2987237.

[66] D.L.Thomas, Dynamics of rotationally periodic structures, International Journal for Numerical methods in Engineering 14 (1979) 81–102.

[67] F. D'Ambrosio, E. Chatelet, G. Jacquet, Influence of contact states on the dynamic behavior of rubbing structures, ASME Turbo Expo June 6-9. doi:10.1115/GT2005-68560.

[68] O. S. Dinc, R. Cromer, S. J. Calabrese, Redesigning mechanical systems for low wear using system dynamics modeling, ASME 118 (1996) 415–422. doi:10.1115/1.2831318.

[69] ´Omer Tanrikulu, M. Imreg´un, Forced harmonic response analysis of nonlinear structures using describing function, AIAA Journal 31 (1993) 1313–1320.

[70] C.-H. Menq, J. Bielak, J. Griffin, The influence of microslip on vibratory response, part 2: a comparison with experimental resutls, Journal of Sound and Vibration 107(2) (1986) 295–307.

[71] E. Cigeroglu, N. An, C.-H. Menq, Wedge damper modeling and forced response prediction of frictionally constrained blades, ASME Turbo Expodoi:GT2007-27963.

[72] E. Cigeroglu, N. An, C.-H. Menq, Forced response prediction of constrained and unconstrained structures coupled through frictional contacts, ASME 131 (2009) 022505–1–022505–11.

[73] B. D. Yang, C. H. Menq, Characterization of contact kinematics and application to the design of wedge dampers in turbomachinery blading, 1 and 2, ASME paper 97-GT-19/20.

[74] E.P.Petrov, A method for use of cyclic symmetry properties in analysis of nonlinear multiharmonic vibrations of bladed disks, Journal of Turbomachinery 126 (2004) 175–183.

[75] F.Al-Bender, W.Symes, J.Swevers, H. V. Brusse, Theoretical analysis of the dynamic behavior of hysteresis elements in mechanical systems, International Journal of Non-Linear Mechanics 39 (2004) 1832–1735.

[76] L. Meirovitch, Analytical methods in vibration, Book.

[77] S.Neumark, Techn.Sc.D., Concept of complex stiffness applied to probles of oscillations with viscous and hysteretic damping, AERONAUTICAL RESEARCH COUNCIL REPORTS AND MEMORANDA.

[78] J. J. Chen, C. H. Menq, Prediction of the resonant response of frictionally constrained blade systems using constrained mode shapes, ASME 1998 International Gas Turbine and Aeroengine Congress and Exhibition 5. doi:ASME 1998 International Gas Turbine and Aeroengine Congress and Exhibition.

[79] E. P. Petrove, D. J. Ewins, Effects of damping and varying contact area at blade-disc joints in forced response analysis of bladed disk assemblies, Journal of Turbomachinery 128 (2) (2006) 406–410. doi:ISSN 0889-504X.

[80] E. P. Petrove, D. J. Ewins, Analytical formulation of friction interface elements for analysis of nonlinear multiharmonic vibrations of bladed discs, Transactions of ASME Journal of Turbomachinery 125 (2) (2003) 3364–371. doi:ISSN 0889-504X.

[81] C. Weiwert, J. W. L Panning, C. Richter, Multiharmonic forced response analysis of a turbine blading coupled by nonlinear contact forces, Journal of Engineering for gas Turbine and Power 132 (8). doi:ISSN 0742-4795.

[82] C. H. Menq, J. H. Griffin, A comparison of transient and steady state finite element analysis of the forced response of a frictionally damped beam, American Society of Mechanical Engineers, Journal of Vibration, Acoustics, Stress, and Reliability in Design 107 (1985) 19–25.

[83] S. W. Shaw, On the dynamic response of a system with dry friction, Journal of Sound and Vibration 108 (1986) 305–325.

[84] M. P. Castanier, C. Pierre, Investigation of the combined effects of intentional and random mistuning on the forced response of bladed disks, AIAA Journaldoi:10.1177/1077546309354863.

[85] D. J. Ewins, Vibration characteristics of bladed disc assemblies, Journal of Mechanical Engineering Science 15 (3).